
Radiating Insights: A Multiwavelength Study of Low-Luminosity Active Galactic Nuclei Jets

Gunjan Tomar

Advisor: Professor Nayantara Gupta



Raman Research Institute, Sadashivanagar, Bengaluru, Karnataka 560080, India

A doctoral thesis submitted in partial fulfilment of the requirements

for the degree of Doctor of Philosophy (Physics)

to

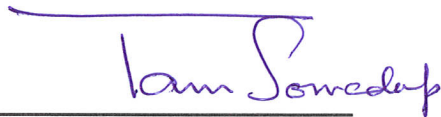


Jawaharlal Nehru University, New Delhi

2024

Certificate

This is to certify that the work submitted in the thesis titled '**Radiating Insights: A Multiwavelength Study of Low-Luminosity Active Galactic Nuclei Jets**,' submitted by **Gunjan Tomar** (Enrolment No. RRI/18/003) to the Jawaharlal Nehru University for the award of the degree of **Doctor of Philosophy (Ph.D.) in Physical Sciences** is the bonafide record of the original research work carried out by Gunjan Tomar under my guidance and supervision at **Raman Research Institute (RRI)**, Bengaluru, India. The results embodied in the thesis have not been submitted to any other University or Institute for the award of any degree or diploma.



Prof. Tarun Souradeep
Director & Professor, RRI



Prof. Nayantara Gupta
Supervisor

Astronomy & Astrophysics Group
Raman Research Institute (RRI)
Bengaluru 560080, Karnataka, India

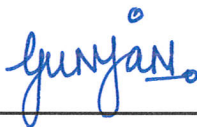
Declaration

I, **Gunjan Tomar** (Enrolment No. RRI/18/003), declare that the work reported in this thesis titled '**Radiating Insights: A Multiwavelength Study of Low-Luminosity Active Galactic Nuclei Jets**' is entirely original. This thesis has been composed by me at **Raman Research Institute (RRI)** under the supervision of **Professor Nayantara Gupta** and is the result of my own work unless otherwise stated. I further declare that the subject matter presented in this thesis has not previously formed the basis for awarding any degree, diploma, membership, associateship, fellowship, or any other similar title of any university or institution. I also declare that this thesis has been checked using the plagiarism software DRILLBIT.



Prof. Nayantara Gupta

Supervisor



Gunjan Tomar

Candidate

© Copyright by Gunjan Tomar, 2024. All rights reserved.

Abstract

In this thesis, we examine the non-thermal emission from jets in low-luminosity Active Galactic Nuclei (LLAGNs) across a range of energies, from radio to gamma rays. The main goal is to determine the physical parameters that characterize these jets. Massive galaxies typically have a supermassive black hole that powers an Active Galactic Nucleus (AGN). However, when the accretion rate onto these black holes decreases, the AGNs are classified as LLAGNs, mainly powered by radiatively inefficient accretion flows (RIAFs). Unlike more luminous AGNs, LLAGNs emit radiation from a combination of a jet, RIAF, and an outer thin disk, leading to discussions about their relative contributions.

In this thesis, we use multiwavelength observations and modeling techniques to understand the physical mechanisms behind these emissions. The significant detection of emission in gamma rays for a few LLAGNs has made our multi-wavelength data richer. A simple leptonic model is used to analyze the spectral energy distribution of the jets, offering constraints on the jet's contribution to the overall high-energy emission in LLAGNs. The results provide insights into the radiative environment in the jets and help estimate the total kinetic jet power. It also allows us to draw comparisons with the jet properties in luminous AGNs.

List of Publications

Publications [Part of This Thesis]

1. Gunjan Tomar, Nayantara Gupta, and Raj Prince. “Broadband Modeling of Low-luminosity Active Galactic Nuclei Detected in Gamma Rays”. In: *The Astrophysical Journal* 919.2, 137 (Oct. 2021), p. 137. doi: 10.3847/1538-4357/ac1588. arXiv: 2107.08256 [astro-ph.HE]. *
2. Gunjan Tomar and Nayantara Gupta. “X-Ray Flares in the Long-term Light Curve of Low-luminosity Active Galactic Nucleus M81*^{*}”. In: *The Astrophysical Journal* 950.2, 113 (June 2023), p. 113. doi: 10.3847/1538-4357/acd16d. arXiv: 2304.14265 [astro-ph.HE]. †

Conference Proceedings

1. Gunjan Tomar, Nayantara Gupta, and Raj Prince. “Emission from the jets of Low-luminosity Active Galactic Nuclei”. In: *PoS ICRC2023* (2023), p. 947. doi: 10.22323/1.444.0947.

Other Publication(s) [Not Part of the Thesis]

1. Gunjan Tomar, Pragati Pradhan, and Biswajit Paul. “New measurements of the cyclotron line energy in Cen X-3”. In: *MNRAS* 500.3 (Jan. 2021), pp. 3454–3461. doi: 10.1093/mnras/staa3477. arXiv: 2011.05534 [astro-ph.HE].

*Chapter 3

†Chapter 4



Contents

| | |
|---|-----|
| Abstract | vii |
| List of Publications | ix |
| 0 Synopsis | 1 |
| 0.1 Introduction | 1 |
| 0.2 Motivation and Aims | 3 |
| 0.3 Methodology | 4 |
| 0.4 Results | 6 |
| 0.4.1 SED modeling of LLAGNs detected in Gamma Rays | 6 |
| 0.4.2 The curious case of M81* | 6 |
| 0.5 Future Prospects | 7 |
| 1 Introduction | 9 |
| 1.1 Black Holes in a nutshell | 9 |
| 1.2 Accretion onto Black Holes | 11 |
| 1.2.1 The Standard Thin Disk | 14 |
| 1.2.2 Radiatively-Inefficient (or Advection-Dominated) Accretion Flow | 16 |
| 1.3 Active Galactic Nuclei | 20 |
| 1.3.1 A brief history of AGNs | 20 |
| 1.3.2 Structural Components of AGN: A General Picture | 23 |

| | | |
|-------------------------------|---|-----------|
| 1.3.3 | AGN Zoology and Unification | 28 |
| 1.4 | Jets | 30 |
| 1.4.1 | Jet launching and collimation | 32 |
| 1.4.2 | Accretion flows and outflows | 33 |
| 1.4.3 | Feedback process | 33 |
| 1.4.4 | Relativistic Effects | 34 |
| 1.5 | Emission Mechanisms of Jets | 37 |
| 1.5.1 | Synchrotron Emission | 38 |
| 1.5.2 | Inverse Compton Emission | 42 |
| 1.5.3 | Hadronic Emission | 43 |
| 1.6 | Kilo-parsec jets from AGN | 44 |
| 2 | Data Analysis and Multiwavelength Modeling | 47 |
| 2.1 | Gamma-Rays from Fermi Gamma-ray Space Telescope | 48 |
| 2.1.1 | Large Area Telescope | 49 |
| 2.1.2 | LAT Data Reduction and Analysis | 51 |
| 2.2 | X-Ray Emission | 57 |
| 2.2.1 | Instrumentation | 58 |
| 2.2.2 | Analysis | 62 |
| 2.2.3 | Neil Gehrels Swift Telescope | 68 |
| a) | Burst Alert Telescope (BAT) | 68 |
| b) | X-Ray Telescope (XRT) | 69 |
| c) | Ultra-Violet and Optical Telescope (UVOT) | 72 |
| 2.2.4 | XMM-Newton | 74 |
| a) | European Photon Imaging Camera (EPIC) | 75 |
| b) | Reflection Grating Spectrometer (RGS) | 77 |
| c) | Optical Monitor (OM) | 77 |
| Data Reduction for XMM-Newton | | 78 |
| 2.3 | Multiwavelength Modeling | 79 |

| | | |
|-------|--|-----|
| 3 | Gamma ray emission from kilo-parsec jets | 85 |
| 3.1 | Sample | 86 |
| 3.1.1 | NGC 315 | 87 |
| 3.1.2 | NGC 4261 | 89 |
| 3.1.3 | NGC 1275 | 89 |
| 3.1.4 | NGC 4486 (M87) | 91 |
| 3.2 | Multiwavelength Observations and Data Analysis | 92 |
| 3.2.1 | Radio to UV | 92 |
| | a) NGC 315 | 93 |
| | b) NGC 4261 | 93 |
| | c) NGC 1275 | 94 |
| | d) NGC 4486 | 94 |
| 3.2.2 | X-ray emission | 94 |
| | a) NGC 315 | 94 |
| | b) NGC 4261 | 95 |
| | c) NGC 1275 | 95 |
| | d) NGC 4486 | 96 |
| | XMM-Newton | 96 |
| | a) NGC 315 | 99 |
| | b) NGC 4486 | 99 |
| | Swift | 100 |
| | a) NGC 315 | 100 |
| 3.2.3 | Gamma-ray Data from Fermi-LAT | 101 |
| | Spectral Models for Fitting Gamma-ray Data | 102 |
| | Results of Gamma Ray Spectral Analysis | 103 |
| | a) NGC 315 | 103 |
| | b) NGC 4261 | 103 |
| | c) NGC 1275 | 104 |
| | d) NGC 4486 | 105 |

| | | |
|----------|--|------------|
| 3.3 | Multi-wavelength SED Modeling | 105 |
| 3.3.1 | SSC Model for Jet Emission | 109 |
| 3.3.2 | Multi-wavelength Emission from Extended jet | 110 |
| 3.4 | Summary and Conclusions | 111 |
| 4 | Curious case of M81* | 115 |
| 4.1 | M81* | 116 |
| 4.2 | Multi-wavelength Observations and Data Analysis | 117 |
| 4.2.1 | X-ray | 117 |
| 4.2.2 | UV-Optical | 119 |
| 4.2.3 | Gamma-Ray | 120 |
| 4.3 | Long-term X-ray Light Curve | 122 |
| 4.3.1 | Identification of Flares | 122 |
| 4.3.2 | Identification of Quiescent State Period | 123 |
| 4.4 | Multi-wavelength Spectral Energy Distributions | 124 |
| 4.4.1 | Construction of Spectral Energy Distributions for Different States | 124 |
| 4.4.2 | Modeling of Spectral Energy Distributions | 126 |
| 4.5 | Results | 129 |
| 4.6 | Discussion | 131 |
| 4.6.1 | Comparison with High-Synchrotron Peaked Blazars | 131 |
| 4.6.2 | Photon Index during Flares | 133 |
| 4.6.3 | Magnetic Field during Flares | 133 |
| 4.6.4 | Role of Doppler Boosting in Flaring | 134 |
| 4.6.5 | Other Parameters during Flares | 135 |
| 5 | Conclusions | 137 |
| 5.1 | Future Outlook | 139 |
| | Appendix A XRT Pile-up Correction | 143 |
| | Appendix B Errors in Swift-UVOT Fluxes | 145 |

Listing of figures

| | | |
|-----|---|----|
| 1.1 | The spectra for emission from a standard thin disk in AGN hosting a supermassive black hole of mass $10^6 M_{\odot}$ | 16 |
| 1.2 | Observed disk component for a blazar J1007+8135 peaking at UV frequency Paliya et al. (2017) | 17 |
| 1.3 | An average spectral energy distribution (SED) computed for RIAF model Nemmen et al. (2014a). The data points correspond to the geometric mean of high spatial resolution optical and UV observations, X-ray observations from Chandra, and high-resolution radio observation from Very Large Array (VLA) or VLBA/VLBI for 35 LLAGNs (Eracleous et al. 2010). The error bars show the scatter in the measurements. In the OUV, the open and filled circles correspond to the measurements with the maximal extinction correction and without any extinction correction, respectively. The black solid line is the average RIAF SED with the standard deviation shaded. | 18 |
| 1.4 | A schematic diagram showing the two accretion flow regimes in LLAGNs. | 20 |
| 1.5 | Hubble Space Telescope images of the host galaxy of Quasar 3C 273. A coronagraph is employed on the right to obscure the quasar's light, revealing the surrounding galaxy. Credit: NASA/ESA | 22 |
| 1.6 | Structural components in an AGN with typical scales. Red, brown, green, and yellow represent the disk, dusty torus, BLR & NLR, and double-sided jets, respectively. Image taken by Marin (2016) | 23 |

| | | |
|------|--|----|
| 1.7 | Schematic representation of standard unification model of AGN by Urry & Padovani (1995). Image by Emma Alexander: https://emmaalexander.github.io/resources.html | 29 |
| 1.8 | A schematic illustration of unification model for different classes of AGNs based on radiative efficiency and strength of jet, taken from Padovani et al. (2017). . . . | 30 |
| 1.9 | A montage taken from (Blandford et al. 2019), showing the jet (or outflow) LLAGN M87 (or better known FRI radio galaxy) at different scales, from its large outer lobes to the area close to its central SMBH. | 31 |
| 1.10 | The two panels at the bottom show HST contours overlaid on the Chandra image for an LLAGN M87, taken from Snios et al. 2019. As seen by HST and Chandra, knots in these panels are labeled as HST -1, D, E, F, I, A, B, and C. To explain the superluminal motion, we consider the motion of knot D along the jet from position D1 (imaged in 2012, t'_1) to D2 (imaged in 2017, t'_2). θ is the angle between the jet motion and the observer's line of sight. | 36 |
| 1.11 | The geometry of synchrotron emission from a single relativistic electron with Lorentz factor γ in the electron's rest frame and observer's frame (left). The synchrotron spectrum from a single relativistic electron with different γ is shown (right). | 39 |
| 1.12 | A schematic plot illustrating that a power-law distribution of leptons results in a total synchrotron emission spectrum that follows a power-law. This spectrum can be seen as the sum of the individual emission spectra from each electron in the lepton energy distribution. | 40 |
| 1.13 | Contour plot showing the self-absorption frequency ν_t as a function of the magnetic field B (in Gauss) and the Lorentz factor γ . The color bar indicates the value of ν_t in GHz. | 41 |
| 1.14 | A schematic representation of emission regions located at different distances from the BH along the jet of an AGN with an inclination θ | 45 |
| 2.1 | Fermi instrument taken from Thompson & Wilson-Hodge (2022) | 49 |

| | | |
|-----|--|----|
| 2.2 | The image illustrates the absorption of different electromagnetic wavelengths by Earth’s atmosphere, emphasizing the need for diverse observational platforms. . . . | 59 |
| 2.3 | Wolter mirrors’ design taken from NASA’s Imagine the Universe! The top panel shows the design of a cut-away X-ray telescope with nested cylindrical mirrors. . . . | 60 |
| 2.4 | A plot of the difference between the estimated model parameters and their true values versus the number of counts. C-Stat (red) can be used to fit models to Poisson-distributed count data at all count levels, as it provides unbiased parameter estimates. In contrast, the χ^2 statistic (blue), suitable for high counts (over 20), leads to biased estimates with fewer counts, underestimating amplitude and overestimating the power-law index. The figure is taken from Buchner & Boorman (2023). | 66 |
| 2.5 | The inset shows a schematic image of the Swift satellite. The top view in the middle clearly depicts the three onboard instruments, BAT, XRT, and UVOT, with their components highlighted. | 70 |
| 2.6 | Inset shows an artistic impression of the XMM-Newton. The sketch below the inset shows the different instruments and components onboard XMM-Newton. . . . | 75 |
| 2.7 | A 2D GRMHD simulation for radiatively inefficient accretion flow is presented: (left) small FOV focusing on detailed structures near the black hole, and (right) large FOV capturing the extended jet structure. Image is taken from Pu et al. 2022. Relativistic jets are launched from the funnel region of black holes via the BZ mechanism. The color represents density distribution shown on a logarithmic scale, where blue indicates low density and red indicates high density. A schematic (not-to-scale) one-zone model is white in the left panel. | 80 |
| 3.1 | NGC 315 image taken from Worrall et al. (2007a) showing large-scale radio and X-ray jet. Black contours represent a 5 GHz VLA radio map. The X-ray 0.8–5 keV image taken by Chandra. | 88 |

| | | |
|-----|---|-----|
| 3.2 | NGC 4261 image taken from Worrall et al. (2010) showing large-scale radio and X-ray jet. Black contours represent 5 GHz VLA radio map (Birkinshaw & Davies 1985a). The X-ray 0.4–2 keV image taken by ROSAT is smoothed with a Gaussian of $\sigma = 30$ arcsec. | 90 |
| 3.3 | The multiwavelength SED of NGC 315 constructed using radio data taken from Capetti et al. (2005), Lazio et al. (2001), Nagar et al. (2005), Agudo et al. (2014), Kovalev et al. (2005) and Venturi et al. (1993), infrared data taken from Gu et al. (2007), Heckman et al. (1983) and Verdoes Kleijn et al. (2002), optical data taken from Verdoes Kleijn et al. (2002) and Younes et al. (2012), X-ray data taken from Worrall et al. (2007b). Other data points from NED are shown in silver. | 96 |
| 3.4 | The multiwavelength SED of NGC 4261 constructed using radio data taken from Jones & Wehrle (1997), Nagar et al. (2005), infrared data taken from Asmus et al. (2014), optical data taken from Ferrarese et al. (1996). The X-ray observation is taken from Zezas et al. (2005). Other data points from NED are shown in silver. The higher flux in radio is due to low-resolution measurements, which could have a significant contribution from the radio lobes of NGC 4261. | 97 |
| 3.5 | The multiwavelength SED of NGC 1275 is constructed using radio data from Abdo et al. (2009a). X-ray data has been taken from Tanada et al. (2018a) and Ajello et al. (2009). Other data points from NED are shown in silver. | 97 |
| 3.6 | The multiwavelength SED of NGC 4486 constructed using data taken from Nagar et al. (2001), Prieto et al. (2016), Whysong & Antonucci (2004) and Perlman et al. (2001). Other data points from NED are shown in silver. The higher flux in radio is due to low-resolution measurements, which could have a significant contribution from the radio lobes of NGC 4486. | 98 |
| 3.7 | The γ -ray SED obtained by <i>Fermi-LAT</i> from 12 years of observations. The shaded part corresponds to 1σ -uncertainty in the respective fit. When $TS < 4$, upper limits at 95% confidence level are plotted with a down arrow. | 104 |

| | | |
|-----|--|-----|
| 3.8 | One zone leptonic modeling of broadband emission from sub-parsec scale jets of the four LLAGNs. The thermal synchrotron and the blackbody components of M87 have been reproduced from Lucchini et al. (2019). The gamma-ray data beyond 1.6 GeV from NGC 315 and 0.6 GeV from NGC 4261 cannot be explained with one zone SSC model. | 107 |
| 3.9 | Leptonic model for emission from sub-parsec (blue) and extended jets (black) for NGC 315 and NGC 4261. The radio and X-ray data for the extended jets are shown in red and pink, respectively. | 110 |
| 4.1 | The lightcurve in (a) soft X-ray energies (0.5-2.0 keV) and (b) hard X-ray energies (2.0-10.0 keV), and the light curve in the (c) optical and (d) UV. The yellow region represents the quiescent state (MJD 56467.7 - MJD 56796.7). The brown line (MJD 55814.83 - MJD 55823.35), and the purple (MJD 56796.74 - MJD 56983.37) and teal (MJD 56983.37 - MJD 57160.25) shaded regions represent Flare A, Flare B, and Flare C, respectively. | 120 |
| 4.2 | Same as Figures 4.1(a) and (b), zoomed in to the region of Flare B and Flare C to show the change in flux. | 123 |

- 4.3 The lightcurve during the period considered at the time of knot ejection (King et al. 2016). The measurements in radio are taken from the same work. The black data points are Swift measurements. The magenta line in Panels (a) and (b), represent the Bayesian blocks, as in Figure 4.1. The blue dotted line is the mean flux over the entire period of 16 yr that we have considered in our study. The red line in panel (a) is the mean flux plus 0.8σ , which represents the peak flux of the X-ray flare associated with the knot ejection, while the blue dotted-dashed line represents 1σ over the mean flux. The vertical dotted-dashed lines represent the four epochs: 2011, September 17, September 21, September 27, and October 4, in the same order. For Flare A, we consider the radio data taken at Epoch 1 (2011 September 17) as it lies within the flare period for a simultaneous radio to X-ray SED. We also construct the SEDs for Epochs 2, 3, and 4 when quasi-simultaneous single-epoch X-ray measurements are available. 125
- 4.4 The multi-wavelength data of M81* at different epochs and flaring periods are shown in color. In the X-ray band, the power law component of the X-ray spectrum obtained in these different states has been shown, with the shaded region representing the errors at 90% confidence level (2.706σ). The simultaneous multi-wavelength data from Markoff et al. (2004) at a quiescent period are also shown by open circles for reference. The gray diamonds are the archival data obtained from the NASA/IPAC Extragalactic Database (NED), shown here as a secondary constraint for modeling at the frequencies where the simultaneous/quasi-simultaneous data are unavailable. 126
- 4.5 One-zone SED modeling of M81* during different states. Panel (c): the dotted curves in the modeling represent the evolution of SED from the initial time of injected electrons to the final age of the system, which explains the emission at this epoch. Panels (a)-(g): X-ray data for different states are black. The upper limits obtained using Fermi-LAT data are shown in olive to constrain the SSC component and, thus, the size of the emission region. Panel (h): Simulated SEDs for all the states and epochs plotted together to show their spectral shape and flux variations. 128

| | | |
|-----|---|-----|
| 4.6 | Time evolution of observables, (a) X-ray photon index, Γ_x , and (b) soft X-ray flux, and the parameters obtained from modeling, (c) injected electron spectral index, (d) energy density of injected electrons, (e) the magnetic field in the emission region, and (f) the jet power in injected electrons. We do not have any quasi-simultaneous X-ray data for Epoch 3, so there is a break in the connected dot plot in the top two panels | 132 |
| 4.7 | SED of blazar 1ES 1959+650 obtained using a one-zone SSC model during quiescent state (red dashed line; reproduced from Tagliaferri et al. 2008) and flaring state (blue dashed line; reproduced from MAGIC Collaboration et al. 2020a) compared with that of M81* during quiescent state (red solid line) and flaring states (blue, green, and yellow solid lines). | 135 |

To you, who decided to pick up my thesis!

“It’s a magical world, Hobbes, ol’ buddy... let’s go exploring!”

— Bill Watterson, Calvin and Hobbes

Acknowledgments

Space is hard, words are harder. †

I would like to express my deepest gratitude to my advisor, Professor Nayantara Gupta, for her unwavering support, guidance, and trust throughout this journey. I sincerely thank Professor Biswajit Paul for offering me my first research project experience and invaluable learning opportunities.

Special thanks to my thesis committee members, Professors Udaya and Vikram Rana, for their constructive feedback and to Mahima for her constant help and support.

I am also grateful to Shigeo Kimura, Markus Bottcher, and Soebur Razzaque for the insightful discussions that have significantly contributed to my learning and growth. Additionally, I appreciate their warm hospitality during my visits.

Sree and Rukaiya, thank you for the cherished memories and support during my visit to Potchefstroom. You both hold a special place in my heart.

Coming to RRI, a big thank you to those who made it a welcoming and warm place from the first step in Raj, Karam, Sreeja, Varun, Nancy, Anand, Sebanti, and Akash. You all are missed. Sukanya, Manami, and Shreya, I will always cherish our shared memories. Rashid, Sandeep, and Anirban, the coursework was fun with you guys.

I would also like to acknowledge the nicest faculty members on the Astro floor and their guidance from time to time.

Ashwin, I owe you the biggest thanks for encouraging and teaching me bash scripting, among several other things I learned from you. Yash, Rajorshi, and Aman

†Becky Smethurst (A Brief History of Black Holes)

thank you so much for being my agony aunts! I couldn't imagine the last few years at RRI without you guys. Saurabh, you've been both a mentor and a friend, and I can't thank you enough. Sovan, thank you for the sweet gestures like bringing little flowers that always managed to make me smile. Also, thank you for proofreading my thesis—it was much needed. Thanks to Kinjal, too, for the proofreading and, of course, also for being a friend. I would also like to express my gratitude to the people without whom the Astro floor couldn't have been complete for me: Sayan, Dipanshu, Sarvesh, Rahul, Ajith, Adarsh, and Naren. Fluffy and ChiChi (Chi-square), your fluff therapy has been therapeutic and invaluable to me. Oreo, Chintu, Vinegar, and all the cats I was too lazy to name myself made RRI a better place for me.

The tough times were a little less tough with all of you (and the cats) around me. Oh, how badly I will miss RRI.

Special thanks to Varalakshmi-amma for loving us as your own kids. I would also like to acknowledge the admin, library, security, and canteen staff who have always been kind and helpful.

Bangalore, you have been so nice. I will miss you the most!

And as they say, last but not least, my deepest gratitude goes to my family—Bhai, MaaPaa, Dijuu, and Vishal. This would not have been possible without your constant love, support, and faith in me, which have been the strongest sources of strength throughout my Ph.D. journey.

To anyone I may have missed, I apologize. I appreciate your presence and support in this journey, but I blame my “re-mem-bory” issues. Words really are the hardest, and I cannot express my gratitude for all the people I met and made friends with during this long, scary, and fun journey. Thank you, all.

The end of an ERA!

You MIGHT say![§]

[§]Monica Geller (F.R.I.E.N.D.S.)

0

Synopsis

This thesis aims to study the emission from the jets of Low-Luminosity Active Galactic Nuclei (LLAGNs) across broadband energies ranging from radio to gamma rays in order to constrain the physical parameters of the jet.

0.1 Introduction

There is a widely accepted consensus in the scientific community that the majority of galaxies if not all, contain supermassive black holes (SMBHs) at their centers. These SMBHs are responsible for powering the most energetic and luminous celes-

tial objects known as Active Galactic Nuclei (AGNs). According to the unified model of AGN, the different classes of AGN exist only due to changes in a small number of parameters like the orientation (Quasars and Radio Galaxies), presence of jet (Quasars and Seyferts), radiative efficiency (Quasars, BL Lac, LLAGNs, LINERs), etc. and are intrinsically the same. However, the rate at which material accretes onto these SMBHs can significantly impact the accretion process within these systems. Consequently, this distinction leads to the categorization of AGNs into two broad classes: AGNs and low-luminosity AGNs (LLAGNs). Therefore, when the accretion rate falls below $0.01L_{Edd}$, where L_{Edd} is the Eddington luminosity of the SMBH, the kinetic energy is advected into SMBHs instead of radiating away. The accretion flow, in this case, is thus termed radiatively inefficient accretion flow (RIAF). LLAGNs are typically powered by RIAFs. RIAFs, although, inefficient at converting accreting matter into radiation, are known to be very efficient at producing jets and/or outflows. We view these jets in LLAGNs under a multiwavelength lens with a particular focus on high energy emission ranging from X-rays to gamma rays.

Unlike the luminous AGNs, more precisely blazars, where the emission from the source is dominated by the emission from the jets due to Doppler boosting, it has been suggested that in most LLAGNs, emission comes from three components: a jet, RIAF, and an outer thin disk. Their relative contributions are still under debate, especially in X-rays. Multiwavelength observations and their simultaneous modeling are powerful diagnostics to probe the physical mechanism in these extreme environments and thus resolve this debate.

0.2 Motivation and Aims

Despite their abundance in the local Universe, the LLAGNs are not well studied due to their faintness. Studying LLAGNs become important for several reasons as follows:

- understanding the AGN population helps us understand galaxy formation and evolution
- studying the detailed physics of AGN, including the accretion processes onto the SMBHs and the emission mechanisms
- AGN feedback processes: constraining the jet parameters and, consequently, the jet properties allow us to dive into the kinetic mode feedback, at the heart of which is the jet activity in LLAGNs.

Studying LLAGNs is also important to resolve a longstanding problem of the origin of Ultra-High Energy Cosmic Rays (UHECRs). At ultra-high energies, the cosmic rays have been observed to become heavier, thus implying that the sources must be nearby (less than 100 Mpc) to avoid photo-disintegration during their propagation to Earth. Also, at the source, low luminosity implies lesser photoionization of the cosmic rays, which is a necessary condition for the UHECR sources. Given their abundance in the local Universe, it becomes indispensable to study these objects.

Despite their faintness, few LLAGNs have been observed in broad energy bands ranging from radio to X-rays, and even fewer have been observed emitting gamma rays. The broadband detection of these objects motivates the construction of the broadband SEDs of these objects and constrains the physical jet parameters in these sources.

0.3 Methodology

Palomar survey is an optical spectroscopic survey of northern galaxies with a declination dominated by the population of LLAGNs. Out of many LLAGNs, only four of the LLAGNs have been detected in gamma rays, namely NGC 4486, NGC 1275, NGC 315, and NGC 4261. While NGC 4486 and NGC 1275 have been detected in gamma rays and even higher energies, NGC 315 and NGC 4261 were detected in gamma rays for the first time. In Tomar et al. (2021), we follow the standard reduction and analysis procedure to extract the gamma-ray spectrum for all four sources using the gamma-ray sky-survey instrument Fermi-LAT. Distributions like power-law and log-parabola are used to model the gamma-ray spectrum in order to find the best-fit model and, consequently, any hints of curvature in the spectrum. A curvature in the gamma-ray spectrum points at the curvature in the particle distribution, producing this spectrum and thus providing an essential tool to constrain the particle population in the region of interest.

We also reduced and analyzed the available observations of X-ray observatories like NuSTAR, XMM-Newton, and Swift. The reduced spectrum is modeled by a standard continuum model (an absorbed power-law; `phabs*powerlaw`) in XSPEC. `phabs` take care of the Galactic absorption of soft X-rays along our line of sight, whereas `power-law` models the non-thermal continuum expected in the jet. We consider the spectrum and flux corresponding to the power-law only to construct the SED. To construct the broadband SEDs for each source, we also take radio to optical data from the archive.

In Tomar & Gupta (2023), we studied the ejection of discrete knots from LLAGN M81* to better understand how the jets of LLAGNs compare to those in more luminous AGNs. The detection of discrete knot ejection from M81* holds particular sig-

nificance as it challenges the conventional expectation that, unlike luminous AGN jets, LLAGN jets should be continuous. The non-detection of gamma-ray emission from M81* remains challenging, partly due to the proximity of the strong gamma-ray emitter M82, a starburst galaxy located just 0.6 degrees away from M81. Therefore, we could only obtain upper limits on the gamma-ray emission from the source using ~ 14 yr Fermi-LAT data.

We constructed a 16-year long-term lightcurve in X-rays using data from an X-ray telescope (XRT) instrument onboard Swift. The data is reduced and analyzed using the standard procedure. To construct the light curve, the power-law flux is plotted for each observation with respect to the observation date. The obtained light curve is thus modeled using the Bayesian block approach, which creates histograms with bin sizes that adapt to the data to identify flaring activity in the light curve.

The SEDs are constructed during the identified X-ray flaring periods and the knot ejection period using the X-ray data analyzed and upper limits in gamma-ray obtained using Fermi-LAT data. Archival radio data, whenever available, is taken to complete the broadband SED.

In both Tomar et al. (2021) and Tomar & Gupta (2023), all the SEDs thus obtained were modeled with a one-zone leptonic model, which incorporated synchrotron and synchrotron self-Compton emission processes. In this model, we assumed that the broadband emission originates from a single spherical homogeneous blob of radius R in the jet. This blob has entangled magnetic field B and moves with a bulk Lorentz factor of Γ . We assume a continuous injection of a non-thermal (accelerated) population of electrons, which then enters the blob and cools down predominantly via synchrotron and synchrotron self-Compton (SSC) processes. As a result of the relativistic motion of the jet, the radiation is Doppler boosted along our line of sight, δ , although smaller for the case of the LLAGNs (approx. 1-2). To calculate

the emission thus produced, we use an open-source code, GAMERA, which solves the time-dependent transport equation for the leptons in 1-dimension.

0.4 Results

0.4.1 SED modeling of LLAGNs detected in Gamma Rays

In Tomar et al. (2021), the leptonic modeling of the SEDs of NGC 1275, NGC 4486, NGC 315, and NGC 4261 revealed that synchrotron and synchrotron self-Compton emission from an emission region at sub-parsec scale within the jet can explain the SEDs up to a few GeV. Since NGC 1265 and NGC 4486 are well-studied, we only study NGC 315 and NGC 4261 further. For the latter two cases, we find an excess above a few GeV. To explain this excess, we considered another emission region at a kilo-parsec scale jet. The low spatial resolution of Fermi-LAT at gamma-ray energies does not allow distinction between the emission regions at sub-parsec and kilo-parsec scale regions. We used the radio and X-ray observations of a kilo-parsec jet to constrain the gamma-ray emission from this region. We found that the excess beyond a few GeV is successfully attributed to gamma rays produced by the upscattering of starlight photons from the host galaxy by ultra-relativistic electrons within the kilo-parsec scale jets of NGC 315 and NGC 4261. This finding suggested that similar to luminous AGNs, LLAGNs can accelerate electrons to ultra-relativistic energies within their kilo-parsec jets.

0.4.2 The curious case of M81*

In Tomar & Gupta (2023), we identified three X-ray flaring periods in the ~ 16 yr light curve. Including the quiescent state, we thus obtained 7 SEDs. Interestingly, each SED is well explained by synchrotron emission from the jet of M81*.

This suggested striking similarities between the synchrotron emission processes in LLAGNs and high-synchrotron-peaked blazars, a sub-class of luminous AGNs. This finding, therefore, hinted at a common jet mechanism operating across different luminosity scales within AGNs.

0.5 Future Prospects

We aim to contribute to resolving a longstanding question in astrophysics and cosmic ray studies: the origin and propagation of cosmic rays in the Universe, particularly at ultra-high energies ($E \geq 10^{18}$ eV), where their source remains elusive. Evidence suggests the presence of heavier nuclei at these energies, implying that the source of these ultra-high-energy cosmic rays must be relatively close to Earth to avoid photodisintegration during their journey. LLAGNs dominantly occupy the local Universe at this distance. Therefore, to tackle the puzzle of UHECR origin, we plan to employ a lepto-hadronic model to investigate the broadband emissions from NGC 315 and NGC 4261, low-luminosity AGNs. Our study seeks to constrain the multiwavelength emissions ranging from radio to gamma rays from these AGNs while also placing constraints on other crucial messengers like neutrinos. This can further be extended to study the entire population of LLAGNs to determine their role in accelerating UHECRs.

*"Twinkle, twinkle, quasi-star
Biggest puzzle from afar
How unlike the other ones
Brighter than a billion suns
Twinkle, twinkle, quasi-star
How I wonder what you are."*

George Gamow, Quasar (1964)

1

Introduction

1.1 Black Holes in a nutshell

Black Holes (BHs) are ubiquitous in the Universe. These objects have a strong gravitational pull from which not even light can escape from their event horizon. It is estimated that any large galaxy, including our Milky Way, could contain tens of millions to over 100 million stellar-mass black holes. Since they do not emit light, black holes are challenging to detect directly. Instead, they are often identified by their gravitational effects on nearby stars and gas or by the radiation emitted from matter accreting onto them. They are the strangest and most enigmatic objects

in the Universe but also ‘simple’ because they can be characterized by only three parameters - mass, spin, and charge (stemming from the no-hair theorem), unlike the other astrophysical objects. While the ‘black hole’ was first predicted only theoretically as a solution to Einstein’s equation, the discovery of Cygnus X-1 and many more made it clear that these objects are out in the Universe. Recently, the Event Horizon Telescope (EHT) collaboration provided direct visual evidence for their existence with the first direct BH images of extremely massive BHs: Sgr A* (The Event Horizon Telescope Collaboration 2023) and M87* (Event Horizon Telescope Collaboration et al. 2019, The Event Horizon Telescope-Multi-wavelength science working group et al. 2024).

Astrophysical BHs are categorized into three categories based on their mass: stellar, intermediate, and supermassive. A stellar BH (sBH) is an end-product of the life of a massive star and can weigh between 5 and 10 times the solar mass (M_{\odot}). A supermassive BH (SMBH) may have millions to tens of billions of times the solar mass and reside at the center of almost all massive galaxies, including our Milky Way. How these gigantic BHs spawn remains unclear, unlike sBHs, although many mechanisms have been proposed (Volonteri 2010, Kormendy & Ho 2013). Although scientists agree that once these giants have formed independently of the formation channel, they can grow to even more humongous sizes by feeding onto the dust and gas around them, i.e., via *accretion* or by merging with other BHs. Intermediate-mass BHs (IMBHs) are medium-sized BHs with masses between 100 to 10^5 times M_{\odot} . Although conclusive evidence for these IMBHs remains elusive, several studies hint at their presence. Several pathways are proposed for their origin, such as mergers of several sBHs in a crowded galaxy area.

Studying black holes is crucial for fundamental physics and understanding the mechanisms that power the most energetic astrophysical phenomena in the Uni-

verse. This thesis aims to characterize the emission from accreting SMBHs in low-luminosity AGNs, particularly the high-energy emission from their collimated, relativistic outflows (or jets) launched from these systems. By studying these jets, we bridge the understanding of jet formation mechanisms across scales, from sBHs in X-ray binaries to SMBHs in Quasars.

1.2 Accretion onto Black Holes

Accretion is the inflow of matter or dust on a gravitating object like a black hole. The gas accretion onto black holes has been widely accepted as the primary radiation source from black hole X-ray binaries (BHXRBS) and active galactic nuclei (AGNs). The gas falling into the gravitational potential well of the black hole loses its potential energy, which is then converted into kinetic energy. The released kinetic energy is converted to thermal energy through interactions and friction within the accreting material. Before discussing the different accretion flows in these BH systems, we will derive the mathematical form of the Eddington limit (Frank et al. 2002) below. The Eddington limit is a physical limit on the luminosity emitted by an accreting object to first order.

We assume a steady spherical accretion, where the accretion material is assumed to be mainly hydrogen and fully ionized. Electrons and protons are thus assumed to be coupled in the accretion material. The radiation exerts a force on free electrons through Thomson scattering due to the large scattering cross-section for free electrons compared to protons. Since a black hole does not have a hard surface, the radius of the black hole refers to the region into which the matter can fall and cannot escape. This uncertainty in the radius in case of accretion onto a black hole is often parametrized by η , known as the accretion efficiency. The gravitational potential energy released by accretion of mass m (or m_p in this case, since the grav-

itational force mainly acts on the protons [$GM(m_p + m_e)/r^2 \cong GMm_p/r^2$]) onto a black hole of mass M_{BH} , at Schwarzschild radius R_s is

$$\Delta E = \eta \frac{GM_{BH}m}{R_s} \quad (1.1)$$

where G is the gravitational constant. In other words, the energy released by accretion is

$$\Delta E = \eta \frac{GM_{BH}m_p}{2GM_{BH}/c^2} = \eta mc^2 \quad (1.2)$$

The accretion luminosity thus can be defined as

$$L = \frac{d}{dt} \Delta E = \eta \dot{m} c^2 \quad (1.3)$$

where \dot{m}_p is the accretion rate quantifying the amount of matter crossing the event horizon of the black hole per unit time.

If the luminosity of the accreting black hole is L (erg s^{-1}), then the radiant energy flux at a distance r from the object emitting isotropically, S ($\text{erg s}^{-1} \text{ cm}^{-2}$) = $L/4\pi r^2$. Therefore, the radiative force F_{rad} on each electron, which is equal to the rate at which it absorbs momentum, is $\sigma_T S/c$, where $\sigma_T = 6.7 \times 10^{-25} \text{ cm}^2$ is the Thomson cross-section for the electron and c is the speed of light. Due to the attractive electrostatic Coulomb force between electrons and protons, the electrons drag protons with them when a radiative force acts on them. Therefore, the radiative force pushes the electron-proton pairs outwards against the total gravitational force acting on each pair inwards. The net inward force on an electron-proton pair is then $(GMm_p - \frac{L\sigma_T}{4\pi c}) \frac{1}{r^2}$, which vanishes for the limiting luminosity, i.e., the Ed-

Edington luminosity,

$$L_{Edd} = 4\pi M m_p c / \sigma_T \quad (1.4)$$

$$\cong 1.38 \times 10^{38} (M/M_\odot) \quad (1.5)$$

From Equations 1.3 and 1.4, the limiting accretion rate or Eddington accretion rate, $\dot{m}_{Edd} = L/\eta c^2$. As can be seen, \dot{m}_{Edd} depends on accretion efficiency, i.e., the more the efficiency of the accretion, the lower the Eddington mass accretion rate, which determines the accretion flow, significantly closer to black holes (discussed in the following sections). In other words, the efficiency of radiative losses affects the dynamical properties of black-hole accretion flows. To understand the accretion behavior relative to the theoretical maximum (i.e., the Eddington limit), we use the Eddington ratio. The *Eddington ratio* is defined as the ratio of luminosity L released by an accreting mass and its limit given by the Eddington luminosity L_{Edd} . We can write the Eddington ratio in terms of mass accretion rate, too, using Equations 1.3 and 1.4, which is,

$$\frac{L}{L_{Edd}} = \frac{\eta \dot{m} c^2}{L_{Edd}} = \frac{\dot{m}}{\dot{m}_{Edd}} \quad (1.6)$$

In most cases, the accreting matter possesses considerable angular momentum per unit mass, which prevents the matter from falling directly onto the black hole and instead settles in to form a disk-like structure, efficiently extracting gravitational potential energy and converting it into radiation. For matter to accrete, some form of friction dissipating angular momentum is required. Supercomputer simulations have played a pivotal role in verifying that angular momentum's dissipation is most likely mediated by magnetorotational instability (Balbus & Hawley 1991). The accretion flows can be described by four basic models - the standard thin disk (Shakura & Sunyaev 1973), the optically thin two-temperature disk

(Shapiro et al. 1976), the slim disk (Abramowicz et al. 1988), and the advection-dominated accretion flow (ADAF) (Narayan & Yi 1994). The optically thin two-temperature accretion flow is optically thin with virial temperature in ions and $\sim 10^9$ K in electrons and is found to be thermally unstable (Piran 1978). The ‘slim disk’ accretion flow is an optically thick advection-dominated accretion flow developed for high accretion rate systems with substantial gas density. The energy conversion into radiation is inefficient as it is primarily advected into the black hole in the form of photons. Although Radiatively Inefficient Accretion Flows (RIAFs) also encompass other models like Adiabatic Inflow-Outflow Solutions (ADIOS; Blandford & Begelman 1999a), Convection-Dominated Accretion Flows (CDAFs; Narayan et al. 2000), in studies of LLAGNs, ADAFs and RIAFs are often used interchangeably in this thesis, unless otherwise mentioned. These represent accretion flows that are optically thin and geometrically thick, unlike the standard thin disk model. We discuss these two models in more detail in the Sections 1.2.1 and 1.2.2.

1.2.1 The Standard Thin Disk

The Standard Thin Disk or Shakura-Sunyaev model is the best-known and studied theoretical model. It is a prototypical example of radiatively efficient accretion flow. Irrespective of the dissipation mechanism, the Shakura-Sunyaev model assumes that the disk is in local thermal equilibrium and can efficiently radiate the heat generated by viscous dissipation, allowing it to cool and maintain a geometrically thin structure. It is geometrically thin in the vertical direction with $H/r < 1$, where H is the vertical height of the disk and r is the radius, and characterized by a multi-temperature black body with effective temperatures in the range of 10^5 and 10^7 K from supermassive black holes to stellar mass black holes.

The viscous dissipation rate per unit area in this case is given by:

$$D(R) = \frac{3GM_{BH}\dot{m}}{8\pi R^3} \left[1 - \frac{R_{ISCO}}{R} \right] \quad (1.7)$$

where R is the distance from the black hole, R_{ISCO} is the innermost stable circular orbit of the black hole. Assuming that the disc is optically thick in the z direction, each ring element of the disk of radius R radiates roughly as a blackbody (see Figure 1.1) with a temperature $T(R)$, which is given by equating the dissipation rate $D(R)$ per unit face area to the blackbody flux.

$$\sigma T^4(R) = D(R) \quad (1.8)$$

$$\Rightarrow T(R) = \left\{ \frac{3GM_{BH}\dot{m}}{8\pi R^3} \left[1 - \left(\frac{R_{ISCO}}{R} \right)^{1/2} \right] \right\}^{1/4} \quad (1.9)$$

The $T(R)$ here can be considered analogous to the star's effective temperature. Therefore, the spectrum emitted by each area element of the disc can be approximated as,

$$I_\nu = B_\nu[T(R)] = \frac{2h\nu^3}{c^2(e^{h\nu/kT(R)} - 1)} \quad (\text{erg s}^{-1} \text{ cm}^{-2} \text{ Hz}^{-1} \text{ sr}^{-1}) \quad (1.10)$$

which may not represent the disc spectrum accurately, especially in cases where the atmospheric opacity is a rapidly varying function of frequency. The observed flux at any given frequency from the disc inclined at angle i concerning the observer at a distance D can be given by,

$$F_\nu = \frac{2\pi \cos i}{D^2} \int_{R_*}^{R_{\text{out}}} I_\nu R dR \quad (1.11)$$

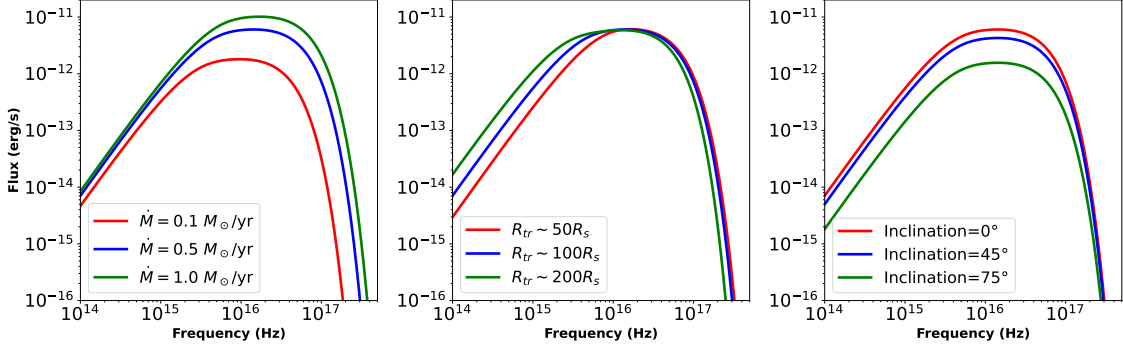


Figure 1.1: The spectra for emission from a standard thin disk in AGN hosting a supermassive black hole of mass $10^6 M_\odot$.

where R_{out} is the outer radius of the disc. Using the blackbody assumption, we get

$$F_\nu = \frac{4\pi h \cos i \nu^3}{c^2 D^2} \int_{R_*}^{R_{out}} \frac{R dR}{e^{h\nu/kT(R)} - 1} \quad (1.12)$$

Now, from Equation 1.9, we can find the temperature at which the spectrum peaks by the derivative of the equation w.r.t. frequency, which gives,

$$T_{pk} = \frac{2.34}{k_B} \left(\frac{M_{BH}}{10M_\odot} \right)^{-1/2} \left(\frac{R_{in}}{R_g} \right) \left(\frac{\dot{m}}{10^{-8} M_\odot \text{yr}^{-1}} \right)^{1/4} \text{ keV} \quad (1.13)$$

where k_B is the Boltzmann constant, R_{in} is the innermost radius of the disk, and R_g is the gravitational radius of the black hole. As can be followed from Equation 1.13, the spectrum of AGN accretion disks peak between ultraviolet to optical frequencies (for, e.g., see Figure 1.2). This model has been used successfully to model supermassive black holes accreting at rates ranging from a few and a few tens of the Eddington limit, i.e., $\frac{\dot{m}}{\dot{m}_{Edd}} \geq 1 - 10$. This limit can be typified by λ_{Edd} .

1.2.2 Radiatively-Inefficient (or Advection-Dominated) Accretion Flow

Unlike the standard accretion flow (Section 1.2.1), where the energy released by viscous dissipation is assumed to be emitted locally, the power is not radiated ef-

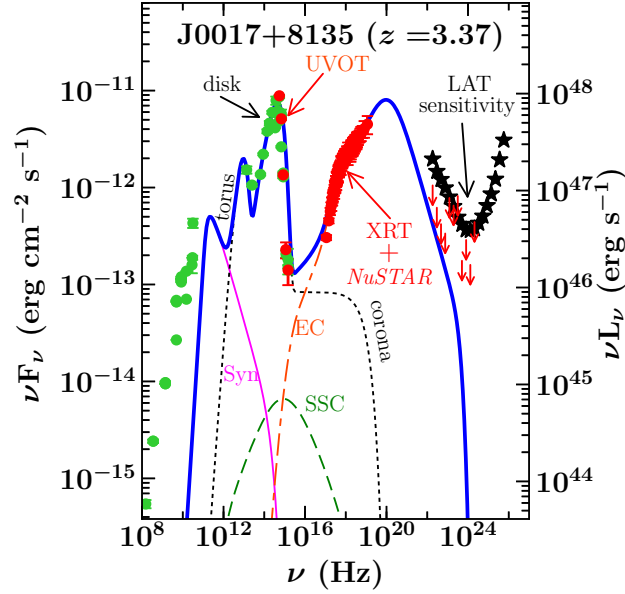


Figure 1.2: Observed disk component for a blazar J1007+8135 peaking at UV frequency Paliya et al. (2017)

ficiently in the case of the radiatively inefficient accretion flow. Instead, a fraction of it is stored as the plasma thermal energy, which is eventually advected into the event horizon before being radiated away. This underluminous accretion flow is known as advection-dominated accretion flow (ADAF). ADAF has two regimes: radiatively inefficient accretion flow (RIAF) and slim disk. Slim-disk ADAF applies when the accretion rate is super-Eddington. The particles in the gas cool efficiently, but due to the high scattering optical depth, the radiation cannot diffuse out of the system. This regime is critical in understanding the ultra-luminous X-ray sources (ULXs), which slim-disk ADAF likely powers onto stellar-mass black holes or neutron stars at a super-Eddington accretion rate.

On the contrary, if the accretion rate is sub-Eddington, the cooling time scales are much larger than the acceleration timescale of the particles due to the low scattering optical depth of the accreting gas. This regime, the radiatively inefficient accretion flow, or RIAF, powers the low-luminosity AGN (LLAGNs). Therefore, we can drop the term ADAF hereafter and refer to these flows in LLAGNs as RIAF.

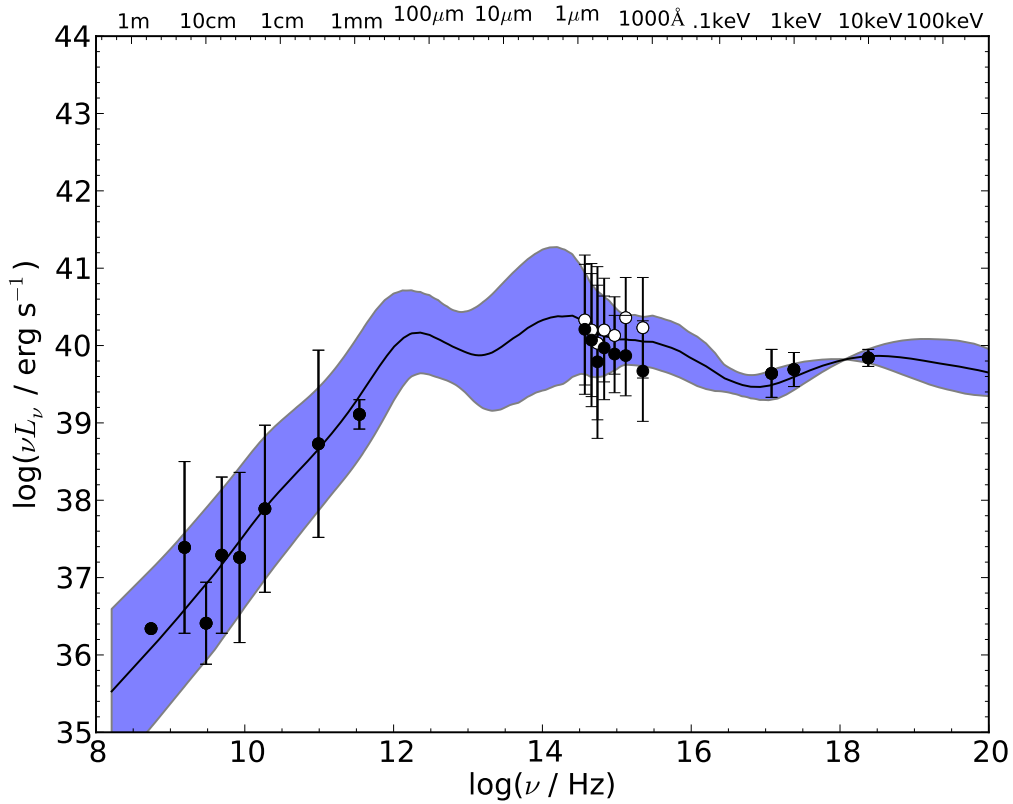


Figure 1.3: An average spectral energy distribution (SED) computed for RIAF model (Nemmen et al. (2014a)). The data points correspond to the geometric mean of high spatial resolution optical and UV observations, X-ray observations from Chandra, and high-resolution radio observation from Very Large Array (VLA) or VLBA/VLBI for 35 LLAGNs (Eracleous et al. 2010). The error bars show the scatter in the measurements. In the OUV, the open and filled circles correspond to the measurements with the maximal extinction correction and without any extinction correction, respectively. The black solid line is the average RIAF SED with the standard deviation shaded.

Since the dominant fraction of the released energy by viscous dissipation is retained in gas, the gas pressure and sound speed are large. The sound speed, c_s , is approximately equal to the Keplerian velocity, v_k , where $v_k(R) = c/\sqrt{2r}$ with $r = R/R_S$, implying the gas temperature is nearly virial. Due to large pressure, the accretion flow becomes geometrically thick with a vertical height H approximately equal to its radius R . Also, the radial velocity of the gas is relatively large. The large scale height and large velocity cause the gas density to be low, so the medium is optically thin. At such low densities, coupling between electrons and

protons via Coulomb collisions is inefficient. Irrefutably, the electrons radiate much more efficiently than protons, and therefore, the protons are much hotter than the electrons, making the accretion flow two-temperature plasma. Consequently, the spectra produced by RIAF are not multi-temperature black body produced by standard accretion flow. Instead, they exhibit multiple peaks across different frequencies due to synchrotron, inverse-Compton, and Bremsstrahlung emission (see Figure 1.3).

Transition from a Shakura-Sunyaev disk to a RIAF (Figure 1.4): The current view is that the Shakura-Sunyaev disk or the thin disk extends up to a certain radius called the truncation radius, R_{tr} , beyond which the accretion flow transitions to hot-RIAF (Done et al. 2007). Although the issue of disk truncation is still an open question, it is expected that R_{tr} decreases with increasing accretion rate. Due to shorter thermal and dynamical timescales in black hole X-ray binaries (BHXBs), the transition from a thin, radiatively efficient state to a RIAF state as the accretion rate decreases, and vice versa can be observed, which can be scaled up to AGNs (McHardy et al. 2006).

Jets: A fundamental characteristic of RIAFs is their enhanced capability to launch magnetically driven outflows, such as winds and jets, more effectively than the traditional Shakura-Sunyaev thin disks (Blandford & Begelman 1999b). This efficiency in RIAFs is due to their ability to capture and channel large-scale magnetic fields toward the black hole (Livio et al. 1999). Additionally, the substantial pressure within these thick flows aids in collimating jets (McKinney 2006, Globus & Levinson 2016, Chatterjee et al. 2019). Consequently, systems with lower accretion rates are more likely to launch jets (Ho 2008).

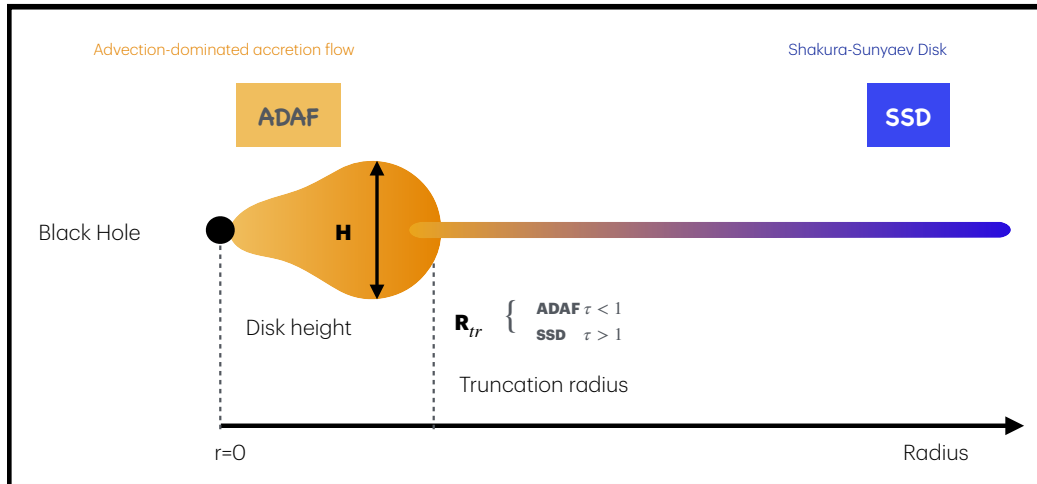


Figure 1.4: A schematic diagram showing the two accretion flow regimes in LLAGNs.

1.3 Active Galactic Nuclei

As discussed in Section 1.1, almost all massive galaxies host a supermassive black hole (SMBH) at their center [Kormendy \(2004\)](#), which, when actively feeds on the matter and gas surrounding it, powers what we call an Active Galactic Nuclei (AGN). These are the most luminous persistent sources emitting across the entire electromagnetic spectrum, outshining the emission from the host galaxy.

1.3.1 A brief history of AGNs

At the start of the 20th century, the emission lines from the galaxy nuclei were already known, but it wasn't till the 1990s that AGNs drew attention. In 1909, E.A. Fath ([Fath 1909](#)) at Lick Observatory studied spiral 'nebulae' including NGC 1068* and M81†, which were at that time believed to be in the Milky Way. The detection of bright and strong emission lines challenged their existence in the Milky Way.

*NGC stands for New General Catalogue ([Dreyer 1888](#))

†M stands for Messier Catalog of Nebulae and Star Clusters by Charles ([Messier 1781](#))

Fath's observations contributed to the growing evidence that spiral nebulae were actually independent galaxies, a notion that Carl Seyfert would later confirm in 1943 (Seyfert 1943). Seyfert's systematic spectral analysis of nearby spiral galaxies, including NGC 1068, showed very bright cores and unusually broad emission lines, leading to a new class termed Seyfert galaxies. Radio astronomy, pioneered by Karl Jansky, was a significant catalyst in understanding AGN. The detection of radio emission from outside our solar system (Jansky 1933, Reber 1944), followed by the first radio surveys and several catalogs, e.g., Third Cambridge Catalogue of Radio Sources (3C), paved the way for the discovery of quasi-stellar radio sources, or *Quasars*. In the early 1950s, Professor Victor Ambartsumian introduced the concept of Active Galactic Nuclei (AGN) at the 1958 Solvay Conference on Physics in Brussels. He theorized that massive explosions in galactic nuclei expelled large amounts of mass and indicated the presence of enormous, enigmatic objects within these nuclei. In 1954, astronomers Baade and Minkowski connected the powerful radio source Cygnus A to a faint galaxy with two nuclei (Baade & Minkowski 1954a), for which a mechanism of two giant galaxies colliding was proposed. Victor A. Ambartsumian noted deficiency in the collision model and introduced Active Galactic Nuclei (AGN) at the 1958 Solvay Conference on Physics in Brussels. He theorized that massive explosions in galactic nuclei expelled large amounts of mass and indicated the presence of enormous, enigmatic objects within these nuclei (Blaauw 1997). Decades later, his student Benjamin Markarian (known for Markarian galaxies) conducted UV excess galaxy surveys at Byurakan Observatory, which revealed a significant number of Quasars and AGN. The first quasar to be identified was 3C 273. In 1963, Hazard et al. (1963a) and Schmidt (1963) studied this source using lunar occultation and optical observations, respectively. It was established that 3C 273 is an extragalactic object at redshift $z = 0.158$ with a very

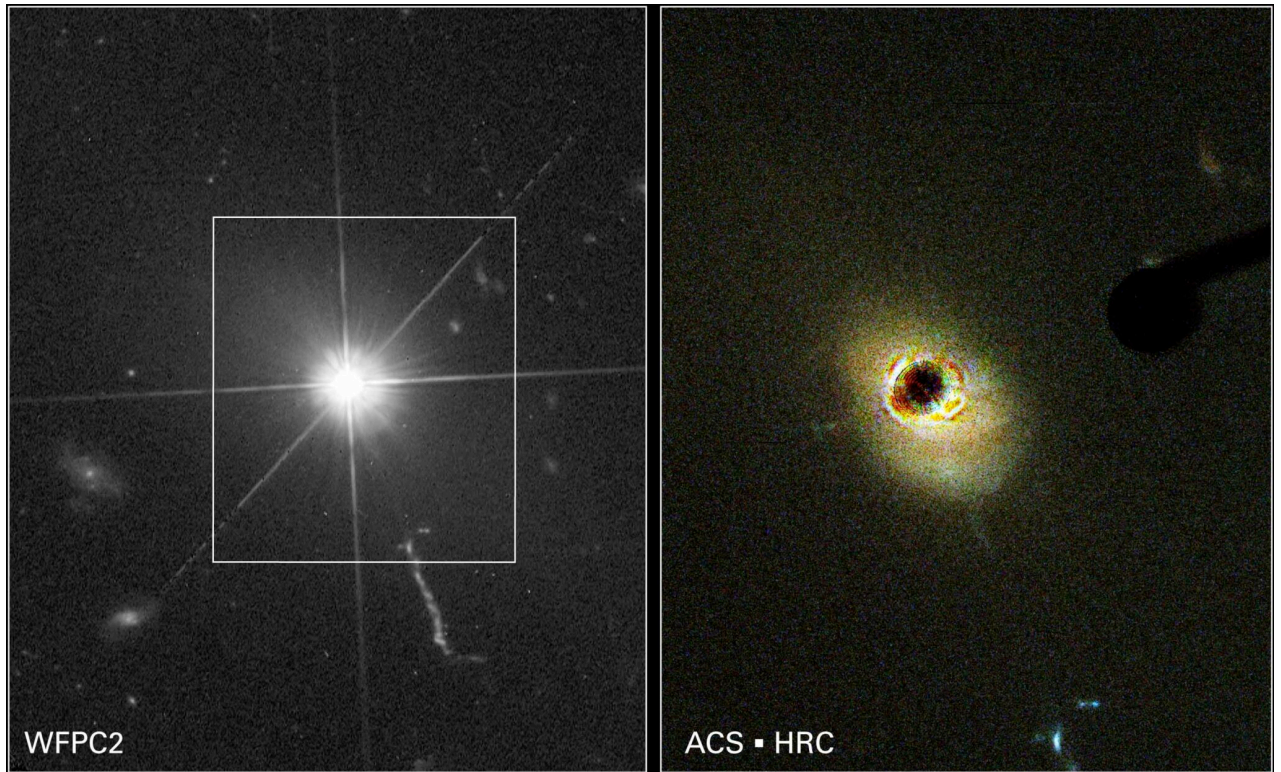


Figure 1.5: Hubble Space Telescope images of the host galaxy of Quasar 3C 273. A coronagraph is employed on the right to obscure the quasar's light, revealing the surrounding galaxy. Credit: NASA/ESA

bright nuclear region outshining the rest of the galaxy in optical (see optical image by Hubble Space Telescope in Figure 1.5; Schmidt 1963, Oke 1963). Since then, many quasars have been detected, with the farthest quasar J0313-1806 at $z = 7.4$ (Wang et al. 2021).

The emission mechanism, which was powerful enough to cause the observed brightness in these systems, was a big enigma. The first step in this direction was to determine the size of the compact nuclear region of these active galaxies. In 1959, two papers in the *Astrophysical Journal* revisited Seyfert's work. Burbidge et al. (1959) concluded that NGC 1068's high gas velocities suggested ejection from its nucleus, while Woltjer (1959) argued that the gas in six Seyfert galaxies was contained by the gravity of a massive body, now known to be a black hole. Both findings were correct and suggested massive cores with $\sim 10^8 M_{\odot}$. In 1963, it was

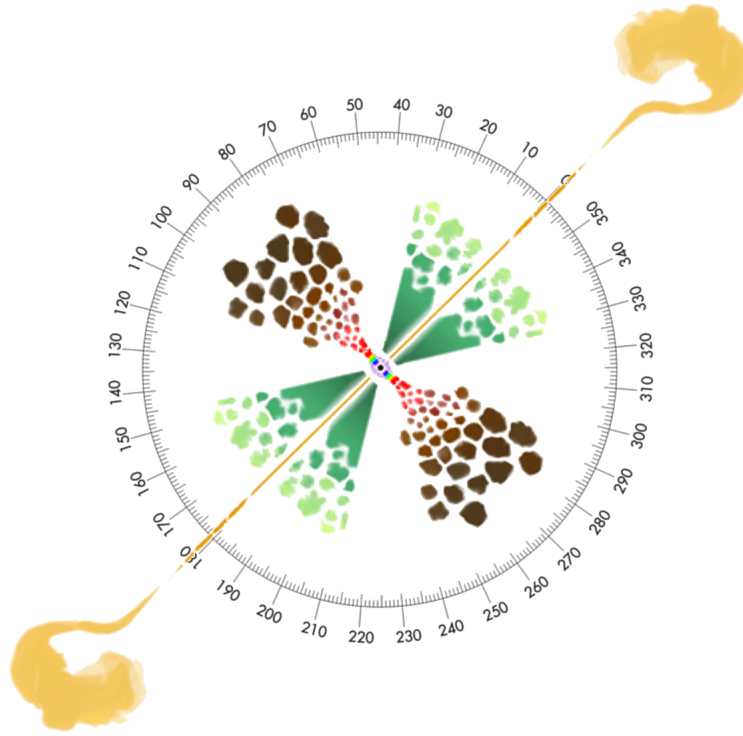


Figure 1.6: Structural components in an AGN with typical scales. Red, brown, green, and yellow represent the disk, dusty torus, BLR & NLR, and double-sided jets, respectively. Image taken by Marin (2016)

proposed that such massive energy outputs could be explained by matter accretion onto a stellar-sized massive object (Hoyle & Fowler 1963). Following this, it was established that the massive object is a supermassive black hole, and the accretion of gas onto these is the reason behind their brightness (Salpeter 1964, Zel'dovich & Novikov 1964, Lynden-Bell 1969). The accretion process is discussed in detail in Section 1.2.

1.3.2 Structural Components of AGN: A General Picture

An AGN, in general, is believed to host several spectral components (as can be seen in Figure 1.6), as listed below.

- Accretion Disk

As discussed in Section 1.2, an accretion disk is formed around the SMBH

due to accretion onto SMBH. Depending on the accretion rate, the structure and physics of the accretion disk differ in different systems. For example, in luminous AGNs, that is, AGNs accreting at $\lambda_{Edd} \sim 1 - 10$, a Shakura-Sunyaev disk which is geometrically thin, is formed. As seen before, it emits multi-temperature black body emission, which peaks in the UV to optical energies range. This emission is often called the ‘big-blue bump’ and is a common characteristic of spectral energy distribution (SED) of luminous AGNs. This big-blue bump is missing in the SEDs of low-luminosity AGNs, which are AGNs accreting at an Eddington rate $\lambda_{Edd} < 0.01$. This absence of a big blue bump is expected owing to the lack of a standard Shakura-Sunyaev disk in the inner region around SMBH. Instead, they show an ‘big-red bump’, peaking at mid-infrared energies, owing to the truncated standard disk in the outer region around the SMBH. As shown in Figure 1.1, the left panel shows how the peak of the spectrum shifts to the right to bluer energies with increasing accretion rates. The middle panel in the figure shows that as the truncation radius increases outwards, the peak gets redder, and thus, the red bump. In a nutshell, in the case of LLAGNs, there are two components: RIAF in the inner region, which truncates at transition (or truncation) radius and switches to standard Shakura-Sunyaev disk (Figure 1.4).

- Broad-Line Region (BLR)

The broad-line region is an important probe of the BH at the center. For example, the mass of central BH can be derived using the virial theorem once BLR size is measured,

$$M_{BH} = f_{virial} R v^2 / G \quad (1.14)$$

where f_{virial} is the virial factor that considers the geometry of BLR, R is the ra-

dius of BLR, v is the rotational speed of BLR, and G is the gravitational constant. Although the nature of BLR remains elusive, one major model class assumes discrete clouds in BLR. The high-density ($\sim 10^{10}\text{cm}^{-3}$), dust-free gas clouds move around the BH with Keplerian velocities at a luminosity-dependant distance determined using $L/4\pi r^2$ (0.1-1 pc for Seyfert galaxies). The photons from the accretion disk in the UV/optical energy range photoionize the clouds in BLR. These emission lines are Doppler-broadened due to the high velocity of the cloud around the compact, massive BH. Their widths vary from $\Delta v_{\text{FWHM}} \approx 500 \text{ km s}^{-1}$ to $\Delta v_{\text{FWHM}} \geq 10^4 \text{ km s}^{-1}$, with a typical value of 5000 km s^{-1} . We only see broad emission from permitted line transitions (hydrogen Lyman and Balmer series, Mg II, He II, Fe II, C IV, etc.), implying collisional de-excitation due to the high density of the clouds. However, BLR cannot be sustained in a LLAGN due to their low accretion rates, which sets a physical upper limit on the width of the broad-line [Laor \(2003\)](#). If the LLAGNs follow the same BLR-luminosity relationship as higher luminosity AGNs, the BLR velocity depends on BH mass and luminosity. Using Eddington luminosity and Equation [1.14](#), we can obtain,

$$\Delta v = 10^{10.85} \sqrt{M_{\text{BH}} L}^{-1/4} \quad (1.15)$$

This implies, as M_{BH} increases and L decreases (i.e, λ_{Edd} decreases), the width Δv increase. Therefore, at a limiting luminosity $L \approx 10^{41.8} (M_{\text{BH}}/10^8 M_{\odot})^2 \text{ erg s}^{-1}$, width $\Delta v \approx 25000 \text{ km s}^{-1}$. Above this limit, the BLR cloud cannot survive due to interactions with the surrounding mediums or large velocity shears and tidal forces within the BLR.

In other words, as the BLR radius shrinks with decreasing $L_{\text{bol}}/L_{\text{Edd}}$ or λ_{Edd} , where $L_{\text{bol}} = 1.3 \times 10^{38} (M_{\text{BH}}/M_{\odot}) \text{ erg s}^{-1}$, the BLR is expected to disappear

for $\lambda_{Edd} \leq 10^{-3}$, where the width of the emission line exceeds $25,000 \text{ km s}^{-1}$.

- Narrow-Line Region (NLR)

NLR exists on the extended scale at a distance of hundreds of parsecs with low density ($\sim 10^4 \text{ cm}^{-3}$; Netzer 2013). In some cases, these regions may extend up to several kilo-parsecs, which we refer to as extended NLR (ENLR). The NLR region produces intense semi-forbidden and forbidden emission lines along with permitted emission lines. The latter is due to low densities in NLR, which allow only a few collisions, and thus, forbidden lines are maintained for a longer time to produce intense emission lines. As the name suggests, the emission lines produced in NLR are narrower than those made in BLR (Netzer 2013, 2015). The material in NLR is highly ionized, and these are (bi)conically shaped, also referred to as ionization cones.

For LLAGN, which often includes low-ionization nuclear Emission-line Regions (LINERs), the ionization is typically softer, and the emission lines, although strong, are less ionized compared to their high-luminosity counterparts. LINERs, for example, show less doubly-ionized oxygen emission, suggesting a less intense ionizing radiation field, likely due to low-rate accretion processes onto the SMBH (Kewley et al. 2006).

- Dusty Torus

A dusty torus plays a pivotal role in the unified theory of active galactic nuclei (AGNs), which posits that all AGNs are essentially ‘born equal’ (Antonucci 1993, Urry & Padovani 1995). However, as discussed in this thesis, the accretion rate onto the black hole is another crucial element.

The idea for forming the torus is that the central accretion disk extends across several parsecs. At a certain point away from the center, some of the gas in this disk gets hot enough to rise. The torus is mainly made up of grains of

graphite and silicate, which, when sufficiently heated ($\sim 1200 - 1500$ K) by optical/UV emission from the accretion disk and BLR, reradiates the absorbed energy in the infrared (IR), for lines of sight which pass through the torus. Observationally, the torus is identified by its ability to obscure X-rays and re-emit absorbed UV-to-optical light in the mid-infrared, altering the AGN's intrinsic SEDs. X-ray observations allow us to constrain the density of the obscuring column in many of these sources, which may range from 10^{22} cm^{-2} to more than 10^{24} cm^{-2} . Despite some progress, the structure remains elusive due to its small scale (e.g., NGC 1068: Imanishi et al. 2018, García-Burillo et al. 2019). Although its geometry and composition are still debated, there are multiple models like smooth tori, clumpy tori, or a mix of both to explain its structure based on the study of the SED, especially in the mid-infrared (MIR) range (see González-Martín et al. (2019a,b) for a complete review on dusty torus models).

Like the BLR region, the dusty torus also disappears in LLAGNs due to low radiative pressure from the disk to sustain the structure (Hönig & Beckert 2007). Additionally, the disappearance of the torus is supported by observations of weak or undetected Fe $K\alpha$ emission and low absorbing column densities, indicating a direct, unobstructed view of the nucleus (Chiaberge et al. 1999, Donato et al. 2004, Balmaverde & Capetti 2006).

- Jet and lobes

Jets consisting of hot plasma are emitted from the central regions of galaxies, extending distances that can exceed the host galaxy's size. These jets, propelled by collimated magnetic fields associated with the accretion disc, travel through the medium at relativistic speeds. They are observable across various wavelengths, such as optical (e.g., M87) and X-rays (e.g., NGC 315). De-

spite the majority of AGNs being radio-quiet—over 90% according to [Padovani et al. \(2011\)](#) — they may still possess relativistic jets. This observation led [Padovani et al. \(2017\)](#) to propose a reclassification of AGNs based on the presence of jets, suggesting categories of ‘jetted’ or ‘non-jetted’ rather than ‘radio-loud’ versus ‘radio-quiet’. More about jets is covered in [Section 1.4](#) since we study the non-thermal emission from this structural component of AGNs in this thesis. In most AGNs, particularly radio galaxies (see [Section 1.3.3](#)), jet terminate into radio lobes, which are extended structures of synchrotron emission (can be seen in [Figure 1.9](#)).

1.3.3 AGN Zoology and Unification

AGNs emit light across the electromagnetic spectrum, but research often focuses on specific properties. This approach has led to a confusing array of classifications, where very similar objects are categorized differently ([Padovani et al. 2017](#)). Whether this taxonomical categorization has simplified or complicated our understanding of AGNs is debatable. Yet, to indeed join the conversation, one must first master the language.

The standard Unification Model of AGNs ([Urry & Padovani 1995](#)) is based on the principle that all AGNs share the same structure: a supermassive black hole (SMBH) at the center surrounded by an accretion disk and a dusty torus ([Figure 1.7](#)). The classification of AGNs depends on the angle at which the AGN is viewed. If the torus is edge-on, it can block the broad line region (BLR) and the accretion disk, leading to a classification as a Type 2 AGN, which exhibits only narrow emission lines. Conversely, if the torus is face-on, broad and narrow emission lines are visible, resulting in a Type 1 AGN classification. Additionally, for jetted AGNs, if the line of sight is closely aligned with the jet (i.e., $\theta \lesssim 10^\circ$), the AGN is classified as a

blazar. If the jet is not closely aligned with the line of sight, the AGN is classified as a radio galaxy. For different classes and acronyms in the field of AGN, one may refer to Table 1 of Padovani et al. (2017).

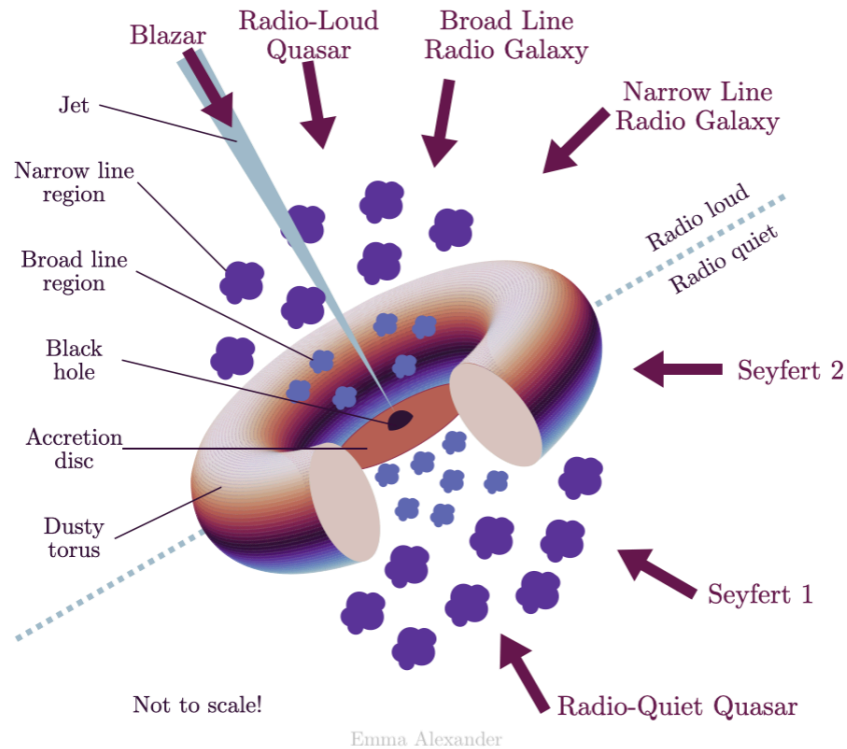


Figure 1.7: Schematic representation of standard unification model of AGN by Urry & Padovani (1995). Image by Emma Alexander: <https://emmaalexander.github.io/resources.html>.

However, the rate at which material accretes onto these supermassive black holes (SMBHs) can significantly impact the accretion process within these systems. Consequently, this distinction leads to the categorization of AGNs into two broader classes, which we use: AGNs and low-luminosity AGNs (LLAGNs). This distinction can be visualized as demonstrated in Figure 1.8. When the SMBH accretion rate falls below 0.01 times the Eddington luminosity (L_{Edd}), the kinetic energy is advected into the SMBH instead of radiating away. In this scenario, the accretion flow is classified as radiatively inefficient accretion flow (RIAF; Section 1.4.2). LLAGNs are typically powered by RIAFs. Although RIAFs are inefficient at converting ac-

creting matter into radiation, they are known to be very efficient at producing jets and outflows.

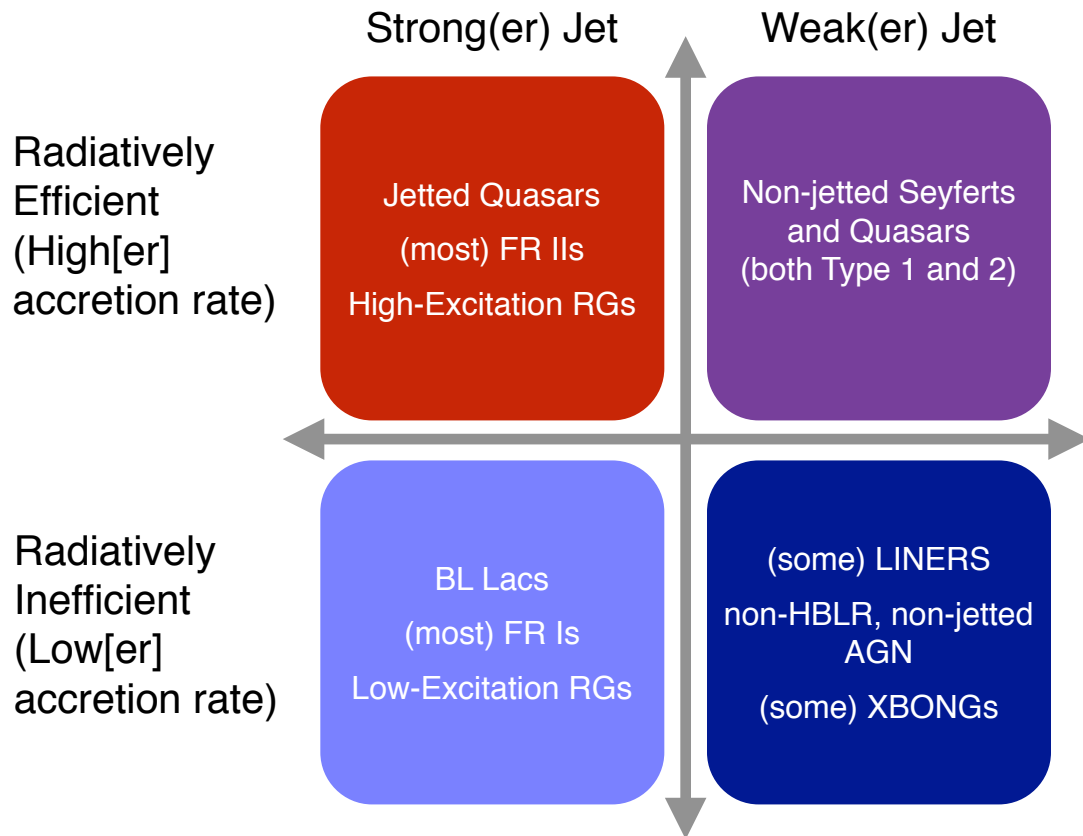


Figure 1.8: A schematic illustration of unification model for different classes of AGNs based on radiative efficiency and strength of jet, taken from Padovani et al. (2017).

1.4 Jets

A curious straight ray lies in a gap in the nebulosity in p.a. 20°, apparently connected with the nucleus by a thin line of matter. The ray is brightest at its inner end, 11'' from its nucleus.

- Curtis (1918)

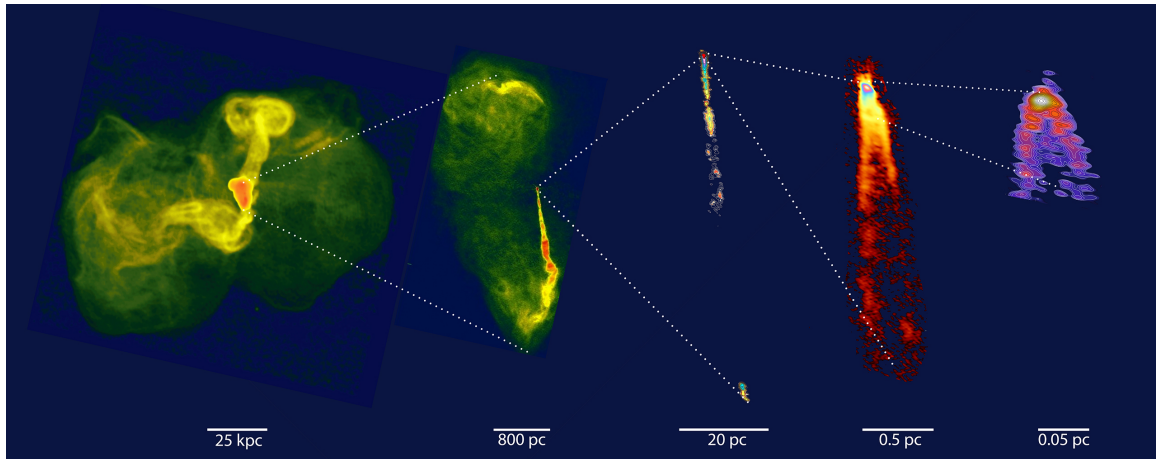


Figure 1.9: A montage taken from (Blandford et al. 2019), showing the jet (or outflow) LLAGN M87 (or better known FRI radio galaxy) at different scales, from its large outer lobes to the area close to its central SMBH.

The quote mentioned above describes a “curious straight ray” feature observed in the galaxy NGC 4486, also known as M87, with a 5-min exposure in the optical waveband (also see Figure 1.9). This “ray” he described is one of the earliest observations of a jet emanating from an AGN. These jets are now understood to be powerful collimated streams of ionized matter propelled at high speeds from the regions close to SMBHs at the centers of galaxies. These jets are often launched due to black hole accretion and can contribute to the observed SED or even dominate it. Radio astronomy led to the discovery of two distinct radio lobes in Cygnus A (Jennison 1959), and its identification with a distant galaxy (Baade & Minkowski 1954b). A year later, synchrotron radiation was identified as the origin for the observed radio emission (Shklovskii 1955, Burbidge 1956). 3C 273, the first quasar to be discovered (Hazard et al. 1963b, Schmidt 1963) also hosts a linear jet extending to 20 arcsecs, with a flat radio spectrum core. As quasars are AGNs that outshine their host galaxy, early models correctly predicted accreting SMBHs (Salpeter 1964, Zel’dovich & Novikov 1964). It was soon revealed that jets from galactic nuclei, rather than supernova remnants, continuously power double radio sources (Rees 1971). Unlike accretion flows, the emission from the jets is non-thermal and more

variable, spanning several orders of magnitude in frequency from radio to gamma-ray. These observations imply that the magnetic fields are a crucial jet component. Consequently, the synchrotron is the fundamental emission mechanism in the jets.

1.4.1 Jet launching and collimation

The formation, acceleration, and confinement of relativistic jets in AGN remain open questions and an enigma in the AGN research community. The predominant theory posits that magnetohydrodynamic (MHD) mechanisms primarily drive these jets. In these scenarios, magnetic fields are anchored in the rotating accretion disk or directly interact with the spinning black hole twist and amplify due to the differential rotation of the disk. This magnetic coiling acts as a sling, accelerating charged particles to relativistic speeds and channeling them into narrow, collimated jets. Two key MHD processes include the Blandford-Znajek (BZ) mechanism (Blandford & Znajek 1977), which extracts energy from the spin of black holes, and the Blandford-Payne (BP) mechanism (Blandford & Payne 1982), which leverages the rotational energy of the accretion disk. The distinction between the jet's power and speed in these BZ and BP mechanisms is crucial for understanding the diverse observational properties of jets in different AGNs (Tchekhovskoy et al. 2011). BP jets are powered by the energy and spin of the accretion disk around a black hole, but there's only so much energy available in the disk, so these jets can't get more powerful than the disk allows. On the other hand, BZ jets draw power directly from the black hole's spin, which can be much more significant, allowing these jets to be faster and more potent than BP jets. BP jets typically reach moderate speeds with Lorentz factors around a few, making them fast but not as extremely high-speed as BZ jets, which can achieve much higher velocities with Lorentz factors up to 10 or more.

1.4.2 Accretion flows and outflows

Radiatively inefficient accretion flows (RIAFs) produce jets and outflows more efficiently than standard accretion flows (Blandford & Begelman 1999b). In RIAFs, most of the gravitational energy of infalling matter is not radiated away but is instead converted into kinetic energy for jets. The low-density, high-temperature plasma in RIAFs generates strong magnetic fields, crucial for jet formation through mechanisms like the BZ and BP processes. These magnetic fields efficiently extract rotational energy from the black hole and drive jets via magneto-centrifugal forces (Yuan & Narayan 2014). Additionally, the high thermal and magnetic pressures in RIAFs enhance jet collimation and acceleration to relativistic speeds (McKinney, Tchekhovskoy, & Blandford 2012). In contrast, standard accretion flows radiate away much of their energy, resulting in weaker magnetic fields and less efficient jet production. The slower angular momentum transfer in standard accretion flows further limits the amplification of magnetic fields necessary for powerful jets (Narayan & McClintock 2012). These combined factors explain why RIAFs produce jets and outflows in AGNs more effectively.

1.4.3 Feedback process

AGNs impact their host galaxies and the surrounding intergalactic medium (IGM) and play a key role in galaxy evolution (Harrison et al. 2018). This impact occurs through two main feedback modes: radiative (or quasar) mode and kinetic (or jet) mode, determined by AGN's luminosity and accretion rate. The radiative mode is associated with high-luminosity AGNs that are radiatively efficient. In this mode, large amounts of gas are expelled from the galaxy to relatively small distances, leading to potential gas depletion in the host galaxy (Fabian 2012). On the other

hand, the kinetic mode is typical of low-luminosity AGNs that are radiatively inefficient (Fabian 2012). These AGNs usually have significant radio emissions and drive energy through jets. This thesis will primarily focus on the emission from LLAGN jets.

1.4.4 Relativistic Effects

Observations reveal that matter within astrophysical jets often moves at relativistic speeds. The most compelling evidence is the observation of knots within these jets that move faster than light, a phenomenon known as apparent superluminal motion (Rees 1971). This effect is an optical illusion where objects traveling near the speed of light appear to exceed it. This effect is primarily observed in radio wavelengths using imaging arrays like VLBA but is also detectable in X-ray and optical bands; an example of this is illustrated in Figure 1.10 for a LLAGN M87. We consider the knot (or blob) D emitted from the core of M87 seen in Figure 1.10, moving at a relativistic speed $v = \beta c$. It moves along the jet from position D_1 to D_2 at an angle θ from the observer's line of sight (black arrow). The time interval between these two positions in the jet frame is given by,

$$\Delta t = t_2 - t_1 \tag{1.16}$$

However, the relativistic motion of the knot dilates the time observed in the observer's frame³. Therefore,

$$\Delta t_{\text{obs}} = t'_2 - t'_1 \quad (1.17)$$

$$= c\Delta t - v\Delta t \cos \theta \quad (1.18)$$

$$= \Delta t \left(1 - \frac{v}{c} \cos \theta\right) \quad (1.19)$$

Therefore, the apparent speed in the observer's frame is

$$v_{\text{app}} = \frac{v\Delta t \sin \theta}{\Delta t \left(1 - \frac{v}{c} \cos \theta\right)} = \frac{v \sin \theta}{1 - \frac{v}{c} \cos \theta} \quad (1.20)$$

This formula given by Equation 1.20 shows that the apparent velocity depends on both the jet's intrinsic speed and the observation angle. The apparent velocity reaches its maximum when $\cos \theta = \beta$. For high velocities (i.e., $\beta \approx 1$), the angle θ becomes very small. For small angles θ , $\cos \theta \approx 1 - \frac{\theta^2}{2}$ and $\sin \theta \approx \theta$. The bulk Lorentz factor Γ is defined as:

$$\Gamma = \frac{1}{\sqrt{1 - \beta^2}} \quad (1.21)$$

Therefore, for $\beta \approx 1$, Γ is large, and we can approximate β as $\beta \approx 1 - \frac{1}{2\Gamma^2}$. Thus, the angle θ can be approximated as $\theta \approx 1/\Gamma$. This *beaming effect* is, of course, valid for a single relativistic particle emitting isotropically, where the emission is beamed into a cone due to its relativistic motion, with an opening angle $\theta \approx 1/\gamma$, where γ is the Lorentz factor of the relativistic particle. Since almost all emitted photons are concentrated in the direction of motion due to the beaming effect, the number of photons emitted with $\theta \gg \frac{1}{\gamma}$ or $\frac{1}{\Gamma}$ is greatly reduced. This beaming effect

³ t'_2 and t'_1 are time in seconds corresponding to 2017 and 2012, respectively for Figure 1.10.

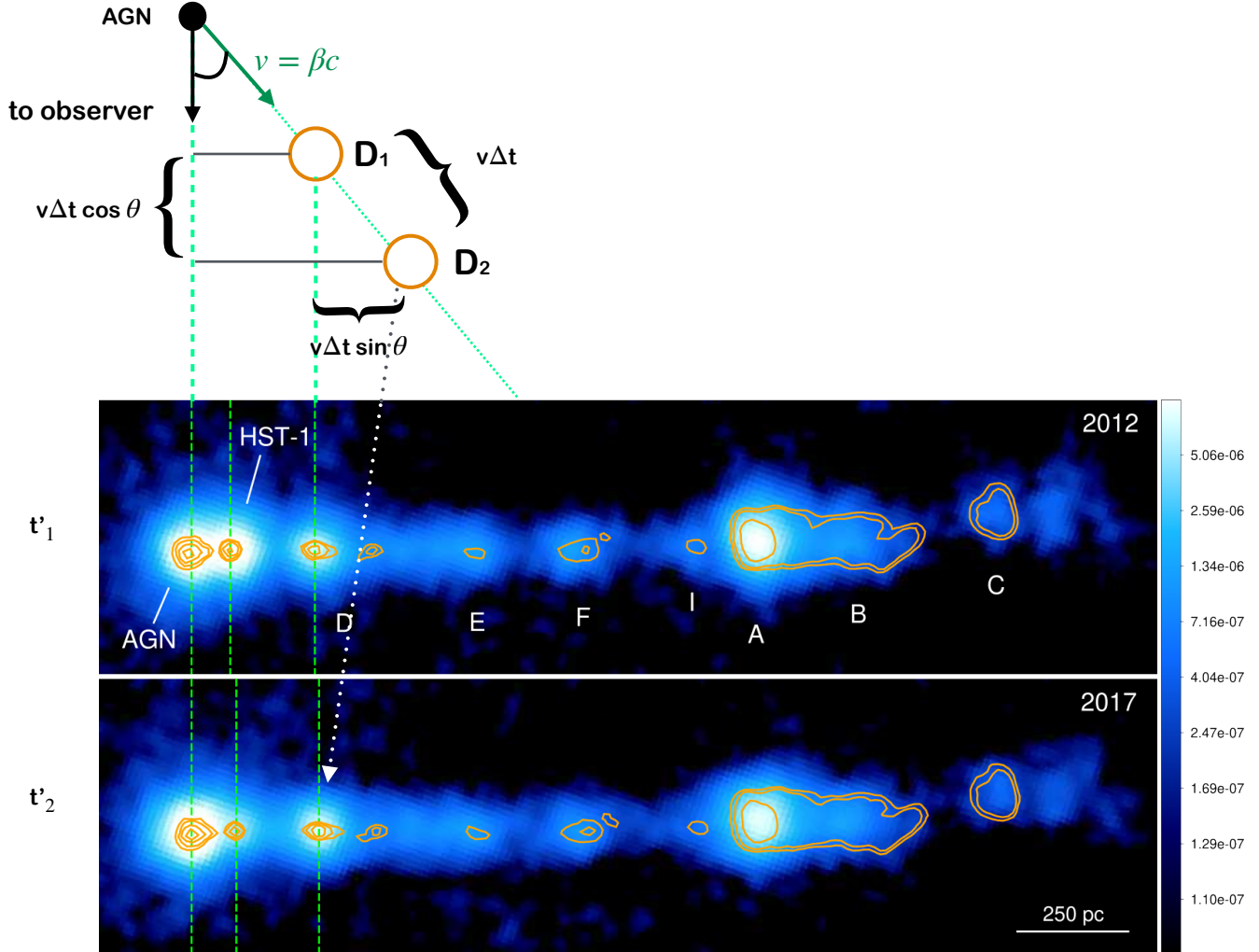


Figure 1.10: The two panels at the bottom show HST contours overlaid on the Chandra image for an LLAGN M87, taken from Snios et al. 2019. As seen by HST and Chandra, knots in these panels are labeled as HST -1, D, E, F, I, A, B, and C. To explain the superluminal motion, we consider the motion of knot D along the jet from position D1 (imaged in 2012, t'_1) to D2 (imaged in 2017, t'_2). θ is the angle between the jet motion and the observer's line of sight.

greatly amplifies the emission in the direction of motion, which can be quantified by *Doppler factor*, δ .

We can obtain the Doppler factor by considering the time delay effects (from Equation 1.19). The time interval between two successive wavefronts in the rest frame of the source is $T' = \frac{2\pi}{\omega'}$, where ω' is the angular frequency of the emitted wave in the rest frame of the source. Due to time dilation, the observed time interval Δt between these wavefronts in the observer's frame is related to the proper

time interval T' by the Lorentz factor Γ :

$$\Delta t = \Gamma T' = \Gamma \frac{2\pi}{\omega'}$$

The observed frequency can, therefore, be given by

$$\omega = \frac{\omega'}{\Gamma \left(1 - \frac{v \cos \theta}{c}\right)} \quad (1.22)$$

or

$$\omega = \delta \omega' \quad (1.23)$$

where Doppler factor, δ , is

$$\delta = \frac{1}{\Gamma \left(1 - \frac{v}{c} \cos \theta\right)} \quad (1.24)$$

Using the Doppler factor, we can write the observed intensity of emission from a homogeneous spherical blob emitting isotropically, as observed due to relativistic effects, as follows:

$$I_{obs} = \delta^4 I_{em} \quad (1.25)$$

where I_{obs} and I_{em} are the total intensities of the emission in the observed and emitted frames, respectively (Ghisellini 2013).

1.5 Emission Mechanisms of Jets

The distribution of charged particles in the homogeneous blob in the jet discussed above cannot be directly observed. Instead, only the radiation eventually emitted from those particles is observed. Therefore, to constrain the jet dynamics, we must discuss the processes that cause particles to lose their energy by emitting photons that we can detect as radiation. While the spectrum of stars is thermal, meaning we

observe a typical blackbody radiation spectrum, this is not the case for many non-stellar objects in the Universe, such as AGNs, where other emission mechanisms dominate the observations discussed below.

1.5.1 Synchrotron Emission

Many jets from AGNs have been seen in radio due to the synchrotron emission (first proposed by [Alfvén & Herlofson 1950](#)). This emission, also known as magnetobremsstrahlung, occurs when the distribution of relativistic charged particles, N , in the blob with the magnetic field, B , is subjected to Lorentz force.

The synchrotron power averaged over all pitch angles (i.e., angles between the magnetic field and the electron velocity) emitted from a single relativistic electron is given by:

$$P_{syn} = \frac{4}{3} \sigma_T c \beta^2 \gamma_s^2 U_B \quad (1.26)$$

where σ_T is the well-known Thomson scattering cross section, c is the speed of light, γ_s is the Lorentz factor for the particle β is the particle velocity (in units of c), and $U_B = \frac{B^2}{8\pi}$ is the magnetic field energy density in Gaussian units ([Rybicki & Lightman 1986](#)). Since $\gamma_s = \frac{E}{mc^2}$, synchrotron emission from electrons (and positrons) is more dominant than from protons of the same energy due to the lighter mass of electrons.

As discussed in Section 1.4.4, this radiation from highly relativistic electrons is beamed in the direction of their motion due to relativistic effects. This relativistic beaming transforms a particle's dipole emission into a narrow cone (as seen in the left panel of Figure 1.11), which results in a short pulse when directed at the observer. The particle emits most of the emission at one frequency referred to as critical synchrotron frequency ν_c (Figure 1.11; right), which is inversely proportional to the timescale during which the observer receives the pulse. This frequency is

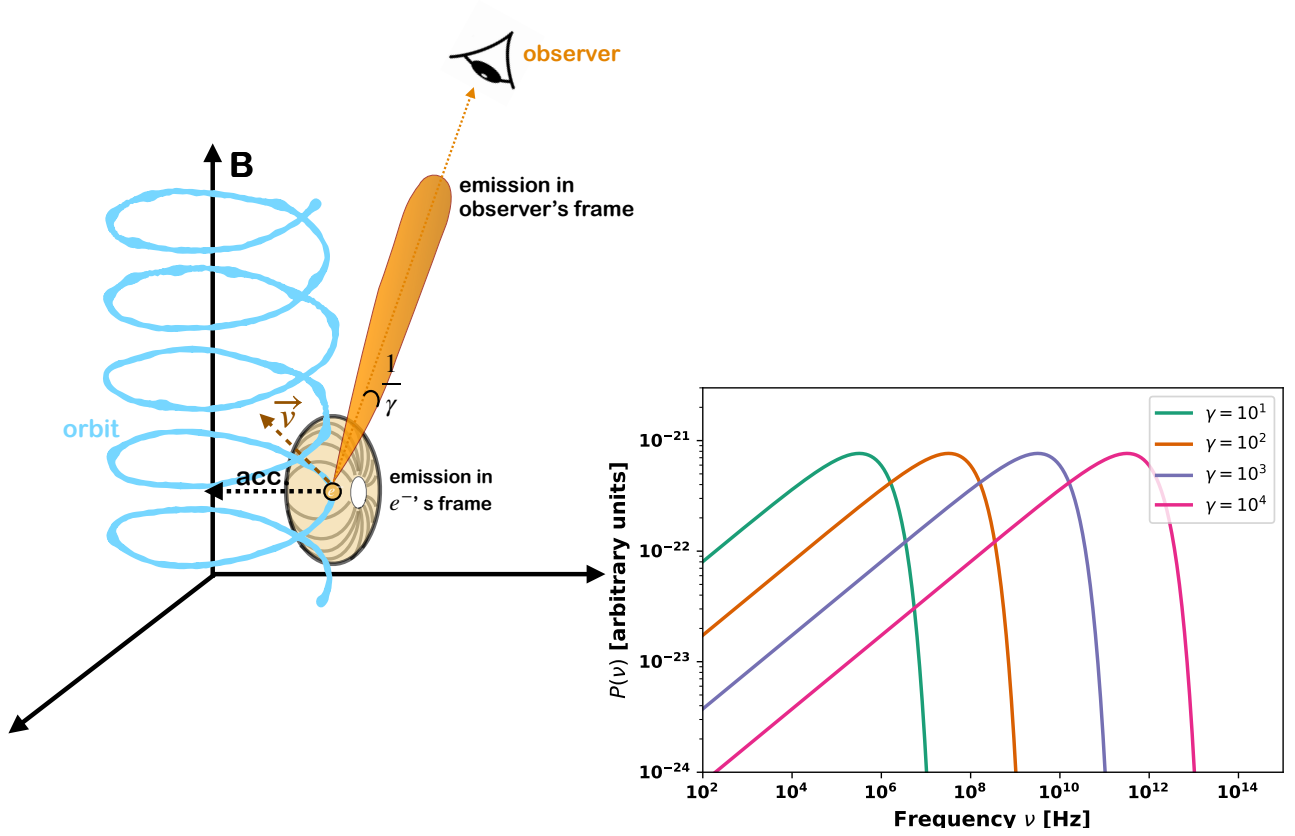


Figure 1.11: The geometry of synchrotron emission from a single relativistic electron with Lorentz factor γ in the electron's rest frame and observer's frame (left). The synchrotron spectrum from a single relativistic electron with different γ is shown (right).

given by,

$$\nu_c = \frac{3}{2} \gamma^2 \frac{eB}{2\pi m_e c} \quad (1.27)$$

The synchrotron spectrum, that is, the synchrotron power emitted by an electron of a given Lorentz factor and pitch angle per unit frequency, is given by

$$P_s(\nu, \gamma, \alpha) = \frac{\sqrt{3} e^3 B \sin \alpha}{m_e c^2} F\left(\frac{\nu}{\nu_c}\right) \quad (1.28)$$

with

$$F\left(\frac{\nu}{\nu_c}\right) \equiv \frac{\nu}{\nu_c} \int_{\nu/\nu_c}^{\infty} K_{5/3}(y) dy \quad (1.29)$$

where $K_{5/3}$ is the modified Bessel function of order $5/3$ and α is the pitch angle.

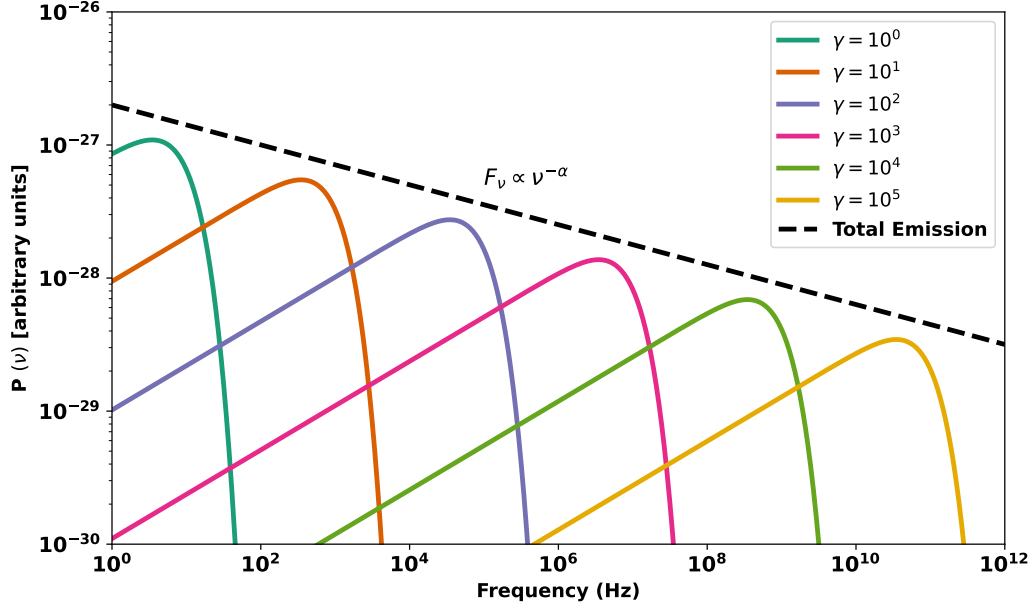


Figure 1.12: A schematic plot illustrating that a power-law distribution of leptons results in a total synchrotron emission spectrum that follows a power-law. This spectrum can be seen as the sum of the individual emission spectra from each electron in the lepton energy distribution.

In AGNs, the energy distribution of leptons follows a power-law distribution with an index p . The spectrum produced by this distribution is then obtained by folding this distribution with the angle-averaged synchrotron power of a single electron (Equation 1.28), which can be easily understood as the sum of each spectrum by the individual electrons in the distribution, as shown in Figure 1.10. That is, a power-law distribution of leptons produces a total synchrotron power-law spectrum (Rybicki & Lightman 1986; see Figure 1.12) described by:

$$P_{\text{tot}}(\nu) \propto \nu^{-\alpha} B^{1+\alpha} \quad (1.30)$$

where,

$$\alpha = \frac{p-1}{2} \quad (1.31)$$

x where α is the spectral index of the resulting radiation.

The same leptons that emit synchrotron emission may absorb these photons at a frequency below a threshold frequency, ν_t , where the optical depth is $\tau_\nu = 1$ ⁴. ν_t depends on the particle's energy and magnetic field as shown in Equation 1.32 (Ghisellini 2013). This process is called Synchrotron Self-Absorption. The distribution in this regime follows $B^{-1/2} \nu^{5/2}$ (Rybicki & Lightman 1986). As can be seen in Figure 1.13, the cutoff frequency is within the observable range only for large magnetic fields and Lorentz factors.

$$\nu_t \propto \gamma^{\frac{2(p+2)}{p+4}} B^{\frac{p+2}{p+4}} \quad (1.32)$$

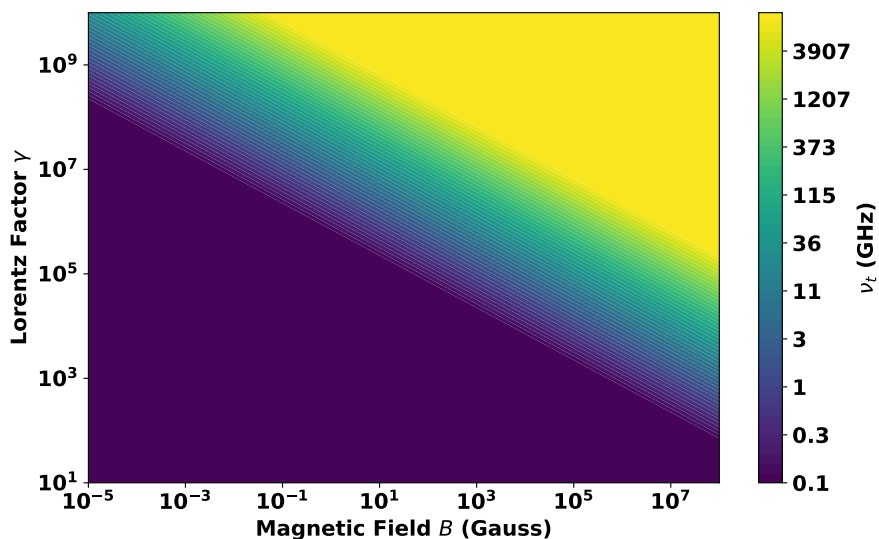


Figure 1.13: Contour plot showing the self-absorption frequency ν_t as a function of the magnetic field B (in Gauss) and the Lorentz factor γ . The color bar indicates the value of ν_t in GHz.

The synchrotron emission from the lepton population in the jets explains the origin of the low-energy bump (radio to soft/hard X-rays) in the observations of almost all jetted AGNs. However, the origin of the high-energy bump is still debated, with inverse Compton emission of the synchrotron photons being a leading

⁴Optical depth, here, is the measure of opacity that photons experience as they travel through a medium of relativistic electrons in a magnetic field.

contender. This mechanism and a few other proposed origins are discussed in the following sections.

1.5.2 Inverse Compton Emission

Inverse Compton (IC) scattering is the process where low-energy photons gain energy by scattering off relativistic electrons and thus producing high-energy photons. This process makes several photon fields of low-energy photons available as seed photons for upscattering. If synchrotron photons produced by relativistic electrons are up-scattered by the same electron population, this scenario is called Synchrotron Self-Compton (SSC; [Konigl 1981](#)). This process is efficient in AGN jets, where the magnetic field and electrons produce strong synchrotron radiation. SSC process has successfully explained the high-energy emission bump (soft/hard X-rays to gamma rays) in many jetted-AGNs, particularly blazars ([Rani et al. 2013](#), [de Menezes et al. 2020](#)).

In contrast, External Compton (EC) scattering involves seed photons originating from external sources such as the accretion disk, the broad line region, or the cosmic microwave background. These photons are up-scattered by the relativistic electrons in the jets ([Begelman & Sikora 1987](#)). This process is thought to dominate over SSC in high-redshift sources because the CMB photon field's apparent density is boosted for the relativistic plasma, often exceeding the magnetic field's energy density ([Ghisellini et al. 2014](#)).

There are two regimes for the IC process in astrophysical scenarios based on the energy of the incoming photon in the electron's rest frame: Thomson and Klein-Nishina. In the Thomson regime, where the photon's energy is less than the electron's rest mass energy ($m_e c^2 \approx 0.511$ MeV), the electron's recoil is negligible, and the scattering is approximately elastic and isotropic. In the Klein-Nishina regime,

the photon energy exceeds $m_e c^2$, and electron recoil is non-negligible, resulting in inelastic and anisotropic scattering.

If $U_r = \int \epsilon n(\epsilon) d\epsilon$ is the energy density of the seed photon field before scattering, the energy loss rate of the electron due to IC scattering can be written as:

$$P_{IC}(\gamma) = \frac{dE_e}{dt} = \frac{4}{3} \sigma_T c \gamma^2 \beta^2 U_r \quad (1.33)$$

This expression is similar to synchrotron energy loss, with the radiation energy density instead of magnetic field energy density (Rybicki & Lightman 1986). Therefore, in regions where relativistic electrons coexist with significant magnetic and radiation energy densities, they may emit energy through synchrotron and IC scattering processes. The ratio of the luminosities from these two processes can be expressed as:

$$\frac{L_{\text{syn}}}{L_{\text{IC}}} = \frac{P_{\text{syn}}}{P_{\text{IC}}} = \frac{U_B}{U_r} \quad (1.34)$$

where P_{syn} and P_{IC} denote the power emitted via synchrotron and Compton processes, respectively, and U_B and U_r represent the energy densities of the magnetic and radiation fields. This relation is mimicked in the similar shapes of the two bumps in the spectral energy distribution of blazars (see, for instance, SEDs of Fermi-bright blazars in Abdo et al. 2010a).

1.5.3 Hadronic Emission

Since the detection of Ultra-High Energy Cosmic Rays (UHECRs; $E \geq 10^{18}$ eV), relativistic jets of AGNs have been a promising site for the acceleration of protons and heavier nuclei. Recently confirmed association of neutrinos from two different jetted-AGN has further strengthened their role in accelerating protons to high energies (TXS 0506+056: IceCube Collaboration et al. 2018a, NGC 1068: IceCube

Collaboration et al. 2022) since neutrinos (and gamma-rays) are inevitable results of hadronic processes. Therefore, studying hadronic processes in these jets is crucial to understanding the behavior of relativistic jets in AGNs and their composition, which remains an open topic.

At very high energies, protons can interact with photons, leading to secondary particle production and high-energy emission in AGNs. For instance, photon-proton interactions can create an electromagnetic pair cascade, contributing to the high-energy spectrum. The primary interactions include photo-meson production ($p + \gamma \rightarrow p + \pi^0$), followed by a π^0 decay into two photons, neutron production ($p + \gamma \rightarrow n + \pi^+$), and electron-positron pair production via the Bethe-Heitler process ($p + \gamma \rightarrow p + e^+ + e^-$; Bethe & Heitler 1934).

1.6 Kilo-parsec jets from AGN

Jets are crucial sites for accelerating particles to relativistic energies, as evidenced by their detection in radio to up to gamma-ray energies, contributing to the production of high-energy cosmic rays and gamma rays. These jets can extend from the central supermassive black hole (SMBH) to distances of several hundred thousand parsecs (See Figure 1.14 for a schematic representation of multiple emission regions at different scales in the jet). Studying these jets provides crucial insights into fundamental questions related to jets, like collimation and composition. Additionally, emissions from kilo-parsec scale jets are essential to understanding extragalactic diffuse gamma-ray background (Stawarz et al. 2006). Electrons with Lorentz factors $\gamma >$ a few thousand cannot survive the journey from the SMBH to the jet ends due to efficient radiative cooling via synchrotron and IC processes. This suggests the presence of proton-dominated jets or re-acceleration processes for electrons along the jet length (Harris & Krawczynski 2006).

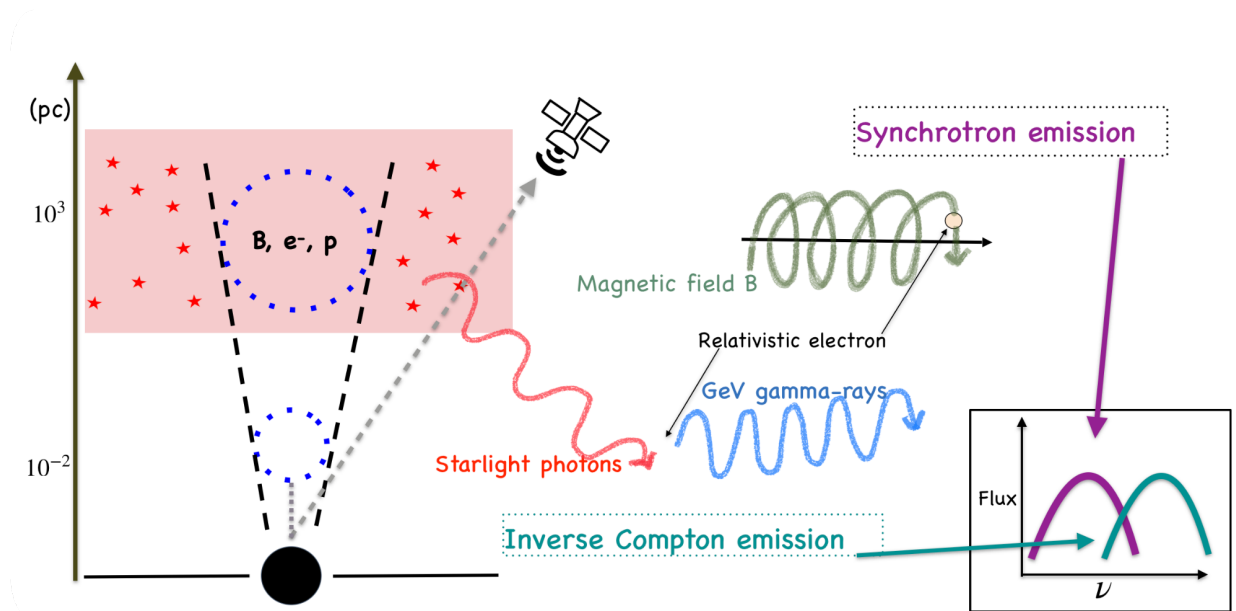


Figure 1.14: A schematic representation of emission regions located at different distances from the BH along the jet of an AGN with an inclination θ .

Chandra X-ray Observatory has been instrumental in detecting X-ray emission from many AGN jets up to kilo-parsec scales, identifying features such as knots and hotspots, where particle acceleration may occur⁵. The first high energy emission from a kilo-parsec scale jet was seen from quasar PKS 0637-752 with Chandra (Schwartz et al. 2000), which was interpreted as upscattering of the photons of Cosmic Microwave Background (CMB; IC/CMB; Tavecchio et al. 2000 Celotti et al. 2001) via IC process. This success has been followed by IC/CMB being a dominant model to explain the high-energy emission from the kilo-parsec jets of AGNs (Schwartz et al. 2020). However, IC/CMB interpretation to explain high-energy emission has its share of problems, such as requiring bulk Lorentz factor in the range $\sim 10 - 20$ and small viewing angles at kilo-parsec scale (Worrall 2009, Breiding et al. 2023). Alternatively, synchrotron emission from highly relativistic electrons has successfully explained X-ray emission from a few kilo-parsec scale jets, thus needing an in situ particle acceleration process (Harris & Krawczynski 2006).

⁵Chandra database for extragalactic Jets, XJET: <https://hea-www.harvard.edu/XJET/>

IC processes with other external photon fields (e.g., Broad Line Region (BLR), Dusty Torus (DT), or host galaxy starlight photons) have also been successful in explaining the origin of the high energy emission from the different scale jets of AGN like blazars and radio galaxies from different scales (Potter & Cotter 2013, Tanada et al. 2019). Although most of the current gamma-ray instruments do not have the resolution to isolate gamma-ray emission from the kilo-parsec scale jets, constraints on gamma-ray emission can help us understand the high-energy emission mechanism better (Rieger 2017). Evidence of very-high-energy (VHE) gamma rays from the kilo-parsec jet in Cen A has recently been reported by HESS collaboration, which has been successfully interpreted as IC/starlight emission with X-ray emission coming from the synchrotron processes (H. E. S. S. Collaboration et al. 2020a). A schematic picture of two different emission regions in the jet and their emission is shown in Figure 1.14. Similarly, for another low-synchrotron peaked blazar, AP Librae VHE is contributed by inverse-Comptonization of CMB or circumnuclear dust (Zacharias & Wagner 2016, Roychowdhury et al. 2022).

*With four parameters, I can fit an elephant, and
with five, I can make him wiggle his trunk.*

Von Neumann

2

Data Analysis and Multiwavelength Modeling

A typical spectral energy distribution (SED) of strongly jetted AGNs (particularly blazars) shows a double-bumped feature from radio to gamma-ray energies. The modeling of the multiwavelength SED helps us understand the particle acceleration, composition, and emission in these jets.

2.1 Gamma-Rays from Fermi Gamma-ray Space Telescope

Gamma rays are the most energetic part of the electromagnetic spectrum, and they offer insights into a wide range of powerful, non-thermal astrophysical phenomena. The Fermi Gamma-ray Space Telescope, named after high-energy physics pioneer Enrico Fermi and formerly known as the Gamma-ray Large Area Space Telescope (GLAST), is a space observatory surveying the sky in the gamma-ray energies from 8 keV to 300 GeV. Fermi advances the groundbreaking work of its predecessor, the 1990s Compton Gamma Ray Observatory (CGRO). It is an international and multi-agencies space mission, launched on June 11, 2008, at 12:05 PM EDT in the low-Earth orbit (at an altitude of 550 km and an inclination of 28.5°) by the National Aeronautics and Space Administration (NASA) on Delta II 7920-H. The Fermi spacecraft orbits the Earth in about 96 minutes. There are two instruments onboard Fermi: a Large Area Telescope (LAT; 20 MeV - 300 GeV) and a Gamma-ray Burst Monitor (GBM; 8 keV - 40 MeV). While GBM is used to study transient gamma-ray phenomena like gamma-ray bursts (GRBs), LAT is the primary instrument used to study galactic and extragalactic gamma-ray sources like Active Galactic Nuclei (AGN), pulsars, globular clusters, and starburst galaxies, among other high-energy sources. The Fermi operates in sky-survey mode, scanning the entire sky every 3.2 hours (\sim two orbits).

Since August 4, 2008, Fermi-LAT has provided continuous data, dramatically broadening our view into the high-energy Universe, and continues to be promising for decades to come (Thompson 2015, Thompson & Wilson-Hodge 2022). In recent decades, the Fermi Gamma-ray Space Telescope has achieved significant milestones in the field of high-energy and multimessenger astrophysics, including detecting GRB 170817A associated with a neutron star merger (Abbott et al. 2017)

and linking the blazar TXS 0506+056 to high-energy neutrinos (IceCube Collaboration et al. 2018b). It discovered the Fermi Bubbles (Su et al. 2010), identified novae as high-energy particle accelerators which were not expected to be gamma-ray sources before (Ackermann et al. 2014), and expanded the gamma-ray pulsar catalog¹. Fermi also placed constraints on dark matter models (Hoof et al. 2020) and provided insights into cosmic rays from supernova remnants (Ackermann et al. 2013).

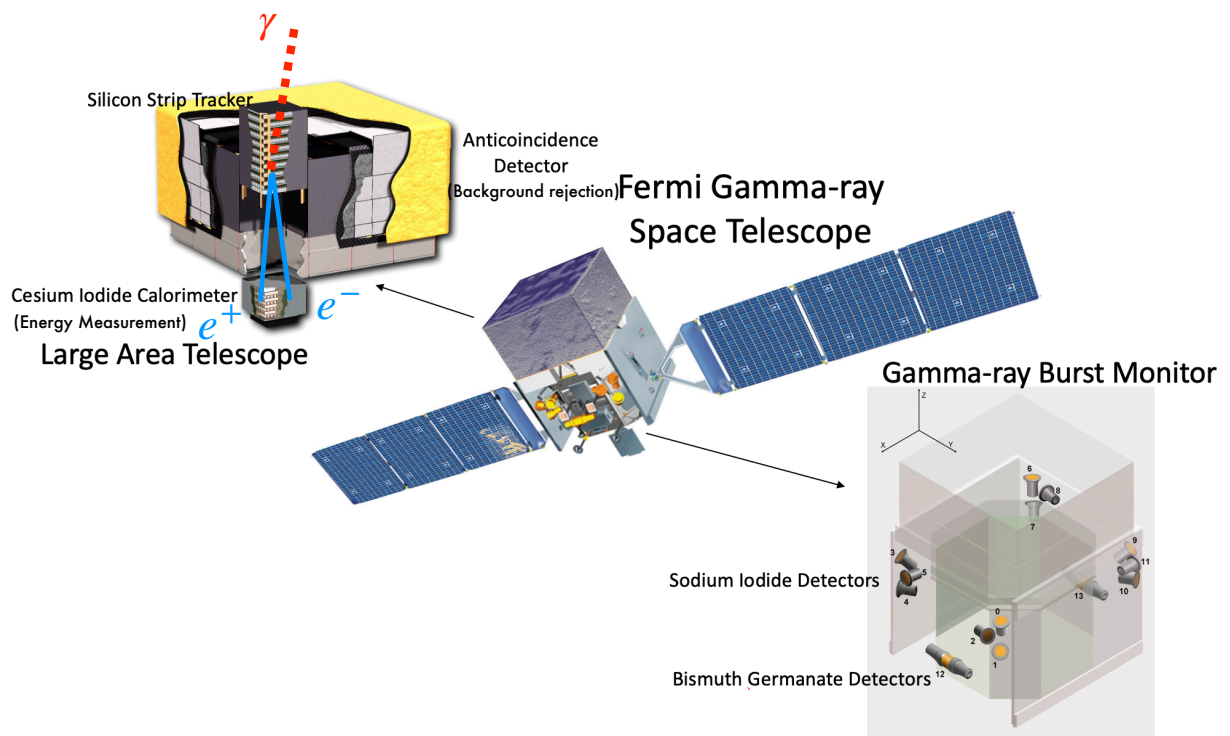


Figure 2.1: Fermi instrument taken from Thompson & Wilson-Hodge (2022)

2.1.1 Large Area Telescope

The Large Area Telescope (LAT) onboard the Fermi Gamma-ray Space Telescope works on the scientific principle of pair production, epitomizing Einstein’s famous equation, $E = mc^2$, by directly observing the conversion of energy into matter, an

¹<https://confluence.slac.stanford.edu/display/GLAMCOG/Public+List+of+LAT-Detected+Gamma-Ray+Pulsars>

electron and its antimatter, a positron. When high-energy gamma photons (red line; Figure 2.1) from cosmic sources strike the LAT's tungsten foils, they undergo pair production (blue lines; Figure 2.1), a process where the energy of the gamma-ray photon is transformed into mass, creating an electron-positron pair. These particles then pass through a series of high-precision silicon strip detectors that track their trajectories. By reconstructing these paths, the LAT determines the direction of the original gamma-ray photon. The instrument includes a calorimeter comprising 1536 cesium iodide logs stacked in 8 layers. The layers are oriented alternately in the x and y directions and are read out by custom photodiodes. The calorimeter measures the energy of the particles by absorbing them and converting their energy into light, detected by photodiodes. The LAT's anti-coincidence detector also helps differentiate between gamma rays and (background) charged cosmic rays, ensuring accurate gamma-ray detection. By combining the information from the tracker and the calorimeter, the LAT reconstructs the original direction and energy of the incoming gamma-ray photon. This data is then used to map the sky, with each detected photon contributing to a pixel in the gamma-ray image.

The LAT instrument works in the energy range of 20 MeV to 300 GeV. It has a wide field of view of about 2.4 steradians, allowing it to observe 20% of the sky at once and scan the entire sky every two orbits (~ 3.2 hours). The performance of the LAT is characterized by its Point Spread Function (PSF), which is its ability to determine the direction of incoming gamma rays. The PSF of LAT improves with increasing energy, with 0.6 degrees angular resolution at lower energies to achieving angular resolutions of around 0.1 degrees for higher energy (> 1 GeV) gamma rays (Atwood et al. 2009). This high-resolution capability ensures precise localization of gamma-ray sources, allowing for detailed mapping and study of high-energy phenomena in the Universe.

2.1.2 LAT Data Reduction and Analysis

To reduce and analyze the data from the Fermi-LAT, we require the installation of `Fermitools`² along with the `Fermipy`³ (Wood et al. 2017) python package, that provides users with a comprehensive set of functions to create desired science products, such as light curves and spectra, from Fermi-LAT data.

After the installation, we require the data. Since Fermi-LAT scans the entire sky every ~ 3.2 hours, the daily gamma-ray data is available for each position in the sky. The LAT collects data by recording discrete photon events and logging the spacecraft's status, including its position, orientation, and periods of high-background exposure, such as during passages through the South Atlantic Anomaly (SAA). Suffice to say, the LAT does not gather data while crossing the SAA or during rare events like software updates or spacecraft maneuvers. These photon events are stored in LAT event files, called the *photon files*, which are the primary data files. In contrast, the continuously logged information about the instrument's status is stored in *spacecraft files* at 30-second intervals. The LAT collects two types of photon files: standard photon files and extended photon files. Standard photon files provide the necessary details for most science analyses, such as each detected photon's time, energy, and position. Standard photon files are a subset of the extended photon files, with the latter containing additional information that aids in interpreting the results of the Level 1 analysis and includes extra photons classified under the TRANSIENT category. Level 1 files are processed and ready for scientific study, created from the raw 'Level 0' data sent down from the Fermi spacecraft. These photon and spacecraft files, which provide everything a user needs for analysis, are made publicly available on the website of Fermi Science Support Center

²Fermitools: <https://github.com/fermi-lat/Fermitools-conda/wiki>

³Fermipy: <https://github.com/fermiPy>

(FSSC)⁴ in FITS format shortly after downlinking.

To ensure accurate isolation and measurement of gamma-ray emission from our source of interest, it is necessary to account for the gamma-ray emission from all the nearby sources. This requires compiling a model that includes both point sources, such as blazars, and extended sources, like features of the Large Magellanic Cloud (Abdo et al. 2010b), using the latest release of the Fermi-LAT catalog. For this thesis, we use the second data release (DR2; Ballet et al. 2020) of the Fourth Fermi-LAT source catalog (4FGL; Abdollahi et al. 2020). In addition, diffuse background emission needs to be modeled. This includes all-sky models for both the Galactic diffuse emission (resulting from the interactions of cosmic rays with interstellar gas and dust in the Milky Way) and isotropic diffuse emission (from the faint, unresolved extragalactic sources distributed across the sky and residual cosmic rays)⁵. Furthermore, fermitools' package is used to convolve the emission of each source with the instrument response functions (IRFs, Ackermann et al. 2012) depending on the event class and event type⁶, to predict the number of observed counts. This convolution ensures that the analysis accurately accounts for the LAT's sensitivity, angular resolution, energy resolution, and diffuse emission models.

Once the data products (event data and spacecraft data files), the latest background all-sky model (Galactic and isotropic diffuse emission models), and compatible IRFs are obtained, the data is prepared for analysis. Fermi-LAT data preparation involves selecting and filtering the downloaded data by defining the region of interest (RoI) and the event class & type, applying energy⁷ and zenith angle cuts,

⁴LAT Data Server: <https://fermi.gsfc.nasa.gov/cgi-bin/ssc/LAT/LATDataQuery.cgi>

⁵LAT Background Models: <https://fermi.gsfc.nasa.gov/ssc/data/access/lat/BackgroundModels.html>

⁶IRF Selection at https://fermi.gsfc.nasa.gov/ssc/data/analysis/documentation/Cicerone/Cicerone_LAT_IRFs/IRF_overview.html

⁷Between 100 MeV to 300 GeV is recommended to ensure optimal effective area of LAT.

and ensuring only good time intervals (GTI) are used. These selection and filtering are done using the two fermitools: `gtselect` and `gtmktime`.

The RoI is a circular region centered on the source of interest, including all relevant sources contributing to the gamma-ray emission around the source. Since PSF is energy dependent, the size of RoI should be defined considering the energy range for the analysis. For an accurate analysis, the RoI must be large enough to include events several degrees from the center, often including nearby sources in an additional ring around the RoI. One may refer to this larger region around RoI as the ‘Source Region’. To optimize the computing time, the typical size for a RoI is between 10° and 20° , allowing modeling only this part of the sky instead of the whole sky. The event class and type for the events within the selected RoI are then defined based on the overall likelihood of being true gamma-ray photons versus background events, photon conversion location (front, back, or both), their PSF signature, and energy dispersion value. The Earth’s limb produces gamma rays when high-energy cosmic rays collide with atmospheric nuclei, generating pions that decay into gamma rays. A zenith cut is applied to avoid contamination from these secondary gamma rays. The threshold zenith angle value or the zenith cut is typically at 90° , implying that the events with a zenith angle greater than this value are excluded. To ensure only “good” quality events, the GTI is updated based on the information embedded in the spacecraft file. For example, the periods during no observation or when the spacecraft passes through SAA are excluded from the GTI.

Once the data files are prepared, it’s helpful to pre-calculate how long the LAT observed each part of the sky at different angles, i.e., livetime⁸, to speed up expo-

⁸Livetime cubes are additive and need to be created only once per time range, as they are independent of source models.

sure calculations during Likelihood analysis ⁹. This livetime is then applied to RoI to create an exposure map. As the name suggests, the exposure map¹⁰ gives the total exposure (area multiplied by time) for each position in the sky contribution to emission in the RoI.

Finally, the data is fitted to the model to obtain the best estimates of the observed events' source properties, such as location, flux, spectrum, and light curve. This analysis is fundamentally based on the Maximum Likelihood method. Given a specific input model, the likelihood \mathcal{L} represents the probability of obtaining the measured data. In the case of Fermi-LAT analysis, the input model includes the distribution of all the gamma-ray sources in the sky within the RoI and the source region, with their spectra, intensity, and background information.

For the Fermi-LAT data, the counts are distributed in many bins, and the observed number of counts in each bin is assumed to follow a Poisson distribution. Therefore, using Cash statistics (Cash 1979), we have,

$$\mathcal{L} = \prod_{i=1}^N p_i = \prod_{i=1}^N \frac{m_i^{n_i} \times e^{-m_i}}{n_i!} = e^{-N_{exp}} \prod_{i=1}^N \frac{m_i^{n_i}}{n_i!} \quad (2.1)$$

where p_i is the probability of detecting n_i counts if m_i is the expected number of counts in the i -th bin and n_i is the observed number of counts. N_{exp} is the total number of expected counts predicted by the model.

In unbinned analysis, the bin sizes are made infinitesimally small, resulting in each bin containing zero or one count. The likelihood is then:

$$\mathcal{L} = e^{-N_{exp}} \prod_{i=1}^N m_i \quad (2.2)$$

⁹Details of the Likelihood analysis are discussed later in the same section.

¹⁰Detailed description on livetime and exposure computation at https://fermi.gsfc.nasa.gov/ssc/data/analysis/documentation/Cicerone/Cicerone_Data_Exploration/livetime_and_exposure.html

Since computation time and memory usage increase with the number of photons and the type of sources, the preferred analysis for most of the Fermi-LAT analysis is binned likelihood. However, unbinned likelihood analysis can be adopted for sources with lower photon rates¹¹. Binning is performed in two dimensions: energy and position (pixel).

One needs to maximize the probability of the data for that model to find the best set of parameters for a given model and/or the best model. This best fit, known as the maximum likelihood estimate, is obtained by maximizing the likelihood function given by Equation 2.1 (Mattox et al. 1996) using optimization methods¹². Now, to determine the significance of detection, a Test-Significance (TS) value is calculated as follows,

$$TS = -2\ln\left(\frac{\mathcal{L}_{max,0}}{\mathcal{L}_{max}}\right) \quad (2.3)$$

where $\mathcal{L}_{max,0}$ is the maximum likelihood for the null hypothesis, i.e., no source present, and \mathcal{L}_{max} is the maximum likelihood with the source included. The TS value measures the source's significance, indicating how likely or unlikely it is that the detection occurred by chance. The higher the TS value, the higher the significance of detection. To the first order approximation, $\sigma \approx \sqrt{TS}$ (Wilks 1938)¹³.

Once a best-fit model has been found, we have the TS values, as well as source positions and spectral parameters, such as the slope of the spectrum and the individual source flux. A spectrum with a variable number of spectral bins can then be generated. Additionally, a light curve can be computed for the entire specified time range by dividing it into bins of fixed or adaptive sizes. For each bin, the analysis starts anew to find the best-fit model. Choosing the right bin size is crucial for

¹¹Fermipy performs binned likelihood analysis.

¹²Fermitools have five optimizers: DRMNGB, DRMNFB, NEWMINUIT, MINUIT, and LBFGS.

¹³If Wilks' Theorem holds, integrating the chi-squared distribution from the observed TS value to infinity gives the probability that the source is just a random fluctuation. The significance is approximately \sqrt{TS} σ , so a TS of 25 corresponds to a 5σ significance.

achieving significant detection in each bin.

We use the following three physically-motivated spectral models for the fitting¹⁴.

1. Power-Law :

$$\frac{dN(E)}{dE} = N_o \left(\frac{E}{E_o} \right)^{-\Gamma} \quad (2.4)$$

where the normalization N_o and γ -ray photon index Γ are considered as free parameters. The scale value E_o is fixed at its catalog value.

This model is motivated by emission processes such as synchrotron radiation and inverse Compton scattering, where particles accelerated in magnetic fields or shock fronts emit radiation over a wide range of energy. This model is a good approximation for many astrophysical sources.

2. Log-Parabola:

$$\frac{dN(E)}{dE} = N_o \left(\frac{E}{E_o} \right)^{-\alpha - \beta \ln(E/E_o)} \quad (2.5)$$

where N_o , α and β are the free parameters.

This model is particularly useful for sources where the spectral energy distribution shows a gradual curvature. The log parabola can account for the energy-dependent acceleration mechanisms in these environments, providing a better fit than a simple power law.

3. Power-Law with exponential cutoff:

$$\frac{dN(E)}{dE} = N_o \left(\frac{E}{E_o} \right)^{-\Gamma} \exp \left(\frac{-E}{E_c} \right) \quad (2.6)$$

where N_o , Γ and E_c are the free parameters.

This model is motivated by physical processes where there is a maximum en-

¹⁴A longer list of available spectral models can be found on the website: https://fermi.gsfc.nasa.gov/ssc/data/analysis/scitools/source_models.html#spectralModels

ergy that particles can attain. The exponential cutoff represents the energy loss mechanisms or limited acceleration efficiency, causing a rapid decline in flux at high energies.

The significance of spectral curvature in the gamma-ray spectrum of the source is also statistically determined using the TS value. The spectral curvature is significant if $TS_{curve} > 16$ (corresponding to 4σ ; Mattox et al. 1996), where $TS_{curve} = 2(\log \mathcal{M} - \log \mathcal{L})$. \mathcal{M} is the maximum likelihood of models with curvature (i.e., log-parabola and power-law with exponential cutoff), and \mathcal{L} is the maximum likelihood of models with no curvature (i.e., power-law).

2.2 X-Ray Emission

X-ray emission in the Universe originates from hot and extreme environments such as stellar coronae, supernova remnants, and AGN jets. Consequently, like gamma rays, X-rays reveal the most energetic and extreme environments in the Universe. In 1949, rockets carrying radiation detectors briefly ascended above the Earth's atmosphere, which absorbs X-rays (see Figure 2.2), and detected X-rays from the Sun, providing the first hint of cosmic X-rays. It took over a decade for significantly improved detectors to discover X-rays from sources beyond our solar system. The first imaging X-ray telescope was developed in 1963 by Riccardo Giacconi's team at American Science and Engineering in Cambridge, MA. Launched on a small-sounding rocket, it produced basic images of hot spots in the Sun's upper atmosphere. In the Scorpius constellation, it detected the first X-ray source beyond the Sun, Scorpius X-1. Since the 1970s, dedicated X-ray satellites like Uhuru, EXOSAT, Ginga, RXTE, ROSAT, ASCA, BeppoSAX, and Suzaku¹⁵ have sig-

¹⁵European X-Ray Observatory Satellite (EXOSAT), Rossi X-ray Timing Explorer (RXTE), ROentgenSATellite (ROSAT), Advanced Satellite for Cosmology and Astrophysics (ASCA), BeppoSAX was named in honor of the Italian physicist

nificantly advanced the field of X-ray astronomy. Launched in the 1990s, NASA's flagship mission, Chandra X-ray Observatory, and European Space Agency's X-ray Multi-Mirror Mission, XMM-Newton, continue to provide valuable data for researchers. Neil Gehrels Swift Observatory (Swift), launched on November 20, 2004, was specifically designed to study Gamma-Ray Bursts (GRBs) across multiple wavelengths, including gamma-ray, X-ray, ultraviolet, and optical bands. It has successfully provided data for other X-ray sources, including AGNs, ever since. The thesis majorly uses Swift data and a few XMM-Newton observations, which are discussed in Sections 2.2.3 and 2.2.4. The Nuclear Spectroscopic Telescope Array (NuSTAR), launched on March 21, 2012, is currently the only active X-ray observatory focusing on hard X-ray emissions from astrophysical sources in the 3-79 keV energy range, following the earlier launch of the International Gamma-Ray Astrophysics Laboratory (INTEGRAL) in 2002.

2.2.1 Instrumentation

X-rays are so energetic and have small wavelengths that they pass through most materials, including traditional mirrors used for visible light. That is to say, if we shoot X-rays at a mirror, they will mostly pass through instead of reflecting. However, they can reflect if we hit X-rays at a shallow angle. This is called 'grazing incidence'. Therefore, An X-ray telescope should have suitable mirror surfaces oriented parallel to the incoming X-rays. To maximize the number of captured X-ray photons, X-ray telescopes use cylindrical mirrors nested inside one another, looking like an onion, increasing the effective area. Hans Wolter, in 1952, proposed three designs for building telescopes using these cylindrical nested mirrors: Wolter type I, II, and III (Figure 2.3). Due to its simplest mechanical configuration,

Giuseppe "Beppo" Occhialini, with SAX for Satellite per Astronomia a raggi X or Satellite for X-ray Astronomy

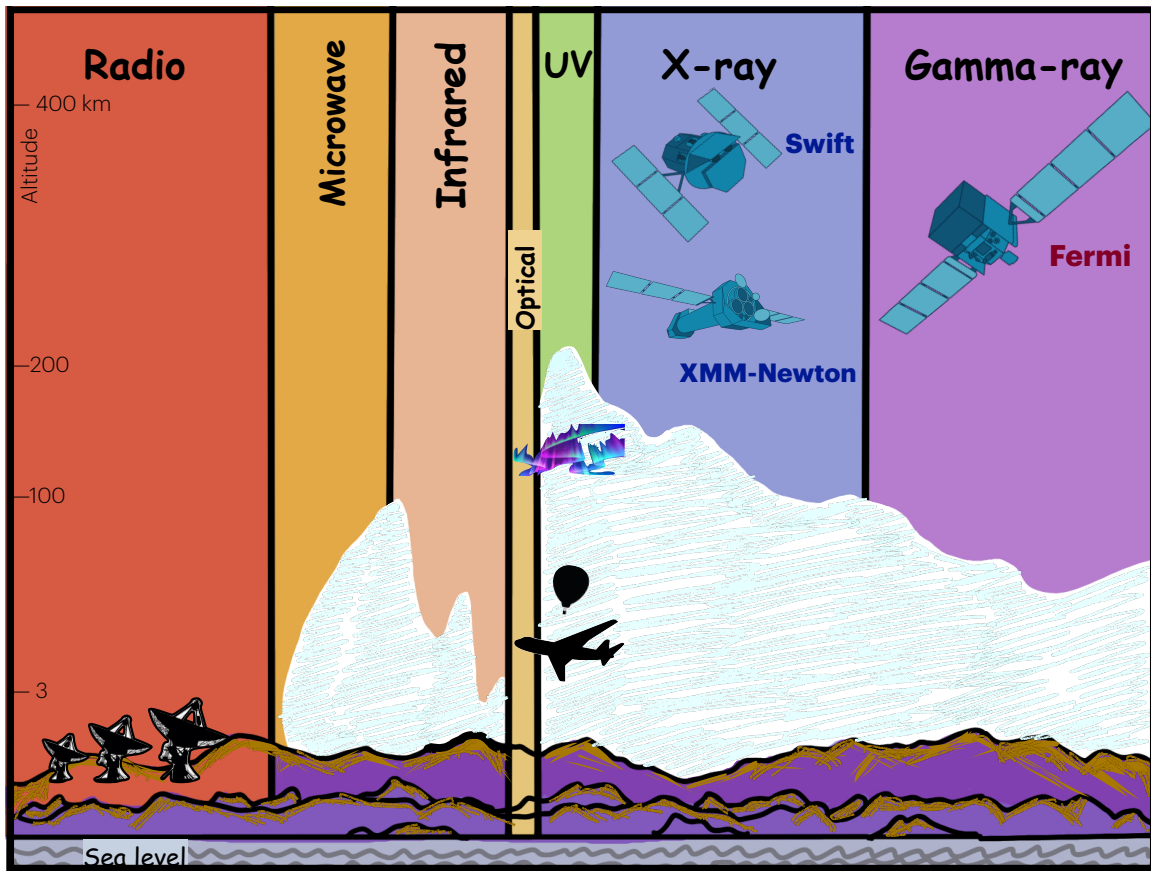


Figure 2.2: The image illustrates the absorption of different electromagnetic wavelengths by Earth's atmosphere, emphasizing the need for diverse observational platforms.

most telescopes have Type I design.

Once the light is collected, it is directed to a detector, which can help determine the direction, time of arrival, brightness, and intensity of the photons based on the type of detector. There are several types of X-ray detectors and different modes of operation. In photon-counting mode, certain types of X-ray detectors can record individual X-ray photons and gradually accumulate data to create an accurate image of the source. Therefore, X-ray detectors are designed to interact with X-rays since they pass through most materials. These detectors convert the energy from X-rays into measurable forms such as electric charge, light, or heat. Two common interactions within these detectors are photoelectric absorption, where X-rays are fully absorbed and eject electrons from atoms, and Compton

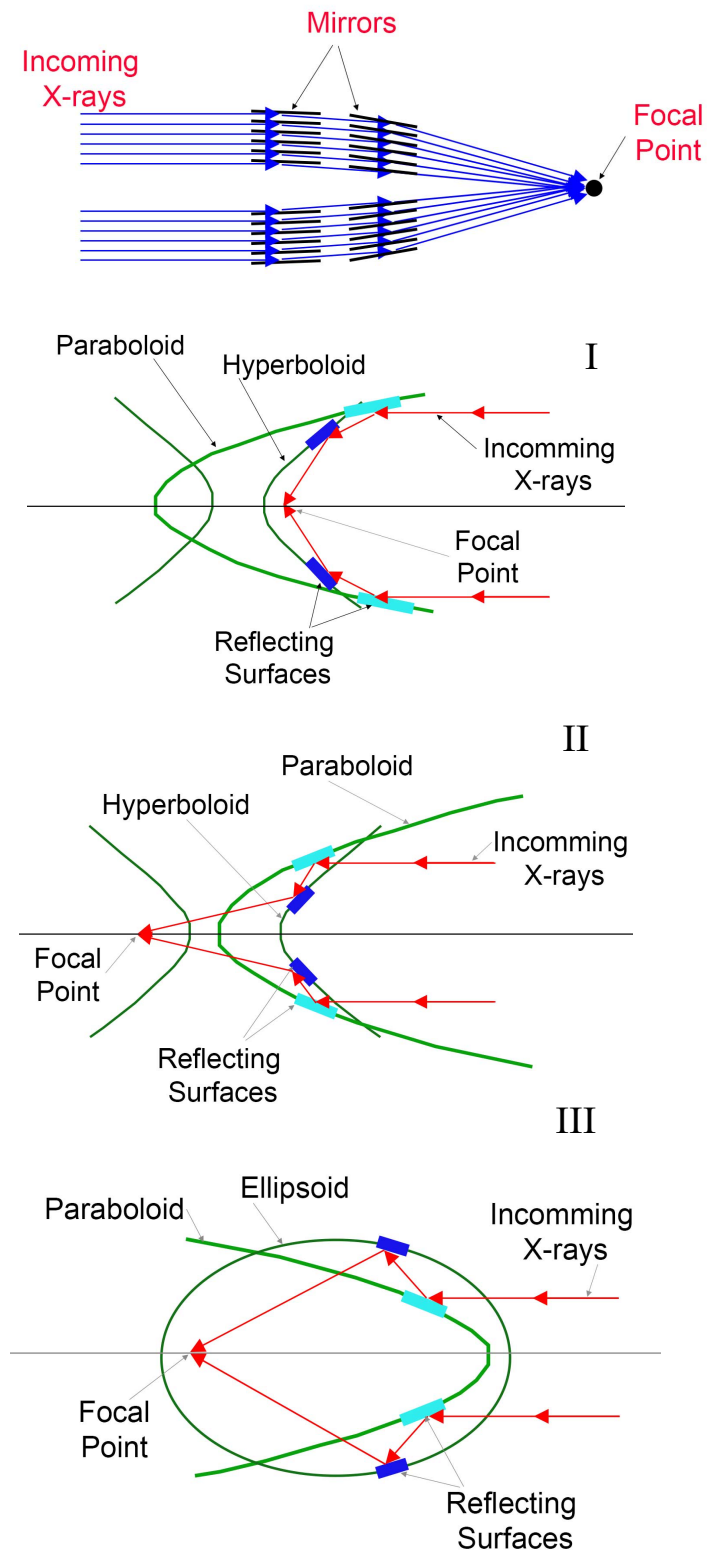


Figure 2.3: Wolter mirrors' design taken from NASA's Imagine the Universe! The top panel shows the design of a cut-away X-ray telescope with nested cylindrical mirrors.

scattering, where X-rays transfer part of their energy to an electron and scatter at a lower energy. Key types of X-ray detectors include proportional counters, which measure electric charges created by ionized gas in response to X-ray exposure, and Charge-Coupled Devices (CCDs), which capture displaced electrons in a semiconductor material when struck by X-rays. Scintillators measure the light produced when photons interact with the atoms and are absorbed, resulting in the emission of photons (in the form of light). Calorimeters directly measure the heat produced in the material when the incoming X-ray is absorbed. The type of detector used in an observatory depends on the science goals. For instance, observatories like Chandra, Swift, and XMM-Newton use CCD detectors, while Fermi and INTEGRAL employ scintillators.

Since their invention, Charge-Coupled Devices (CCDs) have become a widely used technology, enabling us to capture images in devices like our cell phones by converting photons to electrons. In a CCD, a grid of pixels, each acting as a miniature solid-state detector, captures incoming photons. The main component of a CCD is a semiconductor with a depletion zone created through a p-n junction, typically using silicon as the base material. The material's conductivity is greatly increased by doping the silicon with foreign atoms, such as boron for the p-junction and phosphorus for the n-junction. This p-n junction forms a depletion zone where electric charges generated by photons through the photoelectric effect accumulate in potential wells. The charges in each pixel are sequentially transferred to a readout register, converted into voltage, amplified, and digitized, forming an image where each pixel's intensity reflects the count of X-ray photons it detected. Continuous readout of the CCD is necessary to avoid charge overflow and the loss of data from multiple photons striking a single pixel simultaneously, a problem known as pile-up. Instruments like those on the XMM-Newton and Swift

observatories mitigate pile-up by varying the illuminated number of pixels and speeding up readout times, allowing them to handle brighter X-ray sources efficiently.

Calibration with the satellite clock allows us to find the time of the event, which is when the charge is transferred to the readout register. The Pulse Height Amplitude (PHA) is the output from the Analog-to-Digital (A/D) converter that quantifies this charge, allowing for the measurement of the energy of the detected X-ray photon. The position of the detected X-ray event is determined by identifying the pixel or the centroid of the cluster of pixels that registered the event. To convert the pixel position to a position in the sky, the size of CCD, focal length of a telescope, pointing of the telescope, and relative telescope/detector position need to be known. This kind of information is generally stored in attitude files and observation metadata files.

2.2.2 Analysis

SPECTRUM: The intrinsic flux of the source is calculated from the counts recorded by the detector using the fundamental equation of the X-ray observational astronomy, given by

$$N(E) = F(E) \cdot A(E) \cdot \Delta T \quad (2.7)$$

In this equation, $N(E)$ represents the number of counts detected by the instrument at energy E during the exposure time. $F(E)$ is the intrinsic flux of the source at energy E , which quantifies the number of photons per unit area per unit time per unit energy. $A(E)$ is the effective area of the telescope at energy E , reflecting the sensitivity of the detector. ΔT is the exposure time, the duration over which the counts are recorded.

However, the instrument measures the instrumental (or detector) energy, which

may not exactly match the true energy of the incident photon. To accurately reconstruct the original energy spectrum of the source, it is essential to consider the response matrix (RMF). The RMF describes how the instrument responds to and broadens a monochromatic input spectrum, accounting for discrepancies between the detected and actual photon energy. That gives us,

$$N(E') = \Delta T \int_0^{\infty} R(E, E') \cdot F(E) \cdot A(E) dE \quad (2.8)$$

where $R(E, E')$ is the detector response matrix, which describes how photons of true energy E are detected and redistributed across the detector's energy channels E' ^{16, 17}. However, X-ray detectors have a finite number of energy channels (say n_{ch}), each corresponding to a specific energy range (bin). Therefore, the number of photons detected in the i -th energy channel during the observation,

$$N(E'_i) = \Delta T \sum_{i=0}^{n_{ch}} R(E, E'_i) \cdot F(E) \cdot A(E) dE \quad (2.9)$$

$N(E'_i)$ includes both the source and the background counts. Background subtraction is done by measuring the background count rate $B(E'_i)$ and subtracting it from the total count rate $N(E'_i)$ to obtain the source count rate,

$$S(E'_i) = N(E'_i) - B(E'_i) \quad (2.10)$$

with the uncertainty calculated assuming Poisson statistics.

¹⁶The RMF provides the probability of detecting a photon with energy E in a particular energy channel of the instrument.

¹⁷While $R(E, E')$ is often sufficient, spatial dependencies are incorporated in the form $R(E, E', r, r')$ in cases where precise spatial measurements are critical.

Now, to obtain the intrinsic flux (or spectrum) from Equations 2.9 and 2.10¹⁸, one must deconvolve the observed spectrum with the response matrix and effective area. Direct deconvolution of Equation 2.9 is often impractical, which is done through forward model fitting. This process involves assuming a theoretical model for the source spectrum, characterized by a number of adjustable parameters. This model is then convolved with the response matrix of the detector to simulate how the detector would record the model spectrum. Using *XSPEC*¹⁹ adjusts the model parameters to ensure that the convolved spectrum matches the observed data. This iterative fitting process allows the intrinsic flux to be derived using the best-fit model parameters²⁰.

Depending on the photon counts, different statistical methods are utilized for the fitting process described above. The best-fit model is the set of model parameters that maximize the likelihood of the observed data, given the model and its parameters θ . To make math easier and provide suitable machinery and algorithms, the sign of the function to maximize is flipped. For better numerical accuracy, we use logarithms. Thus, the standard practice is to minimize the fit statistic given by

¹⁸Equation 2.9 can be rewritten using Equation 2.10 as

$$N(E'_i) = \Delta T \sum_{i=0}^{n_{ch}} R(E, E'_i) \cdot F_s(E) \cdot A(E) dE + B(E'_i)$$

where F_s is the intrinsic source flux.

¹⁹An X-ray mission-independent spectral fitting package that is part of High-Energy Astronomy Software (HEASoft)

²⁰The power-law spectra in X-ray astronomy are typically fitted in units like photons per keV rather than energy per unit frequency. X-ray power-law fits generally follow the form

$$P_E \text{ (photons s}^{-1} \text{ keV}^{-1}) \propto E^{-\Gamma} \propto \nu^{-\Gamma},$$

since photons per second closely match the measured quantity, which is counts per second. In units of energy flux (or luminosity), we have

$$F_\nu \propto P_E \text{ (photons s}^{-1} \text{ keV}^{-1}) \times h\nu \text{ (ergs/photon)} \propto \nu^{-\Gamma+1} \propto \nu^{-\alpha}.$$

To distinguish clearly between these two spectral indices, α is usually referred to as the 'energy index' and $\Gamma = \alpha + 1$ is called the 'photon index'.

$$-2 \times \log P(\theta) \quad (2.11)$$

A spectrum with many counts per bin will result in a Gaussian distribution of counts in each bin. We use a chi-squared (χ^2) minimization approach in this case. That is,

$$c_i \sim \text{Gaussian}(\lambda_i, \sigma_i) \quad (2.12)$$

where c_i is the count in bin i sampled from a Gaussian distribution with mean λ_i and standard deviation σ_i . The likelihood is then given by,

$$P_{\text{Gaussian}}(c_i, \lambda_i) = \frac{1}{\sqrt{2\pi}\sigma} \exp \left\{ -\frac{1}{2} \left(\frac{c_i - \lambda_i}{\sigma_i} \right)^2 \right\} \quad (2.13)$$

and following Equation 2.11, the minimization statistic is called chi-squared statistic (Gorenstein et al. 1968), given by

$$\chi^2 = \sum_i \left(\frac{c_i - \lambda_i}{\sigma_i} \right)^2 \quad (2.14)$$

While χ^2 can be used for high-count data (more than 20-30 counts), it can lead to biased estimates in low-count scenarios (Figure 2.4)²¹. If we assume that the counts in each bin follow Poisson distribution, Cash statistics (Cash 1979) is used:

$$c_i \sim \text{Poisson}(\lambda_i) \quad (2.15)$$

The Poisson probability is given by,

$$P_{\text{Poisson}}(c_i, \lambda_i) = \frac{\lambda_i^{c_i} \times e^{-\lambda_i}}{c_i!} \quad (2.16)$$

²¹One is further referred to Buchner & Boorman (2023) for a nice review on X-ray spectral analysis.

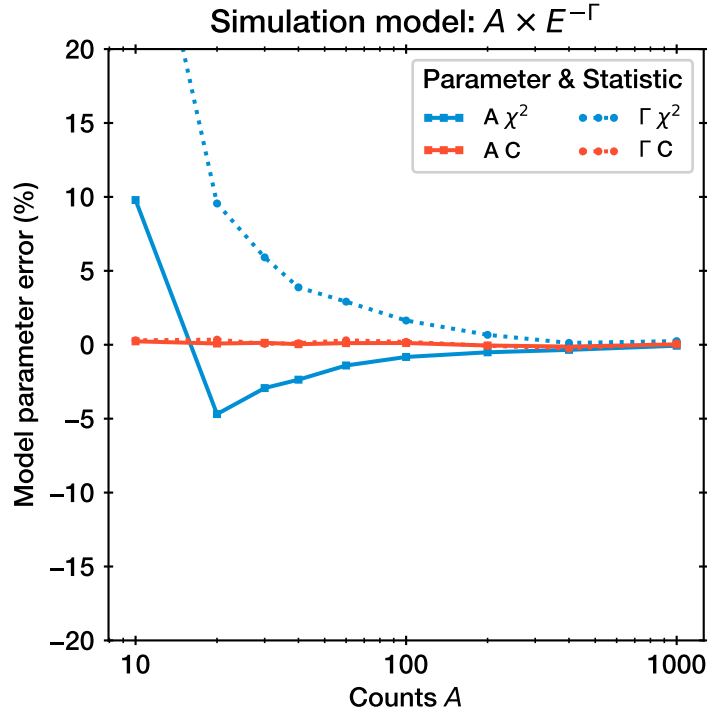


Figure 2.4: A plot of the difference between the estimated model parameters and their true values versus the number of counts. C-Stat (red) can be used to fit models to Poisson-distributed count data at all count levels, as it provides unbiased parameter estimates. In contrast, the χ^2 statistic (blue), suitable for high counts (over 20), leads to biased estimates with fewer counts, underestimating amplitude and overestimating the power-law index. The figure is taken from Buchner & Boorman (2023).

and the statistic follow,

$$CStat = \sum_i c_i \log \lambda_i - \lambda_i \quad (2.17)$$

LIGHT CURVE: Light curves show how the brightness of an astrophysical object changes over time. Unlike spectra, they don't need convolution-deconvolution with the detector's response matrix because they directly measure the total brightness in each time interval.

DATA EXTRACTION: The observed and archived data for most X-ray missions can be obtained from the High Energy Astrophysics Science Archive Research Center (HEASARC)²². Each observation's data folder contains standard files (in FITS for-

²²HEASARC Archive: <https://heasarc.gsfc.nasa.gov/cgi-bin/W3Browse/w3browse.pl>

mat), such as the response matrix file (.rmf), though naming conventions may vary between different X-ray missions. These files include an event list that records all photon events, with their arrival times, positions, and energies. Additionally, details about the telescope's orientation, pointing direction, and other metadata are stored in attitude, orbit, and housekeeping files. The effective area, or $A(E)$ in Equation 2.9, is stored in an Auxiliary (or Ancillary) Response File (.arf). Additionally, a calibration file is required, which includes clock corrections, a gain file with information on energy calibration, a quantum efficiency file detailing the efficiency of the detector in converting incoming photons into measurable signals, and other necessary calibration data²³.

High-level science products such as spectra, light curves, and sky images were created using the above files. I give an overview of creating these data products only for imaging telescopes. The first step is to create a set of cleaned files by applying appropriate filters. The timing filter is applied to include only times during which the instruments perform as expected. That is to say, the period of passage through South Atlantic Anomaly (SAA) or high background activity is excluded. This timing filter provides us with the Good Time Intervals (GTI) files. Further, the known 'bad pixels' are excluded. These bad pixels may be either dead pixels, which have a broad depletion region and therefore no signal, or hot pixels, which have a narrow depletion region and thus show a continuous signal.

To extract a spectrum (and light curve), a sky image of the field of view is created with SAODs9²⁴ using the cleaned image file corresponding to cleaned events (obtained after filtering). This produces a 2D histogram of counts on the sky. Once the image is created, the next step is identifying and extracting the source pho-

²³Calibration files are available at the HEASARC's CALibration DataBase (CALDB): https://heasarc.gsfc.nasa.gov/docs/heasarc/caldb/caldb_intro.html

²⁴SAODs9 is an open-source image display and visualization tool for astronomical data.

tons by selecting a suitable shape and size region. Generally, a circle or annulus is chosen for the region. For an annulus, the outer radius accounts for the background photons. A circular region of appropriate size is selected to extract the background photons for a circular source region. Once the source and background regions are defined, photon count files are produced for these regions, which are the source and background PHA files, respectively. In addition, RMF and ARF files are generated for these regions to ensure accurate data interpretation. Following the spectral analysis method described above, the spectrum is then obtained.

For the work in this thesis, data from mainly two X-ray missions are used, namely, the Neil Gehrels Swift Telescope and XMM-Newton. An overview of these two missions is given in the following subsections.

2.2.3 Neil Gehrels Swift Telescope

The Neil Gehrels Swift Telescope or Swift Telescope (Gehrels et al. 2004), launched in 2004, is a multi-wavelength space observatory primarily designed to detect gamma-ray bursts (GRBs). However, its versatile instruments have already proven exceptionally useful for observing AGNs and other X-ray persistent and transient sources (for examples, see Gupta et al. 2012, Schimoia et al. 2015, Rani et al. 2017, MAGIC Collaboration et al. 2020b, Acciari et al. 2021, Rani et al. 2022, Gulati et al. 2023, Evans et al. 2023). The following three instruments onboard the Swift satellite work together to provide simultaneous observation for a source in optical, ultraviolet, and soft and hard X-ray bands (Figure 2.5).

a) Burst Alert Telescope (BAT)

The BAT (top-right; Figure 3.2.2; Barthelmy et al. 2005) is a highly sensitive instrument in the 15-150 keV energy range. The BAT utilizes a coded aperture mask

consisting of 52,000 lead tiles, each 5 mm in size, arranged randomly. This mask is 1 meter above a detector plane, which includes 32,768 Cadmium Zinc Telluride (CdZnTe) hard X-ray detector tiles, each measuring 4 mm. It has a large field-of-view (FOV) covering a large portion of the sky, with over one steradian fully coded and three steradians partially coded (the whole sky is about 12.6 steradians)²⁵. The BAT is primarily designed to provide rapid alerts for GRBs. By default, it operates in a survey mode and continuously scans the sky, allowing it to monitor other high-energy sources like X-ray binaries and blazars. Upon detecting a GRB, it switches to burst mode to calculate its position and prompt follow-up multiwavelength observations with other instruments onboard Swift. More details can be found in [Barthelmy et al. 2005](#).

b) X-Ray Telescope (XRT)

Unlike BAT, XRT (bottom-left; [Figure 2.5](#); [Burrows et al. 2005](#)) is a narrow-field instrument with a 23.6×23.6 arcmin FOV. It is a focusing X-ray telescope that uses twelve concentric mirrors in the Wolter type-I arrangement (discussed above) to focus X-rays onto CCDs with 600×600 pixels. It works in the energy range of 0.2 - 10 keV with an effective area of 110 cm^2 and 18 arcsec resolution (half-power diameter). The main goal of XRT is to provide rapid, accurate positions, good-resolution spectroscopy, and high-time resolution light curves. There are three major operations (readout/processing) modes available in XRT: Imaging, Photon-Counting (PC), and Windowed-Timing (WT) mode. When the spacecraft locks onto a new target, the XRT begins operation in Imaging Mode, which produces an integrated image by measuring the total energy deposited per pixel. This mode does not per-

²⁵The terms "fully coded" and "partially coded" describe how the coded-aperture mask of the BAT affects its field of view and sensitivity to X-ray sources. Simply put, the fully coded region provides higher sensitivity and more accurate localization, while the partially coded region covers a larger area with reduced sensitivity and precision.

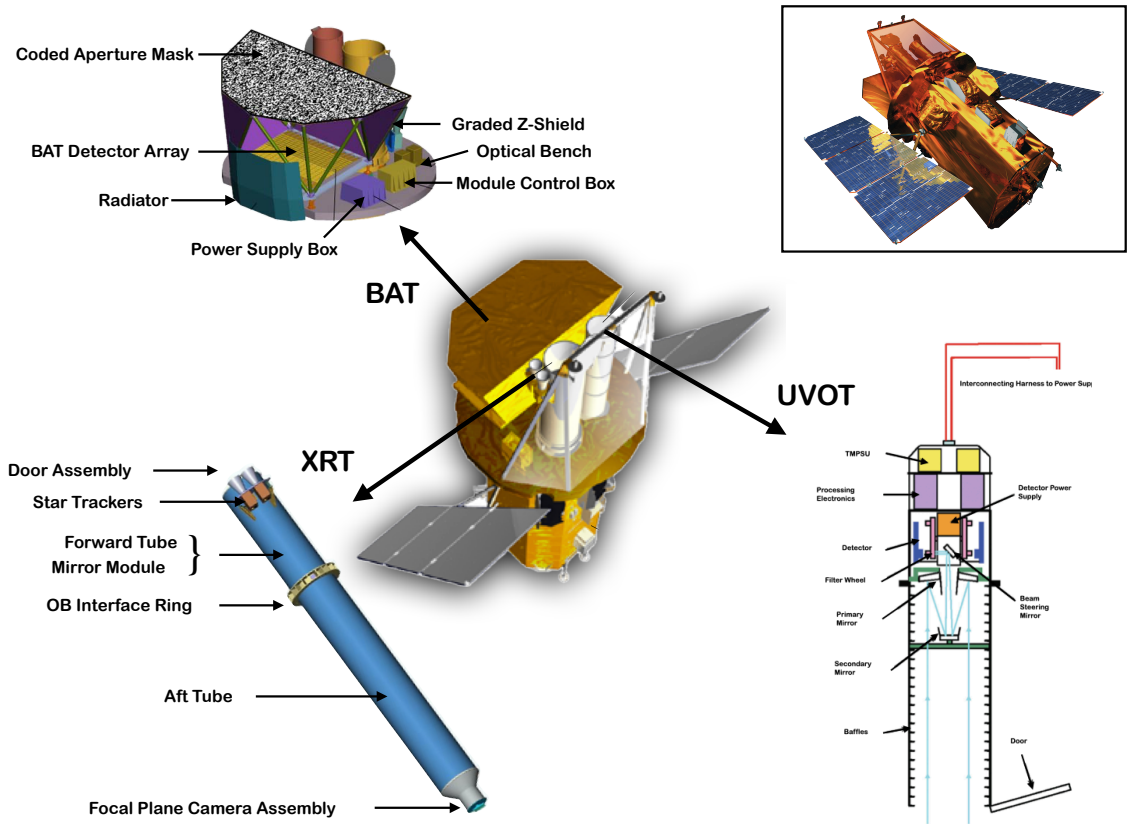


Figure 2.5: The inset shows a schematic image of the Swift satellite. The top view in the middle clearly depicts the three onboard instruments, BAT, XRT, and UVOT, with their components highlighted.

mit spectroscopy. It is used to quickly determine the location of bright sources, such as GRBs, with an accuracy better than 2.5 arcseconds within 5 seconds. PC and WT modes allow the observation of both bright and faint sources. The PC mode is used for observing faint X-ray sources (generally with fluxes below one mCrab) to avoid pile-up²⁶. It retains complete imaging and spectroscopic resolution, capturing each photon's arrival time, energy, and position. The time resolution in PC mode is 2.5 seconds. It uses a standard CCD readout sequence, which reads the entire CCD every 2.5 seconds. For brighter sources, Swift switches automatically to WT mode. It achieves a high timing resolution of 2.2 milliseconds, crucial for

²⁶Pile-up occurs when multiple photons hit the same region of the CCD within a single frame transfer period, causing them to be detected as a single event (of higher energy). It becomes significant for sources with fluxes exceeding 0.5 counts per second (ct s^{-1}).

studying rapid variability in X-ray sources. To achieve high time resolution, the WT mode sacrifices two-dimensional position information. Instead, it provides one-dimensional imaging, clocking columns continuously, resulting in a trailed image along each column.

We utilize the XRT observations in this thesis. Swift observations are particularly valuable for studying AGN due to their versatile instrumentation, rapid response capabilities, and ability to perform long-term monitoring. Once the dataset for observation with Swift is obtained, cleaned event files are produced using the FTOOLS²⁷ `xrtpipeline`. This script has three stages: standard calibration, screening, and filtering. In the first stage, the data is calibrated using the latest calibration files (available in CALDB²⁸). In the second stage, a list of screened events is extracted using the science data and corresponding filter files. It utilizes GTIs (as discussed in Section 2.2.2) by setting conditions on the instrument's attitude and orbit, housekeeping parameters, and bad pixels. This ensures that only data from reliable observation periods are considered for further processing. In the final stage, the previously determined GTIs are applied to the event files to produce the cleaned products, including clean event files. The clean image file created using `xselect` (which is run in `xrtpipeline`) is then used with `ds9` to extract source and background regions as discussed in Section 2.2.2. The region selection is straightforward for the PC mode, as discussed, since it's a 2D²⁹ image. The image is 1D³⁰ in WT mode, and essential care must be taken while selecting the source and background regions. Region selection must, of course, not extend beyond the WT image where there is no data. Further, source and background regions must have the same radius if circular regions are used in WT mode. If different radius

²⁷FTOOLS is a package of HEASoft that allows manipulation of files in FITS format.

²⁸Swift CALDB: <https://heasarc.gsfc.nasa.gov/docs/heasarc/caldb/swift/>

²⁹2D: 2-dimensional

³⁰1D: 1-dimensional

are taken, the BACKSCAL keyword while extracting spectrum and light curve using XSELECT must be set to $2r_s$ and $2r_b$ ³¹ for source and background, respectively to reflect the 1D extent. Generally, the 2D image is collapsed in WT mode into a 1D strip 200 pixels wide, and 100 pixels is the center. If an annular region is selected, centered on the source position, the radii for the background region must be symmetrically placed around 100 pixels³². The edges in WT mode are bad pixels; therefore, BACKSCAL is set to $r_2 - r_1 - 1$ if the edges are enclosed within the annulus to exclude it. Otherwise, BACKSCAL is set to $r_2 - r_1$ ³³. With the source and background regions, the source and background spectra (PHA files; Section 2.2.2) and light curve are then extracted using the tool `xselect`. The tool `xrtmkarf` is used to produce the ARF file. The corresponding RMF file can be found in the output of `xrtmkarf` or determined using `ftool quzCIF` for any given observation. Finally, to improve the signal-to-noise (SN) ratio, `grppha` is used to group the data such that a minimum number of counts per bin is achieved for the relevant statistics (discussed in Section 2.2.2). The grouped spectra are then used in XSPEC to obtain the best-fit model parameters.

c) Ultra-Violet and Optical Telescope (UVOT)

UVOT (bottom-right; Figure 2.5) is the essential instrument onboard Swift that makes the observatory multiwavelength. It is a diffraction-limited 30 cm Ritchey-Chrétien reflector with a 12 arcsecond aperture. It provides simultaneous ultra-violet and optical coverage in the 170-650 nm range across a $17' \times 17'$ FOV. The UVOT features an $f/2.0$ primary mirror that is re-imaged to $f/13$ by the secondary mirror, resulting in 0.502 arcseconds pixels. Equipped with two micro-channel

³¹ r_s and r_b are the radius of the circular regions selected for source and background, respectively.

³²See for more details: <https://www.swift.ac.uk/analysis/xrt/backscal.php>

³³ r_2 and r_1 are outer and inner radii of the annulus, respectively.

plates intensified CCD detectors, the UVOT operates as a photon counting device, capable of detecting very faint objects down to magnitude 22.3 for a 17-minute exposure. There are three primary data modes in UVOT, namely, Image, Event, and Image&Event. Image mode records only the event’s position and creates a 2D sky image. In Event mode, the event’s position and time are captured. Image&Event mode records both data types from the same exposure, allowing different window sizes, locations, and binning. The UVOT data is obtained similarly to XRT data from the HEASARC archive. The data files are provided in different sub-folders within the UVOT data folder for other modes. For the works in this thesis, we do not perform spectrometry and only obtain the intrinsic flux values of the source in each band recorded in Image mode. Therefore, I will review the steps to get the fluxes in the following section.

| Filter | Wavelength [Å] | Zero point | Error | Conversion factor [$\times 10^{-16}$] | Error [$\times 10^{-18}$] |
|--------|-------------------|------------|-------|--|--------------------------------|
| V | 5468 | 17.89 | 0.01 | 2.614 | 0.87 |
| B | 4392 | 19.11 | 0.02 | 1.472 | 0.57 |
| U | 3465 | 18.34 | 0.02 | 1.63 | 2.5 |
| W1 | 2600 | 17.44 | 0.03 | 4.0 | 9.7 |
| M2 | 2246 | 16.85 | 0.03 | 8.5 | 5.6 |
| W2 | 1928 | 17.38 | 0.03 | 6.2 | 14.0 |

Table 2.1: The six filters of UVOT, along with their wavelengths, zero points and associated errors, and conversion factors and their associated errors, are listed.

Note: The central wavelength of the wavelength band of each filter is listed.

There are six UVOT filters: V, B, U, W1, M2, and W2 (Table 2.1). Similar to the X-ray analysis, source, and background regions are selected from the images using `ds9`. The aperture for photometry calibration is 5 arcseconds, so the source region must be the same size. If a different size for the region is used, aperture correction using the `apercorr` keyword (in the `ftool uvotsource`) is required. A background region of larger size, typically 10 arcseconds, can be selected in any source-free area on the image. The source magnitude is extracted with `uvotsource` using the region

files selected. This magnitude is corrected for Galactic reddening³⁴ to obtain the intrinsic magnitude of the source. We use the Python implementation `extinction`³⁵ using the dust extinction function given by [Fitzpatrick \(1999a\)](#). The value of R_V is fixed at 3.1. The intrinsic values obtained are converted to count rates in each filter using the zero point³⁶ correction values ([Breeveld et al. 2011a](#)) provided in [Table 2.1](#). The count rates are then converted to fluxes (in the units of $\text{erg s}^{-1}\text{cm}^{-2}\text{\AA}^{-1}$) using conversion factors (listed in [Table 2.1](#); [Poole et al. 2008](#)). The respective errors are calculated using standard error propagation. The relevant formulae and error calculation are given in [Appendix B](#). The `uvotimsum` tool is used to sum images from different observations if multiple exposures are taken, and similar steps from `uvotsource` are followed to obtain the fluxes for summed images.

2.2.4 XMM-Newton

XMM-Newton (XMM: X-ray Multi-Mirror; [Jansen et al. 2001](#)), launched on December 10, 1999, is a major European Space Agency (ESA) satellite telescope designed to observe X-ray emissions from very hot and energetic astrophysical sources such as active galactic nuclei, active black holes, neutron stars, and supernova remnants. There are three scientific instruments onboard XMM-Newton: European Photon Imaging Camera (EPIC), Reflection Grating Spectrometer (RGS), and Optical Monitor (OM). These instruments allow simultaneous observations in X-ray and optical/UV bands. The X-ray telescopes have a Wolter type-I arrangement with 58 nested mirrors coated with gold. The three X-ray telescopes are co-aligned, ob-

³⁴ R_V and A_V follows extinction law as

$$R_V = \frac{A_V}{E(B - V)}$$

. Here, A_V is the extinction in the V band, and R_V is the total-to-selective extinction ratio. The A_V value is taken from the NED database for the line-of-sight of each source.

³⁵<https://extinction.readthedocs.io/en/latest/index.html>

³⁶Zero point is defined as the magnitude of an object that produces one count per second on the detector.

serving an energy range of 0.15 - 15 keV. Another distinct telescope onboard: a 30cm optical/UV telescope with a CCD detector that uses a microchannel plate pre-amplifier at its focal plane (Mason et al. 2001). The data reduction process for XMM-Newton observations is done using separate software, and the steps are discussed in Section 2.2.4.

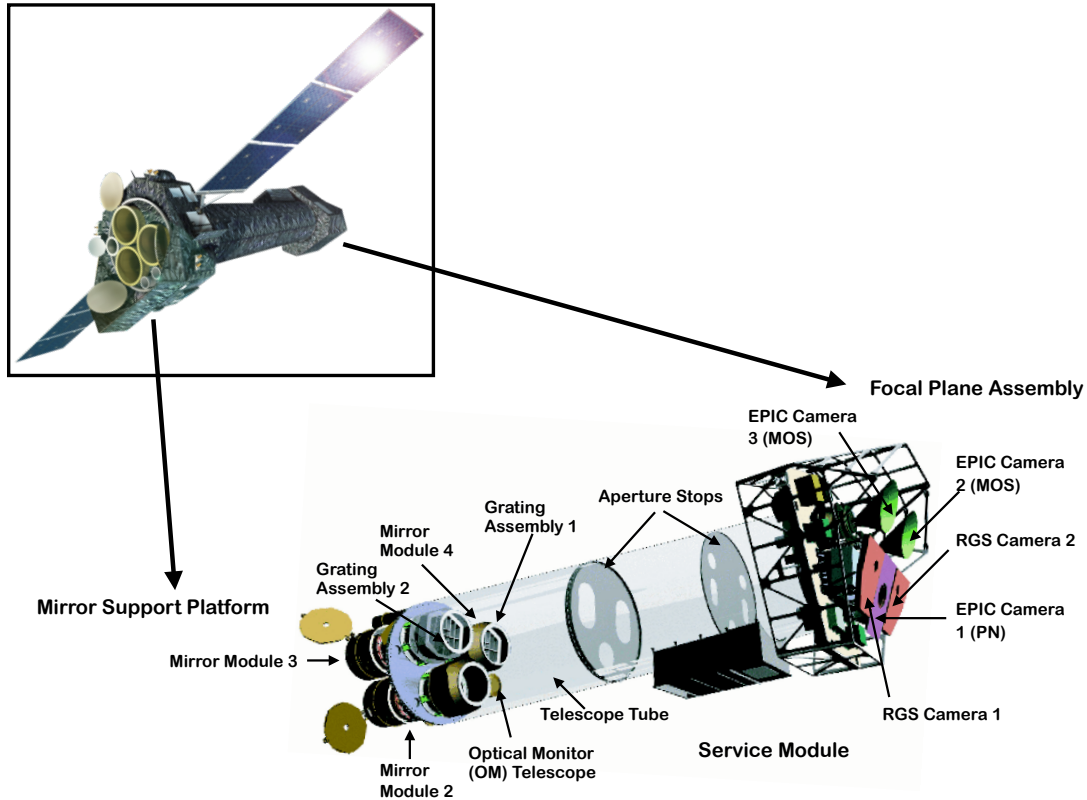


Figure 2.6: Inset shows an artistic impression of the XMM-Newton. The sketch below the inset shows the different instruments and components onboard XMM-Newton.

a) European Photon Imaging Camera (EPIC)

EPIC consists of three X-ray detectors or cameras: two MOS (Turner et al. 2001) and one pn (Strüder et al. 2001). MOS cameras are Metal Oxide Semi-conductor (MOS) CCD arrays with RGS gratings in the light path. At the focal point of the third telescope is a pn CCD called the pn camera, where the incoming light reaches with-

out obstruction, unlike EPIC-MOS(s). All three cameras allow good imaging in the 30 arcmin's FOV of the X-ray telescopes. They offer moderate spectral resolution ($E/\Delta E \sim 20-50$) and angular resolution of 6 arcseconds (FWHM). EPIC cameras allow several operating modes: full (and extended full) frames, partial windows, and timing. The first mode is allowed only by pn. All CCD pixels are read out, covering the entire field of view in this mode. In Partial Window mode, the central CCD of the MOS cameras reads only a portion of the chip, with small window mode capturing 100×100 pixels and large window mode capturing 300×300 pixels. Similarly, the pn camera operates in large and small window modes for data acquisition in Partial Window mode. The pn camera, in large window mode, reads half of the area of all 12 CCDs, while in small window mode, it uses only part of CCD4³⁷. The Timing mode, used by the MOS and PN cameras, collapses data along the column axis for high-speed readout. The pn camera offers a burst mode for very high time resolution with a 3% duty cycle.³⁸ More information, including timing resolutions in these modes, is provided in XMM's Users Handbook³⁹. An additional part of EPIC is the EPIC Radiation Monitor (ERM). The ERM detects solar flares and radiation belts and supplies particle environment information to ensure the correct operation of EPIC cameras.

EPIC cameras (MOS and pn) record X-ray events, which are categorized based on the pattern of pixel activation on the CCD when an X-ray photon is detected. Patterns are defined by how many pixels are affected and in what arrangement. Single events (PATTERN = 0) occur when an incoming X-ray photon activates only

³⁷CCD4 according to numbering conventions of Science Analysis Software (SAS) or CCD0 in the first quadrant. Details at <https://www.cosmos.esa.int/web/xmm-newton/boundaries-pn>

³⁸Duty cycle refers to the fraction of time the camera is actively collecting data compared to the total cycle time. A 3% duty cycle means it collects data for only 3% of the total observation time, allowing very high time resolution during the short periods when the camera is active.

³⁹XMM's Users' Handbook, Section 3.3.2: https://xmm-tools.cosmos.esa.int/external/xmm_user_support/documentation/uhb/epicmode.html

one pixel. These events offer the highest energy resolution and are less affected by noise and charge spreading, making them ideal for precise measurements. Double events (PATTERN = 1-4 for EPIC-pn and PATTERN = 1-12 for EPIC-MOS) involve the activation of two adjacent pixels by a single photon.

b) Reflection Grating Spectrometer (RGS)

The RGS is best suited for high spectral resolution X-ray spectroscopy, with resolving power ($\Delta E/E \sim 150$ to 800) over the energy range of 0.33 to 2.5 keV and an effective area peaking around 0.83 keV at approximately 150 cm². This configuration allows RGS to analyze a rich spectrum of X-ray emission lines, which is ideal for investigating the physical conditions and chemical compositions of cosmic sources. Two RGS units, each consisting of linear arrays of nine MOS CCD chips, are positioned along the Reflection Grating Assemblies (RGAs) dispersion direction. These RGAs are mounted in the light path of the telescopes and intercept about half of the focused light.

c) Optical Monitor (OM)

The Optical/UV Monitor Telescope (XMM-OM or OM) is mounted alongside the X-ray mirror modules on the mirror support platform (see Figure 2.6). It covers wavelengths from 170 nm to 650 nm within the central 17 × 17 arcmin's square region of the X-ray FOV. It enables simultaneous ultraviolet/optical observations with X-ray for XMM targets. The telescope is a modified 30 cm Ritchey-Chrétien design with a focal ratio of $f/12.7$ and a focal length of about 3.8 m. Light enters the 2 m long telescope tube, is reflected by the primary and secondary mirrors, and then directed by a 45° inclined mirror to one of two detectors. There are 11 apertures containing broadband filters (U, B, V, UVW1, UVM2, UVW2), a white filter,

a magnifier, and two gratings (UV and optical) for various observational purposes (Table 2.2).

Table 2.2: The seven filters of OM, along with their wavelengths, width, and zero points, are listed. Note: The central wavelength of the wavelength band of each filter is listed.

| Filter | Effective wavelength [nm] | Width ^a [nm] | Zeropoint [magnitudes] | AB zero point [magnitudes] |
|--------------------|------------------------------|----------------------------|---------------------------|-------------------------------|
| V | 543 | 70 | 17.9633 | 17.9230 |
| B ^b | 450 | 105 | 19.2661 | 19.0809 |
| U | 344 | 84 | 18.2593 | 19.1890 |
| UVW1 | 291 | 83 | 17.2038 | 18.5662 |
| UVM2 | 231 | 48 | 15.7724 | 17.4120 |
| UVW2 | 212 | 50 | 14.8667 | 16.5719 |
| White ^c | 406 | 347 | 20.2555 | 20.6900 |

^a Width is the Full Width at Half Maximum (FWHM).

^b The B filter's effective wavelength is set to 450 nm to avoid the core of the Balmer line H γ .

^c Values for the White filter are based on simulations.

Data Reduction for XMM-Newton

While the steps for data reduction remain the same (discussed in Section 2.2.2), XMM-Newton data is reduced using the Science Analysis Software (SAS)⁴⁰ unlike HEASoft used for several other X-ray missions including Swift. Observation data can be obtained from HEASARC's archive. One may also obtain the data from the XMM-Newton Science Archive (XSA) as it is XMM-specific and provides detailed information, such as the observation mode of each instrument. Therefore, we use XSA to retrieve the desired data. The calibration files for XMM data are called the Current Calibration Files (CCF) and are stored in the ccf folder⁴¹. The calibrated event files are then obtained using `emproc` and `epproc` for EPIC-MOS and

⁴⁰SAS: <https://www.cosmos.esa.int/web/xmm-newton/download-and-install-sas>

⁴¹A CCF index file is required, which is built using the command `cifbuild`. It lists all the CCFs relevant to the observations of interest. More details at <https://www.cosmos.esa.int/web/xmm-newton/current-calibration-files>

EPIC-pn, respectively. These calibrated event files are then filtered for high flaring background using `evselect` and `tabgtigen`. Event selection is then performed, where for EPIC-MOS cameras, single to quadruple events (`PATTERN = 0-12`) in the energy range of 0.3-12 keV are selected, while for the EPIC-pn camera, both single and double events (`PATTERN 0-4`) in the energy range of 0.15-15 keV are chosen. Pileup correction is applied as needed. RMF is generated using the SAS task `rmfgen`, and ARF is created with the `arfgen` task. The cleaned and calibrated data are then used to extract light curves and spectra with tasks `evselect`. The spectra are grouped and rebinned to improve the SN ratio. Finally, we perform spectral fitting with `XSPEC` to derive best-fit model parameters with suitable statistics (as discussed in Section 2.2.2).

2.3 Multiwavelength Modeling

Once we obtain the flux measurements across different energy bands, we can construct a comprehensive Spectral Energy Distribution (SED). Modeling the SED of jetted AGNs, such as blazars, radio galaxies, and quasars, offers insights into their physical characteristics, including particle acceleration mechanisms, the composition and structure of the jets, and how these jets interact with their surrounding environments.

We consider a simple ‘blob-in-jet’ framework, where a homogeneous and spherical emission region (called a *blob*) with radius R is considered (white; left panel Figure 2.7). This region penetrates the tangled magnetic field with uniform strength B within the jet at a certain distance from the SMBH. The emission region contains a relativistic plasma consisting of electrons, positrons, and/or protons, which interact with the magnetic field to produce radiation through processes like synchrotron emission and inverse Compton scattering. The blob moves with a bulk

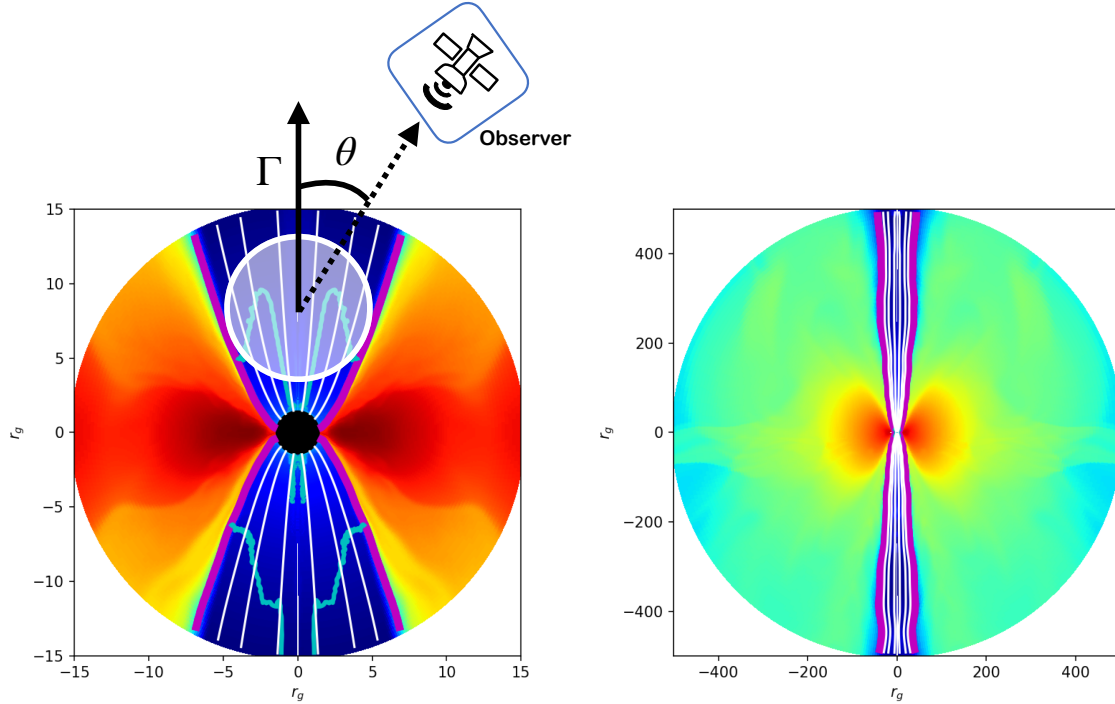


Figure 2.7: A 2D GRMHD simulation for radiatively inefficient accretion flow is presented: (left) small FOV focusing on detailed structures near the black hole, and (right) large FOV capturing the extended jet structure. Image is taken from Pu et al. 2022. Relativistic jets are launched from the funnel region of black holes via the BZ mechanism. The color represents density distribution shown on a logarithmic scale, where blue indicates low density and red indicates high density. A schematic (not-to-scale) one-zone model is white in the left panel.

Lorentz factor Γ along the jet's direction, with a velocity close to the speed of light, c , and a Doppler factor δ . The angle θ is between the jet's motion and the observer's line of sight. The simplicity of this model makes it versatile to provide a common framework for comparing a wide range of AGNs, including blazars, radio galaxies, and quasars, and understanding their emission properties.

Particles are assumed to be accelerated in a shock region located ahead of the blob in the direction of motion⁴²(Kirk et al. 1998). This acceleration occurs through a process such as Diffusive Shock Acceleration (DSA), an example of a first-order Fermi (Fermi I) process. This mechanism typically results in single power-law distributions of particle energies, as detailed by seminal studies such as Blandford &

⁴²Acceleration and emission regions are different.

Eichler 1987 and Jones & Ellison 1991.

The accelerated particle distribution is injected into the plasma blob, represented by $Q = Q(E, t)$, which is the number of particles injected per unit time, per unit energy interval.

The particles confined in the blob may cool down via different cooling mechanisms such as synchrotron emission, inverse Compton process, and adiabatic process. To calculate the particle spectrum $N = N(E, t)$ at any instant t , we solve the time-dependent kinetic equation for particles (leptons, in our case), called the Fokker-Planck equation:

$$\frac{\partial N(E, t)}{\partial t} = Q(E, t) - \frac{\partial(bN)}{\partial E} - \frac{N(E, t)}{t_{esc}} \quad (2.18)$$

where t_{esc} is the timescale over which the leptons escape from the emission region, $b = b(E, t)$ is the energy loss rate, and $Q(E, t) \sim Q(E)$ is considered to be independent of time (Ginzburg & Syrovatskii 1964). I discuss the escape time and energy loss rate in our work below.⁴³

The particles are assumed to escape advectively from the emission region, and thus,

$$t_{esc} = \eta \frac{R}{c} \quad (2.19)$$

where R/c is the light-crossing time from the emission region of radius R , c is the speed of light, and $\eta > 1$ is the escape timescale parameter. The parameter η quantifies the diffusive nature of particle transport in a plasmoid, accounting for scattering that prolongs particle paths and escape times. The value of η reflects

⁴³NOTE: When comparing the luminosities of spectra of parent particles using different codes, note that in GAMERA, we typically quote the injected luminosity at time 0. In contrast, the luminosities of injected population quoted for modeling using steady-state codes corresponds to the luminosity when the equilibrium is achieved. The correct way for comparison thus is to compare the luminosity of injected particles at the time when steady-state is achieved using GAMERA with the latter.

how scattering within a plasmoid extends the paths of particles, thus increasing their escape time compared to direct, straight-line travel (see, e.g., Böttcher et al. 2013 and Gao et al. 2017).

The energy loss rate, $b(E, t) = -dE/dt$, includes cooling due to radiative losses like synchrotron and inverse Compton process, considering the Klein-Nishina effects (Blumenthal & Gould 1970). This can be written as,

$$b(E, t) = \left(-\frac{dE}{dt}\right)_{\text{total}} = \left(-\frac{dE}{dt}\right)_{\text{Synch}} + \left(-\frac{dE}{dt}\right)_{\text{IC}} \quad (2.20)$$

$$= \frac{4}{3}\sigma_{TC}(U_B + U_{\text{rad}})\gamma^2 \quad (2.21)$$

where U_B and U_{rad} are the energy densities of the magnetic field and the photon field, respectively, and $\gamma = E/(mc^2)$ is the Lorentz factor of the particle with rest mass m .

In the thesis work, we have considered the leptonic SSC model (see Chapter 1); therefore, $\gamma = E/(m_e c^2)$ where m_e is the rest mass of electrons (equal to that of positrons). Additionally, the Fokker-Planck equation, given by Equation 2.18 is solved using publicly available time-dependent code GAMERA⁴⁴(Hahn 2015).

The code subsequently calculates the synchrotron and inverse-Compton emission, which is Doppler boosted by a factor of δ^4 in the observer's frame due to relativistic beaming. $\delta = [\Gamma(1 - \beta \cos\theta)]^{-1}$ is the Doppler factor, Γ is the bulk Lorentz factor, β is the intrinsic speed of the emitting plasma and θ is the viewing angle of the jet with respect to the line of sight of the observer (Figure 2.7).

The input parameters of the model include parameters describing the injected particle distribution and parameters describing the emission region radius, R , and magnetic field strength, B . The simulated spectral energy distributions are subsequently fitted to the data points by adjusting the model's free parameters to find

⁴⁴GAMERA: http://libgamera.github.io/GAMERA/docs/main_page.html

the best-fit model parameters.

Finally, the total required jet power to produce the observed emission within our model is calculated as

$$P_{tot} = \pi R^2 \Gamma_b^2 c (U'_e + U'_B + U'_p) \quad (2.22)$$

where U'_e , U'_B and U'_p are the energy densities of electrons, magnetic field, and protons in the comoving frame of jet respectively. These are defined as follows:

$$U'_e = \frac{1}{V} \times \int_{E_{min}}^{E_{max}} Q(E) E dE \quad (2.23)$$

$$U'_B = \frac{B^2}{8\pi} \quad (2.24)$$

and

$$U'_p = n_p m_p c^2 \quad (2.25)$$

where V is the volume of the emission region, m_p is the mass of the proton, and n_p is the number density of protons, which is equal to the number density of electrons n_e , assuming the jet contains equal numbers of electrons and protons to maintain charge neutrality.

Each photon of starlight is a tiny piece of a grand puzzle, helping us to unravel the mysteries of the cosmos and our place within it.

Henrietta Swan Leavitt

3

Gamma ray emission from kilo-parsec jets

In this chapter, we have studied four gamma-ray LLAGNs: NGC 315, NGC 4261, NGC 1275, and NGC 4486. Electrons are assumed to be accelerated to relativistic energies in sub-parsec scale jets, which radiate by synchrotron and synchrotron self-Compton emission covering radio to gamma-ray energies. This model can fit most of the multi-wavelength data points of the four sources. However, the gamma-ray data points from NGC 315 and NGC 4261 can be well-fitted only up to 1.6 GeV and 0.6 GeV, respectively, in this model. Assuming gamma rays are also produced in kilo-parsec scale

jets (detected in radio and X-rays) of these sources from inverse Compton scattering of starlight photons by ultra-relativistic electrons, it is possible to fit the gamma-ray data at higher energies.

This chapter is based on the paper published in the *Astrophysical Journal* titled **“Broadband Modeling of Low Luminosity Active Galactic Nuclei Detected in Gamma Rays”** by Tomar et al. (2021).

The gamma-ray detection by Fermi-LAT from non-blazar AGNs shows that these are different and potentially very interesting classes of gamma-ray emitters (Rieger 2017). This provides an alternative approach to studying high-energy emission processes compared to blazars, where the emission is strongly Doppler boosted, which favors their detection.

3.1 Sample

Ho et al. (1995, 1997a) conducted the Palomar spectroscopic survey, focusing on northern galaxies (declination $> -30^\circ$) with an apparent blue magnitude $B_T < 12.5$. This comprehensive survey, using high-quality, moderate-resolution, long-slit optical spectra, aimed to study nearby galaxies’ demographics and physical properties, particularly low-luminosity active galactic nuclei (LLAGNs; Ho 2008). The survey found that over 40% of nearby galaxies contain LLAGNs, revealing that low-luminosity nuclear activity is more common than previously thought. The emission-line spectra from these galaxies showed a wide range of properties, indicating diverse physical conditions in their nuclei. The survey found that LLAGNs are associated with elliptical and lenticular galaxies, unlike spiral galaxies, which typically host more luminous AGNs. By showing that LLAGNs are very common, the survey suggested that low-level nuclear activity is a typical stage in the life of many galaxies. The smooth transition between AGNs and LINERs implies that

many galaxies might experience different levels of nuclear activity at different times. Therefore, it is crucial to study LLAGNs using observations across multiple wavelengths.

de Menezes et al. (2020) selected 197 AGNs (declination $> 0^\circ$) from 486 bright northern galaxies in the Palomar spectroscopic survey to look for gamma-ray emission. Only four sources were detected in gamma rays with a significance above 5σ ($TS > 25$). These four sources are NGC 315, NGC 1275, NGC 4261, and NGC 4486 (M87). All four sources are misaligned FRI radio galaxies with kiloparsec-scale radio jets.

In this work, we study these four source to find the possible origin of their gamma-ray emission. These four are briefly discussed below.

3.1.1 NGC 315

NGC 315 is a nearby elliptical galaxy located at a redshift of 0.01648 (Trager et al. 2000). It hosts a Fanaroff-Riley type 1 (FR I) radio source with two-sided asymmetric well-resolved radio jets at arcsec and milliarcsec resolutions shown both with Very Long Baseline Interferometry (VLBI) and Very Large Array (VLA) observations (Venturi et al. 1993, Cotton et al. 1999). The high spatial resolution of Chandra imaging allowed the detection of X-ray emission from the main jet (Worrall et al. 2003) inclined at an angle $38^\circ \pm 2^\circ$ to our line of sight (Canvin et al. 2005). The Hubble Space Telescope (HST) image shows a clear circum-nuclear dusty disk with a 2.5 arcsec diameter in its center (Verdoes Kleijn et al. 1999). It has been classified as an LLAGN by Ho et al. (1997b) through the detection of a broad H_α line. Its LLAGN nature was later confirmed by Gu et al. (2007), who obtained the bolometric luminosity of $L_{bol} \sim 1.9 \times 10^{43}$ ergs s^{-1} corresponding to an extremely low Eddington ratio of 4.9×10^{-4} .

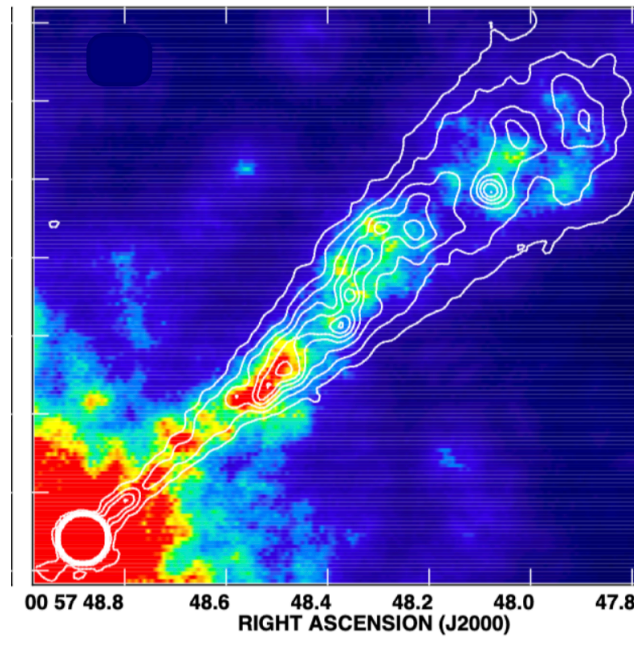


Figure 3.1: NGC 315 image taken from Worrall et al. (2007a) showing large-scale radio and X-ray jet. Black contours represent a 5 GHz VLA radio map. The X-ray 0.8–5 keV image taken by Chandra.

The radio and X-ray emission from the kiloparsec jets of NGC 315 have been observed owing to the good resolution of VLA and Chandra. The radio flux of 74 and 50 mJy are observed at 5 GHz for the kiloparsec jet (in the region between 3.2 arcsecs and 16.2 arcsecs from the nucleus) of NGC 315 (Worrall et al. 2007a; shown in Figure 3.1).

Located at a distance of 65.8 Mpc (Nagar et al. 2005), this LLAGN is one of the four low accreting galaxies from the Palomar survey (Ho et al. 1995, 1997b) to be detected at γ -ray energies at above 5σ significance by Fermi (de Menezes et al. 2020). It is detected with a statistical significance of $\sim 9\sigma$ in the energy range 0.1–300 GeV over an observation of 10.25 years ranging from August 4th, 2008, to November 15th, 2018. The measured differential spectrum is well defined by a power-law with photon index $\Gamma = 2.32 \pm 0.11$ with an average flux of $3.38 (\pm 0.43) \times 10^{-12}$ ergs cm^{-2} s^{-1} .

3.1.2 NGC 4261

NGC 4261 is an elliptical galaxy located at a redshift of 0.00738 (Cappellari et al. 2011), with a nucleus classified as a type 2 Low-ionization nuclear emission-line region (LINER) based on high-quality optical spectra by Ho et al. (1997b). It is located at a distance of 35.1 Mpc (Nagar et al. 2005) with a SMBH of mass $4.9 (\pm 0.1) \times 10^8 M_{\odot}$ (Ferrarese et al. 1996) at the center. It hosts a low-power FR I radio source with twin jets (Birkinshaw & Davies 1985b) oriented at angle $63^{\circ} \pm 3^{\circ}$ with respect to the line of sight of the observer (Piner et al. 2001). In addition, a 300 pc-scale nuclear disk of gas and dust was imaged by HST (Jaffe et al. 1993, Ferrarese et al. 1996) lying orthogonal to the radio jets.

The presence of X-ray jet has been detected in the inner few kiloparsec-scale of the radio jets by ROSAT observations (Figure 3.2; Gliozzi et al. 2003, Zezas et al. 2005, Worrall et al. 2010). Zezas et al. (2005) also showed a substantial absorbing column in X-rays. After absorption and bolometric corrections, the luminosity is only 2.0×10^{-5} of the Eddington luminosity, implying a low accretion rate.

NGC 4261 was detected in γ -rays by Fermi with a significance of $\sim 6.8\sigma$ over a period of 10.25 years (de Menezes et al. 2020). A power-law with photon index 2.15 ± 0.16 and an average flux of $2.15 (\pm 0.42) \times 10^{-12}$ ergs cm^{-2} s^{-1} explains the measured spectral energy distribution in the energy range 0.1-300 GeV.

3.1.3 NGC 1275

NGC 1275 is one of the nearest radio galaxies at a redshift of $z = 0.0176$ (Young et al. 1995). It is located at a distance of 70.1 Mpc (Nagar et al. 2005) and is elliptical in shape. It is a radio-loud AGN with a relatively low Eddington ratio of 3×10^{-4} (Sikora et al. 2007), classifying it as a low luminosity AGN. It is identified as Seyfert

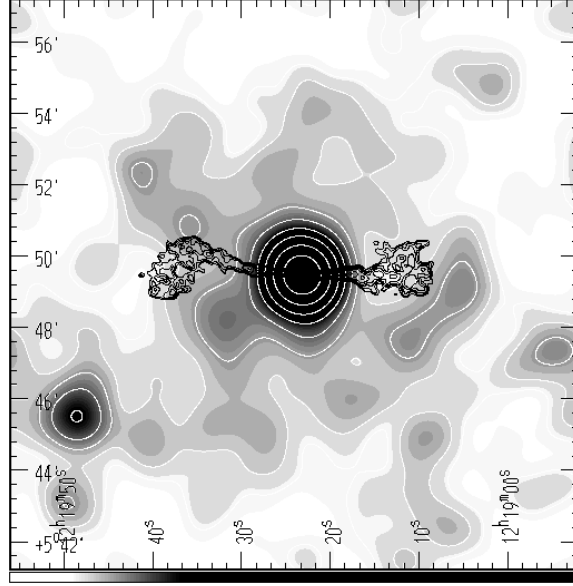


Figure 3.2: NGC 4261 image taken from Worrall et al. (2010) showing large-scale radio and X-ray jet. Black contours represent 5 GHz VLA radio map (Birkinshaw & Davies 1985a). The X-ray 0.4-2 keV image taken by ROSAT is smoothed with a Gaussian of $\sigma = 30$ arcsec.

1.5 due to the presence of a weak broad emission line based on $H\alpha$ study (Ho et al. 1997b). The detailed studies of the AGN with VLBI and VLA established the presence of an exceptionally bright radio source (3C 84) with asymmetrical jets at both parsec and kilo-parsec scales (Walker et al. 2000, Vermeulen et al. 1994, Asada et al. 2006), suggesting an FR I morphology. These studies reveal a jet angle of 30° - 60° with our line of sight (Walker et al. 1994, Asada et al. 2006). Recently, Fujita & Nagai (2017) suggested the viewing angle of the jet with respect to the line of sight to be $65^\circ \pm 15^\circ$ based on the increased radio activity detected by Nagai et al. (2010).

NGC 1275 is one of the brightest radio galaxies detected at the high energy (HE; >100 MeV) and very high energy (VHE; >100 GeV) γ -rays (Abdo et al. 2009a, Aleksić et al. 2012). The average flux and the photon index measured by Fermi from 2008 August 4 to 2016 November 15 are $F_{>100\text{MeV}} = 3.34(\pm 0.03) \times 10^{-7}$ ph cm $^{-2}$ s $^{-1}$ and 1.93 ± 0.01 , respectively (Tanada et al. 2018b). At VHE, *MAGIC* measured the average γ -ray flux above 100 GeV to be $1.3 (\pm 0.2) \times 10^{-11}$ ph cm $^{-2}$ s $^{-1}$. The corresponding differential spectrum in 70-500 GeV was estimated with a power-law of

photon index 4.1 ± 0.7 (Aleksić et al. 2012). This spectral break from HE to VHE was later confirmed by several studies like Fukazawa et al. (2015), Tanada et al. (2018b). NGC 1275 has also been observed at VHE by other imaging atmospheric Cherenkov telescopes like *HEGRA*, *Whipple*, *VERITAS* (Mukherjee & VERITAS Collaboration 2017) and *TACTIC* (Ghosal et al. 2020).

3.1.4 NGC 4486 (M87)

M87 is a giant elliptical galaxy located in the Virgo cluster at a redshift, $z = 0.00428$ (Cappellari et al. 2011). It is located at a distance of 16.8 Mpc (Nagar et al. 2005), with a SMBH of mass $6.5 \times 10^9 M_{\odot}$ at its center powering it (Event Horizon Telescope Collaboration et al. 2019). Despite hosting such an SMBH, its bolometric luminosity is only of the order of 10^{42} ergs s^{-1} , which is six orders of magnitude lower than the Eddington luminosity (Reynolds et al. 1996), placing this in the class of LLAGNs. It is commonly classified as a FR I radio galaxy. The narrow emission lines also suggest it is a type 2 LINER. The relativistic jet, first detected by H. Curtis (Curtis 1918) in optical, is misaligned with respect to the line of sight with an angle between 15° and 30° (Biretta et al. 1999; Acciari et al. 2009; Walker et al. 2018). Due to its proximity, the jet is well-imaged at radio through X-ray frequencies. This relativistic outflow extends up to kilo-parsec scales (Marshall et al. 2002) and its radiative output is believed to dominate the spectral energy distribution of the AGN core (Abdo et al. 2009b, Nemmen et al. 2014b, de Jong et al. 2015, Prieto et al. 2016, Fraija & Marinelli 2016). A recent polarised image of the SMBH of M87 indicates the presence of a strong magnetic field at the event horizon, which can launch powerful jets (The Event Horizon Collaboration 2021).

M87 is the first extra-galactic object to be detected at VHE by *HEGRA* (Aharonian et al. 2003). Since then, it has been detected at γ -ray frequencies by *H.E.S.S.*,

VERITAS, *MAGIC*, and Fermi (Aharonian et al. 2006, Albert et al. 2008, Acciari et al. 2008, Abdo et al. 2009b).

3.2 Multiwavelength Observations and Data Analysis

We have constructed the multiwavelength SED of our sample by compiling radio-to-UV data from earlier works on these sources. We have analyzed the X-ray data recorded by *XMM-Newton* in 2017 from NGC 4486, *XMM-Newton* data taken in 2019 and *Swift* data from 2017 to 2018 for NGC 315, and compiled the archival X-ray data available on NGC 4261 and NGC 1275 (see details in Section 3.2.2). In addition, we analyzed 12 years of Fermi data collected over the period of 2008 to 2020. Due to low spatial resolution in the gamma-ray energy band, the distinction between the emission from the sub-parsec scale and kilo-parsec scale jet cannot be made. The radio and X-ray data points of the extended jets of NGC 315 and NGC 4261 were obtained from observations by Very Large Array (VLA) and Chandra (and ROSAT) observatories, respectively, owing to their high spatial resolution (Worrall et al. 2007a, Worrall et al. 2010). The results obtained for the maximum likelihood analysis of Fermi-LAT data are summarized in Table ?? for different spectral models. The 12-year averaged spectrum, and the best fit of each spectral model are shown in Figure 3.7. Data from NED ¹ has also been taken for an overall reference SED.

3.2.1 Radio to UV

The radio-to-UV data for this work has been compiled from previous observations. The details of the observations and reductions can be found in the references given in Figure 3.3, 3.4, 3.5, and 3.6.

¹<https://ned.ipac.caltech.edu/>

Whenever available, radio data has been taken from NRAO² Very Large Array (VLA), NRAO Very Large Baseline Array (VLBA) and Very Large Baseline Interferometry (VLBI). The high resolution of these radio telescopes allowed scientists to isolate radio emissions from the AGN from other sources. In the optical band, data points from *Hubble Space Telescope (HST)* have been obtained, if available.

a) NGC 315

NGC 315 has been observed in radio band by several studies using VLA, VLBA, and VLBI (Capetti et al. 2005, Nagar et al. 2005, Kovalev et al. 2005, Venturi et al. 1993). As part of a polarimetric survey, it was simultaneously observed at 86 GHz and 229 GHz in August 2010 using the XPOL polarimeter on the IRAM 30m radio telescope (Agudo et al. 2014). Infrared data at arcsec resolution has been obtained from Spitzer. These are considered upper limits due to non-negligible contributions from the central dusty disk of the AGN. The data points obtained using filter UVW2 and UVM2 of XMM-Optical Monitor, in July 2005 by Younes et al. (2012) are also included. For the modeling, HST data points are preferred over XMM-Optical Monitor data points due to their lower resolution.

b) NGC 4261

We have used the radio to UV data compiled by de Menezes et al. (2020). The radio data from VLA and VLBI has been taken (Jones & Wehrle 1997, Nagar et al. 2005). The mid-infrared data was taken as sub-arcsec resolution images obtained using VISIR (Asmus et al. 2014).

²NRAO is a facility of the National Science Foundation operated under co-operative agreement by Associated Universities, Inc.

c) NGC 1275

Almost simultaneous radio observations taken in August - September 2008 by VLBA as part of Monitoring Of Jets in Active galactic nuclei with VLBA Experiments (MO-JAVE) and 600-meter ring radio telescope RATAN-600 of the Special Astrophysical Observatory, Russian Academy of Sciences, have been used in this work (Abdo et al. 2009a).

d) NGC 4486

The radio to UV data compiled for the quiescent phase from aperture radius ~ 0.4 arcsec by Prieto et al. 2016 has been used in our study.

The radio emission from the kilo-parsec jets of NGC 315 and NGC 4261 has been observed owing to the good resolution of VLA. The radio flux of 74 mJy and 50 mJy are observed at 5 GHz for the kilo-parsec jet [in the region between 3.2 to 16.2 arcsec from the nucleus] of NGC 315 (Worrall et al. 2007a) and [measured in the region between 8.8 to 31.7 arcsec from the nucleus] of NGC 4261 (Worrall et al. 2010), respectively.

3.2.2 X-ray emission

a) NGC 315

Due to low spatial resolution, jet emission can not be distinguished from the core³ in XMM-Newton and Swift-XRT observations. Recent observations of 2019 taken by XMM-Newton and multiple observations taken by Swift between 2017 and 2018 were combined and analyzed. The details on the data extraction and subsequent analysis for each instrument are given in Section 3.2.2 and 3.2.2.

³Here, we define core as the data corresponding to the unresolved structures

Owing to the high spatial resolution of *Chandra* observatory, X-ray jet emission has been resolved between 3.6 and 16.2 arcsec from the core. The power-law index for X-ray spectrum is calculated to be $\alpha = 1.2 \pm 0.2$ with an X-ray luminosity of $4.3 (\pm 0.2) \times 10^{40}$ ergs s^{-1} in 0.3-5.0 keV (Worrall et al. 2007a).

b) NGC 4261

Due to faintness, recent Swift observations recorded low counts and did not provide a good data set; thus, we compiled the previous measurement in an X-ray for NGC 4261. *Chandra* recorded the soft X-ray data with an exposure time of 35 ks. The flux (2 - 10 keV) and photon index are reported as 6.97×10^{-13} ergs $cm^{-2} s^{-1}$ and $1.54^{+0.71}_{-0.39}$, respectively (Zezas et al. 2005).

Worrall et al. (2010) analyzed 100 ks *Chandra* observation and could resolve jet emission out to 31.7 arcsec with a photon spectral index $\alpha = 1.22 \pm 0.22$ with an X-ray luminosity of $2.9 (\pm 0.2) \times 10^{39}$ ergs s^{-1} in 0.3-5.0 keV.

c) NGC 1275

The soft X-ray data from *Chandra* and hard X-ray data from Swift-BAT were reconstructed from the previous literature. The photon index and the total integral flux in the 2–10 keV band reported are 2.11 ± 0.16 and 1.14×10^{-11} ergs $cm^{-2} s^{-1}$ (Tanada et al. 2018b). Though *Swift-BAT* observations could not resolve the nucleus spatially, non-thermal hard X-ray emission from the nucleus with a photon index of $1.7^{+0.3}_{-0.7}$ was inferred. The corresponding luminosity was reported as 8×10^{42} ergs s^{-1} in 0.5-8 keV energy band (Ajello et al. 2009).

d) NGC 4486

There are multiple observations with *XMM-Newton* from 2017. We analyze the observation with the maximum exposure time. The analysis details are given in Section 3.2.2.

The spectral analysis for the reduced data from *XMM-Newton* and *Swift* has been performed using *XSPEC* version 12.10.0f (see Section 2.2.2). The errors are quoted at a 90% confidence level.

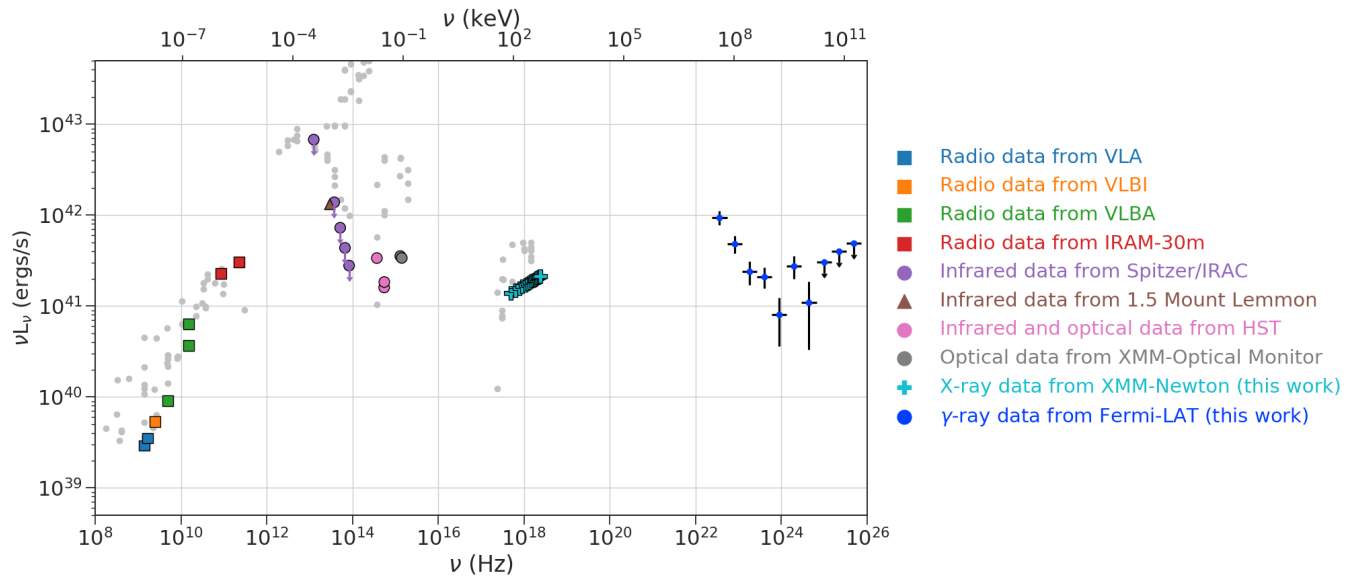


Figure 3.3: The multiwavelength SED of NGC 315 constructed using radio data taken from Capetti et al. (2005), Lazio et al. (2001), Nagar et al. (2005), Agudo et al. (2014), Kovalev et al. (2005) and Venturi et al. (1993), infrared data taken from Gu et al. (2007), Heckman et al. (1983) and Verdoes Kleijn et al. (2002), optical data taken from Verdoes Kleijn et al. (2002) and Younes et al. (2012), X-ray data taken from Worrall et al. (2007b). Other data points from NED are shown in silver.

XMM-Newton

The observation data files are obtained from the *XMM-Newton* Science archive⁴ (XSA) and are reduced using the Science Analysis System (SAS; v18.0.0). The event list obtained is filtered of any high flaring background activity, which is further

⁴XSA: <http://nxsa.esac.esa.int/nxsa-web/home>

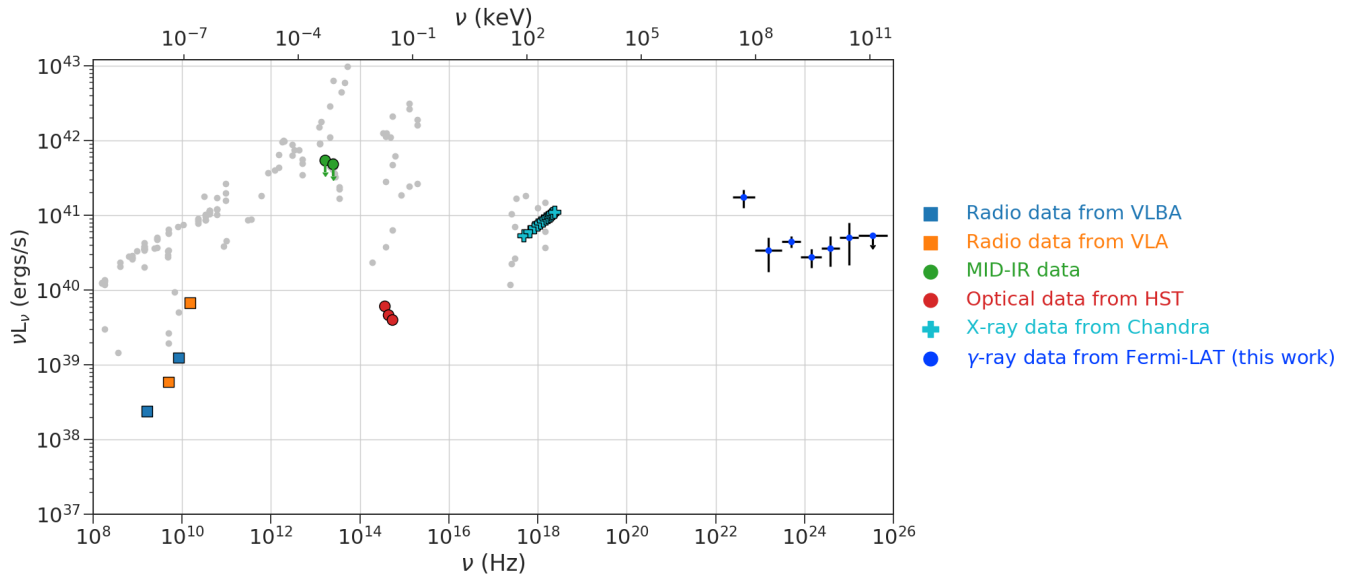


Figure 3.4: The multiwavelength SED of NGC 4261 constructed using radio data taken from Jones & Wehrle (1997), Nagar et al. (2005), infrared data taken from Asmus et al. (2014), optical data taken from Ferrarese et al. (1996). The X-ray observation is taken from Zezas et al. (2005). Other data points from NED are shown in silver. The higher flux in radio is due to low-resolution measurements, which could have a significant contribution from the radio lobes of NGC 4261.

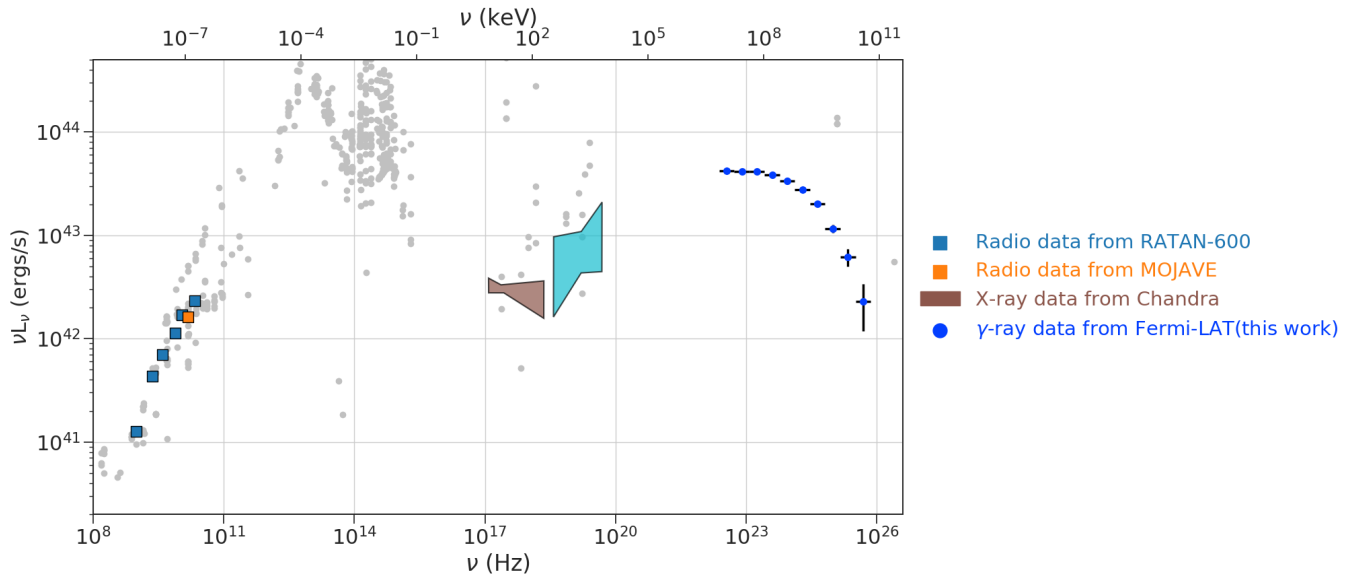


Figure 3.5: The multiwavelength SED of NGC 1275 is constructed using radio data from Abdo et al. (2009a). X-ray data has been taken from Tanada et al. (2018a) and Ajello et al. (2009). Other data points from NED are shown in silver.

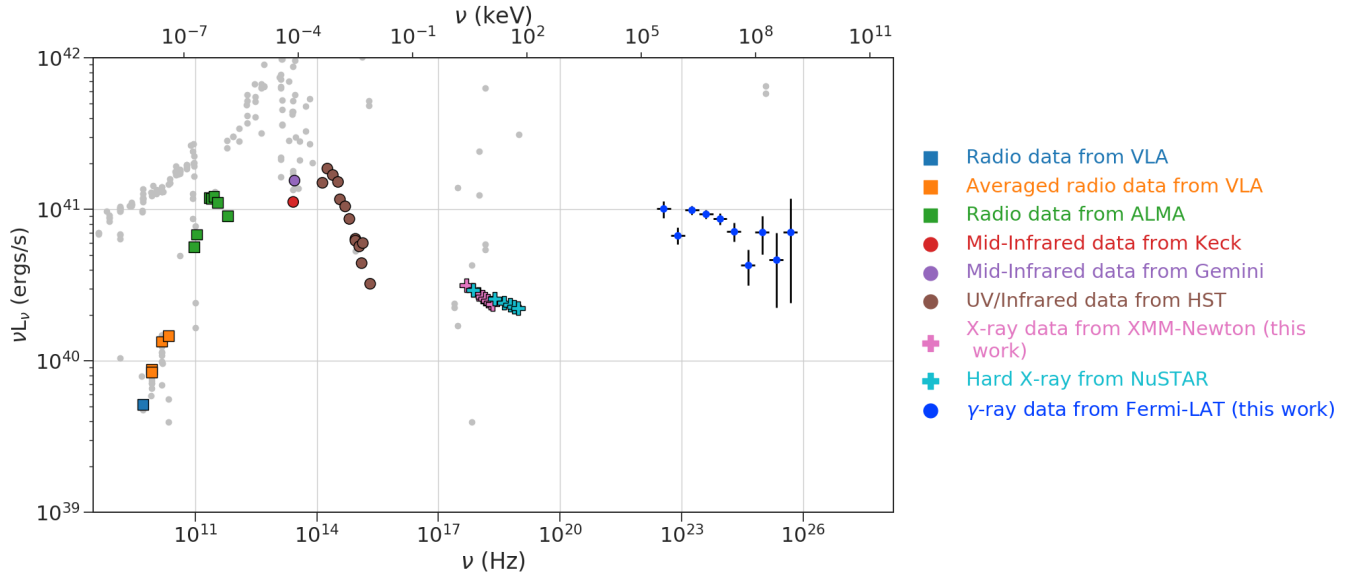


Figure 3.6: The multiwavelength SED of NGC 4486 constructed using data taken from Nagar et al. (2001), Prieto et al. (2016), Whysong & Antonucci (2004) and Perlman et al. (2001). Other data points from NED are shown in silver. The higher flux in radio is due to low-resolution measurements, which could have a significant contribution from the radio lobes of NGC 4486.

used to obtain the science products using single events ($\text{PATTERN} = 0$) ≥ 0.3 keV for MOS and up to 12 keV for EPIC-pn camera. Only events with patterns 0–4 (single and double) for the PN and 0–12 for the MOS were selected. The EPIC observations are corrected for pile-up if present. The response matrix files using the SAS task `rmfgen` are generated, while the ancillary response files are generated using the task `arfgen` in SAS.

The spectral analysis was performed in the 0.5–10.0 keV energy range. The photo-electric cross-sections and the elemental abundances of Wilms et al. (2000) are used throughout to account for absorption by neutral gas. An absorbed Galactic column density fixed to the value obtained by the `w3Nh` tool⁵ was applied to the spectral models to account for the Galactic absorption.

⁵w3Nh: Nhvalue: <https://heasarc.gsfc.nasa.gov/cgi-bin/Tools/w3nh/w3nh.pl>

a) NGC 315

XMM-Newton made an observation of ~ 50.9 ks of NGC 315 on 2019 January 27 (Obs ID: 0821871701). The EPIC-pn and MOS cameras on board XMM-Newton were operated in Prime Full Frame using the medium filter. We extract the source events from a circle with a radius of 25 arcsec centered on the source. The background events are extracted from a circle with a radius of 50 arcsec on the same CCD away from the source. We group the spectra to have a signal-to-noise ratio of 3 with a minimum of 20 counts per bin for better statistics, thus allowing the use of the χ^2 statistics. All three EPIC spectra were fitted simultaneously, allowing for a cross-normalisation between them. The spectra is fitted with model (ztbabs*po)+mekal with a reduced- χ^2 value 1.18 (190 d.o.f). The model ztbabs and mekal consider the intrinsic absorption and the thermal emission below 2 keV, respectively. We obtain a power-law index of 1.73 ± 0.10 and an average flux of $5.7_{-0.4}^{+0.3} \times 10^{-13}$ ergs cm $^{-2}$ s $^{-1}$ over an energy range 2.0-10.0 keV.

b) NGC 4486

We analyzed a 132 ks observation (Obs. ID: 0803670501) taken on July 6th, 2017. Following the analysis of XMM-Newton by Böhringer et al. (2001), we extracted source spectra from circular regions of 4 arcsec for each PN, MOS1, and MOS2 (see Section 2.2.4). The background spectra for each were extracted from a circular region of 20 arcsec away from the source. We group the spectra to have a signal-to-noise ratio of 3. For PN and MOS1, we group the spectra to have a minimum of 25 counts per bin. Due to low counts in MOS2, we bin the spectra with a minimum of 1 count per bin. Following this, the three spectra could not be fitted simultaneously since χ^2 statistics could not be used for the MOS2 spectrum. We fit the PN spectrum with a pow plus mekal model with reduced- χ^2 value 1.21 (75 d.o.f.).

The addition of another absorption component for intrinsic absorption was not significant. The flux and power-law index obtained for the best-fit in the energy range 2.0-10.0 keV are $1.51_{-0.13}^{+0.02} \times 10^{-12}$ ergs cm⁻² s⁻¹ and $2.19_{-0.30}^{+0.22}$ respectively. We obtain a temperature value of $1.37_{-0.23}^{+0.25}$ keV with an abundance set at 1, which is compatible with the values obtained by [Donato et al. \(2004\)](#). We use the same model for MOS1 and MOS2 spectra. A power-law index of $2.14_{-0.23}^{+0.19}$ and corresponding flux of $1.70_{-0.19}^{+0.16} \times 10^{-12}$ ergs cm⁻² s⁻¹ in 2.0-10.0 keV range are obtained for MOS1 with reduced- χ^2 value 1.3 (34 d.o.f.). Due to poor statistics, the parameters could not be well constrained for MOS2 and, thus, are ignored (though a rough fit provides values compatible with those obtained with PN and MOS1 spectra).

Swift

XRT data reduction was performed using the standard data pipeline package (XRTPipeline v0.13.5) to produce cleaned event files. Source events are extracted within a circular region with a radius of 30 arcsecs centered on the source positions, while background events are extracted from a source-free region with a radius of 60 arcsecs close to the source region of interest. The spectra are obtained from the corresponding event files using the XSELECT v2.4g software; we created the ancillary response file using the task `xrtmkarf`. The photo-electric cross sections and the solar abundances of [Wilms et al. \(2000\)](#) are used to account for absorption by neutral gas. An absorbed Galactic column density derived for the source from [Kalberla et al. \(2005\)](#) (obtained with the w3Nh tool) was applied to the spectral model.

a) NGC 315

Due to low counts in a single spectrum, we combine the spectra at multiple epochs using the FT00LS task `addspec`. The background spectra are summed using task

mathpha. We bin the spectra to contain a minimum of 5 counts per bin using task grppha. We use Cash statistics instead of χ^2 statistics since the number of counts per bin is less than 20 (details on fit statistics provided in Section 2.2.2). We summed eleven spectra obtained between 2017 and 2018 for a total exposure of 20.8 ks. We fit the resultant spectrum using an absorbed power-law (ztbabs*po) and found a good fit with a C-stat of 76.12 for 52 d.o.f. The residuals below 2 keV are further modeled by adding a mekal component at kT = 0.56 keV, improving the C-stat with a value of 58.18 (for 50 d.o.f.). This value agrees with the value found by González-Martín et al. (2006). The average flux and photon index obtained in the energy range 2.0-10.0 keV is $3.7_{-1.6}^{+0.8} \times 10^{-13}$ ergs cm⁻² s⁻¹ and $2.11_{-0.6}^{+0.9}$, respectively.

3.2.3 Gamma-ray Data from Fermi-LAT

The data collected by Fermi-LAT during a period of 10.25 years for NGC 315 and NGC 4261 was analyzed by de Menezes et al. (2020). We analyzed the data set collected over a period of 12 years ranging from 2008 August 4 to 2020 August 21 for all 4 sources with fermitools v2.0.0, fermipy v1.0.0 (Wood et al. 2017), and Pass 8 event processed data (Atwood et al. 2013). The events are selected in 100 MeV to 300 GeV energy range in a 15° × 15° region of interest (ROI) centered on the positions of each AGN. The data are binned spatially with a scale of 0.1° per pixel and 8 logarithmically spaced bins per energy decade.

We only selected the Source class events (evclass = 128 and evtype = 3) with the recommended filter expression (DATA_QUAL>0 && LAT_CONFIG == 1). Also, a maximum zenith angle cut of 90° was applied to reduce the contamination from secondary γ -rays from the Earth limb.

We included the standard diffuse templates, gll_iem_v07 and iso_P8R3_SOURCE_V2_v1,

available from the Fermi Science Support Center ⁶ (FSSC), to model the Galactic diffuse emission and isotropic extragalactic emission, respectively.

To quantify the significance of γ -ray detection from each source, we used the test-statistics (TS ⁷) obtained in binned likelihood analysis using `minuit`.

Spectral Models for Fitting Gamma-ray Data

A binned maximum likelihood analysis is performed by taking into account all the sources included in the updated fourth source catalog (4FGL-DR2; Abdollahi et al. 2020, Ballet et al. 2020) and lying up to 5° outside the ROI to obtain the spectral parameters and the significance of detection of the source.

An automatic ROI optimization was performed using function `optimize` within the package to ensure that all the parameters are close to their global likelihood maxima. To look for any additional sources in our model which are not included in the 4FGL (or 4FGL-DR2) catalog, we used `find_sources()` with a power-law model with `index 2`, `sqrt_ts_threshold = 5.0` and `min_separation = 0.5`. When detected with $TS > 25$, additional sources were included during the LAT analysis.

The normalization of all the sources with a radius of 5° from the ROI and the isotropic and Galactic diffuse emission templates were left to vary. The spectral shape parameters of the four LLAGNs were also kept free, while those of the other sources were fixed at the values in the 4FGL catalog.

The following spectral models are explored for the whole energy range :

1. Power-Law :

$$\frac{dN(E)}{dE} = N_o \left(\frac{E}{E_o} \right)^{-\Gamma} \quad (3.1)$$

⁶<https://fermi.gsfc.nasa.gov/ssc/data/access/lat/BackgroundModels.html>

⁷TS = $-2 (\log \mathcal{L}_0 - \log \mathcal{L}_1)$ where \mathcal{L}_0 , \mathcal{L}_1 are the maximum likelihood for the model without an additional source and with an additional source at the specified location, respectively Mattox et al. 1996.

where the normalization N_o and γ -ray photon index Γ are considered as free parameters. The scale value E_o is fixed at its catalog value (Ajello et al. 2020, Lott et al. 2020).

2. Log Parabola:

$$\frac{dN(E)}{dE} = N_o \left(\frac{E}{E_o} \right)^{-\alpha - \beta \ln(E/E_o)} \quad (3.2)$$

where N_o , α and β are the free parameters.

3. Power Law with exponential cut-off:

$$\frac{dN(E)}{dE} = N_o \left(\frac{E}{E_o} \right)^{-\Gamma} \exp \left(\frac{-E}{E_c} \right) \quad (3.3)$$

where N_o , Γ and E_c are the free parameters.

Results of Gamma Ray Spectral Analysis

The significance of spectral curvature is determined to determine the best-fit spectral model of each source. The spectral curvature is significant if $TS_{curve} > 16$ (corresponding to 4σ ; Acero et al. 2015).

a) NGC 315

No significant curvature is seen in the γ -ray SED of NGC 315. Its γ -ray spectrum is defined by a power-law with $\Gamma = 2.53 \pm 0.11$ detected with $\approx 11.1 \sigma$ (TS=123.7). An integrated flux of $3.1 (\pm 0.41) \times 10^{-12}$ ergs cm^{-2} s^{-1} over 0.1-300 GeV is obtained.

b) NGC 4261

It is the faintest in our sample with statistical significance detection of 8.2σ (TS = 67.24). As shown in Figure 3.7, no cut-off is seen in the spectrum. The 12 years averaged spectrum obtained is well represented by a power-law with $\Gamma = 2.04 \pm 0.15$

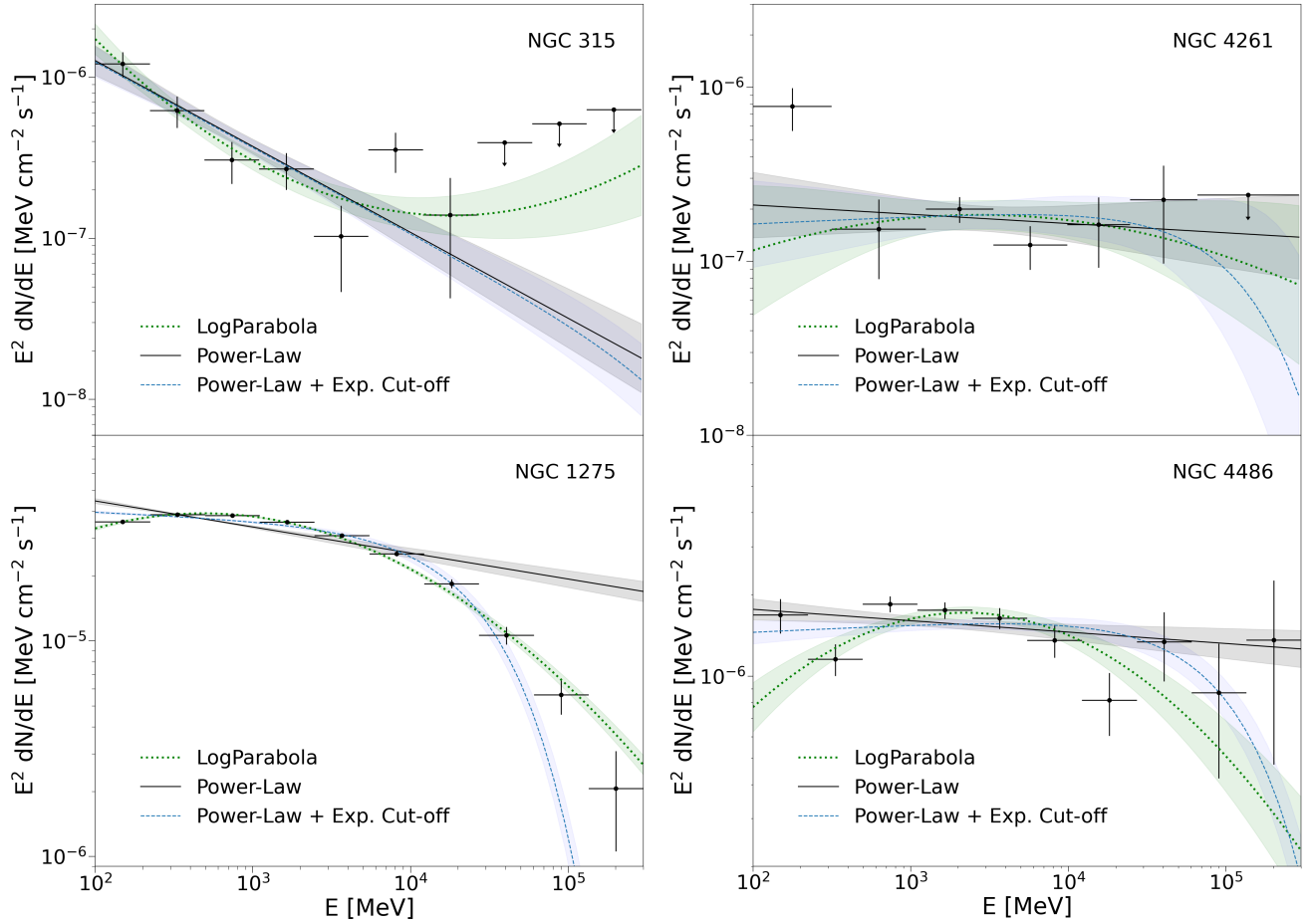


Figure 3.7: The γ -ray SED obtained by *Fermi*-LAT from 12 years of observations. The shaded part corresponds to 1σ -uncertainty in the respective fit. When $TS < 4$, upper limits at 95% confidence level are plotted with a down arrow.

with corresponding integrated flux over 0.1-300 GeV of $2.27(\pm 0.4) \times 10^{-12}$ ergs $\text{cm}^{-2} \text{s}^{-1}$.

c) NGC 1275

Figure 3.7 clearly indicates a curvature in the spectrum. The source is detected with a high statistical significance of 376.6σ ($TS = 141829.6$) with our likelihood analysis. The log-likelihood ratio test ($\Delta TS \sim 383.6$ i.e. 19.6σ) signifies that a log-parabola model is a better representation over a single power-law model with an integrated flux of $3.1(\pm 0.03) \times 10^{-10}$ ergs $\text{cm}^{-2} \text{s}^{-1}$ over the energy range 0.1-300

GeV with best-fit indices $\alpha = 2.08 \pm 0.01$ and $\beta = 0.065 \pm 0.003$.

d) NGC 4486

Our likelihood analysis detected the source with high statistical significance $TS=1844.52$ ($\sim 43\sigma$). The average spectrum is well-defined by a power law of photon index, $\Gamma = 2.04 \pm 0.03$ and integrated flux, $F_{0.1-300\text{GeV}} = 1.94 (\pm 0.09) \times 10^{-11} \text{ ergs cm}^{-2} \text{ s}^{-1}$.

3.3 Multi-wavelength SED Modeling

We consider homogeneous and spherical emission region of radius R moving through the magnetic field B inside the jet with a bulk Lorentz factor Γ_b . This region contains relativistic plasma of electrons and protons and emits radiation through the synchrotron and inverse-Compton processes (detailed in Section 2.3).

A simple power-law injection spectrum is expected in the case of Fermi-I-type acceleration. While a power-law is supported by the γ -ray SED fits for NGC 315, NGC 4261 and NGC 4486, presence of curvature in the γ -ray SED of NGC 1275 hints at a different particle distribution. As suggested by [Massaro et al. \(2004\)](#), the injected particles may show an intrinsic curvature following a log-parabolic distribution due to energy-dependent acceleration, which is supported by the best-fit results for γ -ray SED of NGC 1275.

Thus, we consider a constant injection spectrum $Q = Q(E)$ following a power-law distribution,

$$Q(E) = L_0 \left(\frac{E}{E_{ref}} \right)^{-\alpha} \quad (3.4)$$

Table 3.1: Parameter results for γ -ray SED obtained by Fermi-LAT fitted using different spectral models in the range 100 MeV to 300 GeV

| Source | Model | Parameter Values ^a | Flux _{0.1–300GeV} [ergs cm ⁻² s ⁻¹] | TS _{curve} ^b |
|---------------------------------|--------------------------------------|--|--|----------------------------------|
| NGC 315 (4FGL J0057.7+3023) | Power-Law | $\Gamma = 2.53 \pm 0.11$ | $3.81(\pm 0.41) \times 10^{-12}$ | - |
| | Log-Parabola | $\alpha = 2.52 \pm 0.08$ $\beta = -0.09 \pm 0.03$ | $4.51(\pm 0.75) \times 10^{-12}$ | 3.16 |
| | Power-Law with Exponential Cutoff | $\Gamma = 2.53 \pm 0.11$ $E_c = 0.9 \text{ TeV}$ | $3.73(\pm 0.40) \times 10^{-12}$ | -1.7 |
| NGC 4261 (4FGL J1219.6+0550) | Power-Law | $\Gamma = 2.05 \pm 0.15$ | $2.22(\pm 0.42) \times 10^{-12}$ | - |
| | Log-Parabola | $\alpha = 1.99 \pm (0.19)$ $\beta = 0.04 \pm 0.09$ | $1.92(\pm 0.69) \times 10^{-12}$ | -0.58 |
| | Power-Law with Exponential Cutoff | $\Gamma = 1.95 \pm 0.22$ $E_c = 0.1 \text{ TeV}$ | $1.97(\pm 0.54) \times 10^{-12}$ | 2.34 |
| NGC 1275 (4FGL J0319.8+4130) | Power-Law | $\Gamma = 2.12 \pm 0.02$ | $3.70(\pm 0.05) \times 10^{-10}$ | - |
| | Log-Parabola | $\alpha = 2.08 \pm 0.01$ $\beta = 0.065 \pm 0.003$ | $3.10(\pm 0.03) \times 10^{-10}$ | 383.6 |
| | Power-Law with Exponential Cutoff | $\Gamma = 2.03 \pm 0.01$ $E_c = 30.8 \pm 2.6 \text{ GeV}$ | $3.02(\pm 0.02) \times 10^{-10}$ | 351.1 |
| NGC 4486 (4FGL J1230.8+1223) | Power-Law | $\Gamma = 2.04 \pm 0.03$ | $1.94(\pm 0.09) \times 10^{-11}$ | - |
| | Log-Parabola | $\alpha = 1.94 \pm 0.04$ $\beta = 0.08 \pm 0.02$ | $1.48(\pm 0.11) \times 10^{-11}$ | -18.6 |
| | Power-Law with Exponential Cutoff | $\Gamma = 1.97 \pm 0.03$ $E_c = 0.13 \text{ TeV}$ | $1.69(\pm 0.08) \times 10^{-11}$ | -51.1 |

^a Symbols are as defined in Section 2.1.2

^b $TS_{curve} = 2 (\log \mathcal{L}(\mathcal{M}) - \log \mathcal{L}(\text{PL}))$ where \mathcal{L} is the maximum likelihood of the model, \mathcal{M} is either a Log-Parabola or a Power Law with Exponential Cutoff spectral model. PL is a Power-Law spectral model.

for NGC 315, NGC 4261 and NGC 4486 and a log-parabola distribution,

$$Q(E) = L_0 \left(\frac{E}{E_{ref}} \right)^{-\alpha - \beta \ln(E/E_{ref})} \quad (3.5)$$

for NGC 1275, where $E_{ref} = 1 \text{ TeV}$ is the reference energy. The injection spectral index (α), the curvature index (β) and the normalization constant of the spectrum

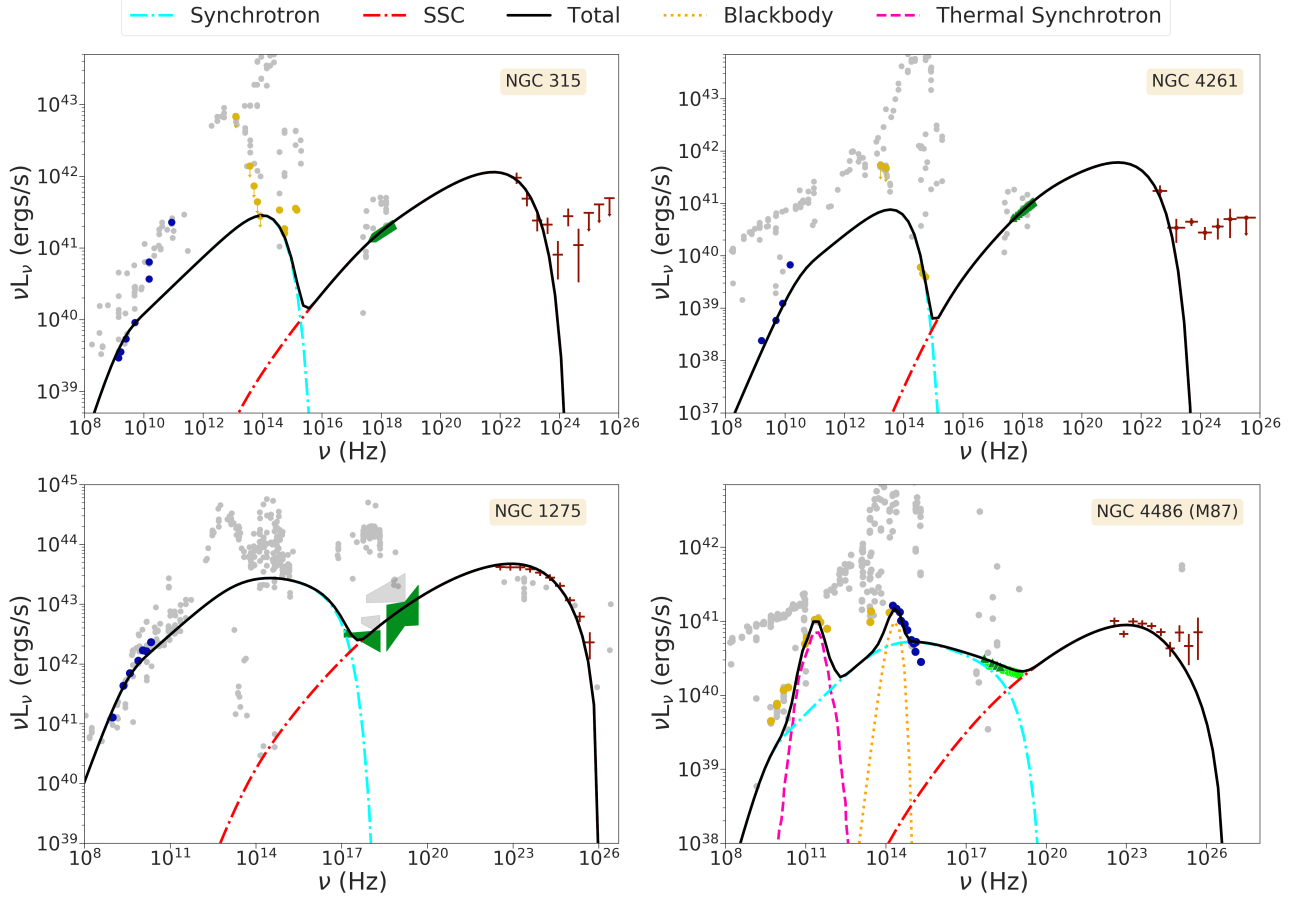


Figure 3.8: One zone leptonic modeling of broadband emission from sub-parsec scale jets of the four LLAGNs. The thermal synchrotron and the blackbody components of M87 have been reproduced from Lucchini et al. (2019). The gamma-ray data beyond 1.6 GeV from NGC 315 and 0.6 GeV from NGC 4261 cannot be explained with one zone SSC model.

(L_0) are free parameters and are determined from the modeling.

We calculate the particle spectrum $N = N(E, t)$ at a time t at which the spectrum is assumed to attain a steady state under the continuous injection of particles described by $Q(E)$ and energy losses given by the energy loss rate $b = b(E, t)$ using publicly available time-dependent code GAMERA⁸(Hahn 2015). The code solves the 1D transport equation,

$$\frac{\partial N}{\partial t} = Q(E, t) - \frac{\partial(bN)}{\partial E} - \frac{N}{t_{esc}} \quad (3.6)$$

⁸GAMERA: http://libgamera.github.io/GAMERA/docs/main_page.html

Table 3.2: Parameter Values for the best-fit one-zone leptonic SSC model

| Parameter | Symbol | NGC 315 | NGC 4261 | NGC 1275 | M87 |
|---|----------------|----------------------|-----------------------|-----------------------|-----------------------|
| Injection Spectrum Type | Q_i | Power-Law | Power-Law | Log-Parabola | Power-Law |
| Minimum Electron Lorentz factor | γ_{min} | 35 | 190 | 72 | 40 |
| Maximum Lorentz factor | γ_{max} | 2.5×10^4 | 1.6×10^4 | 5.4×10^5 | 2.8×10^6 |
| Escape time coefficient | η_{esc} | 1 | 1 | 1 | 6 |
| Alpha | α | 2.2 | 2.06 | 2.25 | 2.27 |
| Beta (Curvature Index) | β | - | - | 0.015 | - |
| Lorentz factor | Γ_b | 1.5 | 1.5 | 1.8 | 3.3 |
| Doppler Factor | δ | 1.6^a | 1^a | 2.3^b | 2.3^c |
| Blob Radius (cm) | R | 1.1×10^{16} | 1×10^{16} | 3.13×10^{17} | 4.1×10^{15} |
| Magnetic Field (G) | B | 0.21 | 0.21 | 0.07 | 0.24 |
| Jet power in electrons (ergs/s) | P_e | 3.9×10^{37} | 4.8×10^{37} | 8.1×10^{36} | 1.04×10^{37} |
| Jet power in magnetic field (ergs/s) | P_B | 4.5×10^{40} | 3.72×10^{40} | 5.8×10^{42} | 3.9×10^{40} |
| Jet power in cold protons ^d (ergs/s) | P_p | 4.7×10^{38} | 1.12×10^{38} | 2.69×10^{37} | 1.06×10^{38} |
| Total jet power (ergs/s) | P | 4.5×10^{40} | 3.74×10^{40} | 5.8×10^{42} | 3.96×10^{40} |
| Eddington Jet power (ergs/s) | P_{edd} | 9.9×10^{46} | 6.1×10^{46} | 3.60×10^{45} | 8.17×10^{47} |

^a Adopted from [de Menezes et al. \(2020\)](#).

^b Adopted from [Abdo et al. \(2009a\)](#).

^c It is close to the value ($\delta = 2.8$) used by [Fraija & Marinelli \(2016\)](#).

^d Assuming the number of protons equals the number of radiating electrons in the jet.

where t_{esc} is the timescale over which the leptons escape from the emission region.

We consider escape time as $t_{esc} = \eta_{esc} \frac{R}{c}$ and η_{esc} is considered as a free parameter (≥ 1).

The code subsequently calculates the synchrotron and inverse-Compton emission, which is Doppler boosted by a factor of δ^4 in the observer's frame due to relativistic beaming. $\delta = [\Gamma_b(1 - \beta \cos\theta)]^{-1}$ is the Doppler factor, Γ_b is the bulk Lorentz factor, β is the intrinsic speed of the emitting plasma, and θ is the viewing angle of the jet with respect to the line of sight of the observer.

The simulated spectral energy distributions are fitted to the data points by adjusting the parameters in [Table 3.2](#).

The total required jet power is calculated as,

$$P_{tot} = \pi R^2 \Gamma_b^2 c (U'_e + U'_B + U'_p) \quad (3.7)$$

where U'_e , U'_B and U'_p are the energy densities of electrons, magnetic field, and protons in the comoving frame of jet respectively. These are defined as follows:

$$U'_e = \frac{1}{V} \times \int_{E_{min}}^{E_{max}} Q(E) E dE \quad (3.8)$$

$$U'_B = \frac{B^2}{8\pi} \quad (3.9)$$

and

$$U'_p = n_p m_p c^2 \quad (3.10)$$

where V is the volume of the emission region, m_p is the mass of the proton, and n_p is the number density of protons, which is equal to the number density of electrons, assuming the jet contains equal numbers of electrons and protons to maintain charge neutrality.

3.3.1 SSC Model for Jet Emission

As for blazars, the spectral energy distribution of most radio galaxies is well interpreted by a single zone SSC model (e.g., [Abdo et al. 2010c](#), [Abdo et al. 2009b](#)). Within this framework, radio-to-optical photons are produced by synchrotron radiation of the non-thermal electron population in the magnetic field. X-rays of higher energy photons are produced by upscattering the synchrotron photons by the same electron population. While this model can explain the broadband SED of NGC 1275 and NGC 4486 up to 0.3 TeV and 8 GeV, respectively, it fails to do so for

NGC 315 beyond 1.6 GeV and NGC 4261 beyond 0.6 GeV. The modeling results can be seen in Figure 3.8.

3.3.2 Multi-wavelength Emission from Extended jet

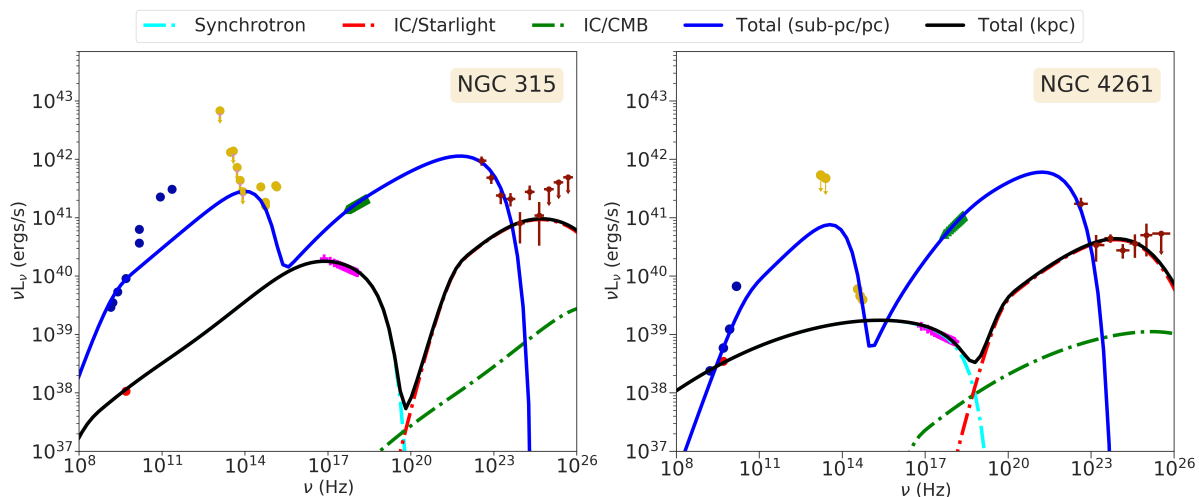


Figure 3.9: Leptonic model for emission from sub-parsec (blue) and extended jets (black) for NGC 315 and NGC 4261. The radio and X-ray data for the extended jets are shown in red and pink, respectively.

The low angular resolution of instruments at γ -ray energies does not allow us to distinguish between jet and extended jet emission. We invoke the emission from the kilo-parsec scale jets of NGC 315 and NGC 4261 since the SSC emission from their sub-parsec scale jets cannot fit the γ -ray data points beyond 1.6 GeV and 0.6 GeV energy, respectively.

The radio and X-ray photon flux from the extended jets of NGC 315 and NGC 4261 can be well fitted with synchrotron emission by the relativistic electrons (Worrall et al. 2007a, Worrall et al. 2010). This implies that the extended jets could also be sources of high and very high energy photons due to inverse Compton scattering of starlight photons from the host galaxy by the relativistic electrons in the extended jets (Stawarz et al. 2003). The starlight energy density at the extended jet of NGC 4261 has been adopted from Worrall et al. (2010). For NGC 315, the typical

Table 3.3: Parameter values for the best-fit one-zone leptonic model for kilo-parsec jet

| Parameter | Symbol | NGC 315 | NGC 4261 |
|--------------------------|---------------------------|------------------------|------------------------|
| Starlight energy density | $U_{star}(\text{ergs/s})$ | 2.25×10^{-9} | 2.09×10^{-10} |
| Dust energy density | $U_{dust}(\text{ergs/s})$ | 2.25×10^{-11} | 2.09×10^{-12} |
| CMB energy density | $U_{cmb}(\text{ergs/s})$ | $9. \times 10^{-13}$ | $9. \times 10^{-13}$ |
| Minimum Lorentz factor | γ_{min} | 1400 | 220 |
| Maximum Lorentz factor | γ_{max} | 5.0×10^8 | 5.2×10^8 |
| Spectral index | α | 2.1 | 2.16 |
| Curvature index | β | 0.025 | 0.084 |
| Magnetic field | B (G) | 10×10^{-6} | 5.7×10^{-6} |
| Radius | R (cm) | 5×10^{21} | 1×10^{21} |
| Escape time factor | η_{esc} | 1 | 1 |
| Bulk Lorentz factor | Γ_b | 1.5 | 1.5 |
| Doppler factor | δ | 1.6 | 1 |
| Total kpc jet power | $P_{tot}(\text{ergs/s})$ | 2.1×10^{43} | 2.7×10^{41} |

energy density of starlight in kilo-parsec scale jet for FRI radio galaxies has been adopted (Stawarz et al. 2006). We have also considered IC/CMB emission, as has been suggested for other large-scale X-ray jets (Zacharias & Wagner 2016), where CMB photons are up scattered by the relativistic electrons, but it is found to be sub-dominant as compared to IC/starlight emission.

We calculate the synchrotron, IC/starlight, and IC/CMB emission from kiloparsec scale jets by considering the constant escape time of electrons from the emission region as R/c . We assume the same bulk Lorentz factor and viewing angle for the spherical emission region or blob in the kiloparsec scale jet as in the sub-parsec scale jet. The results are shown in Figure 3.9, and the corresponding parameters are given in Table 3.3.

3.4 Summary and Conclusions

LLAGNs are important to study as their number is expected to be much higher than the high luminosity AGNs, and they have been speculated to be acceleration sites

of cosmic rays (Rodrigues et al. 2021, Das et al. 2020). Detection of these sources by gamma-ray detectors is necessary to support this speculation. The four LLAGNs NGC 315, NGC 4261, NGC 1275, and NGC 4486 have been detected in gamma-rays before. Hence, we have selected these sources for a more extended analysis. We have analyzed the XMM-Newton data from NGC 315 and NGC 4486 and Swift data from NGC 315. We have also analyzed the Fermi-LAT data for all four LLAGNs, NGC 315, NGC 4261, NGC 1275, and NGC 4486, for a period of 12 years (2008-2020). We have combined the archival multi-wavelength data of these sources with our analyzed data to build the broadband spectral energy distributions of these sources (see Figure 3.3, 3.4, 3.5 and 3.6). We have found the best-fitted models for the Fermi-LAT data (see Figure 3.7), and the parameters of the fitted models are given in Table 3.1.

For NGC 4486, we find the best fit describing the Fermi-LAT SED is a power law which is consistent with the best fit obtained for the combined Fermi-LAT and MAGIC data (MAGIC Collaboration et al. 2020c) for 2012-2015. Hence, we used a power-law electron distribution in our modeling to fit the multi-wavelength SED.

The gamma-ray data points of NGC 315 and NGC 4261 are also found to be well represented by the power-law spectral model, while for NGC 1275, log-parabola distribution gives a better fit to the gamma-ray data. We have considered SSC emission from sub-parsec scale jets of these sources to fit the multi-wavelength data points (see Figure 3.8), and the corresponding values of the parameters of our model are given in Table 3.2. We have included the emission from the extended kilo-parsec scale jets of NGC 315 and NGC 4261 to explain the gamma-ray data points at higher energies (see Figure 3.9). The corresponding values of the model parameters are given in Table 3.3.

de Menezes et al. (2020) analyzed 10.25 years of Fermi data and simulated the

multi-wavelength SED of NGC 315 and NGC 4261 using one zone SSC model to compare with the observational data. The radio flux estimated in their model is lower than the observed flux for both NGC 315 and NGC 4261.

Abdo et al. (2009a) used a one-zone SSC model to fit the multi-wavelength data from NGC 1275. However, their model gives a higher X-ray flux than the observed flux.

For NGC 4486, a multizone model has also been proposed to explain the radio to X-ray emission, which gives a lower γ -ray flux (Lucchini et al. 2019) compared to the observed flux.

While ADAF or jet dominance for X-ray emission from LLAGNs remains under debate, we show that synchrotron and SSC emission from relativistic electrons in sub-parsec scale jets can explain the observed multi-wavelength data from NGC 1275, up to 1.6 GeV from NGC 315, up to 0.6 GeV from NGC 4261 and up to 8 GeV from NGC 4486. At higher energy, inverse Compton scattering of starlight photons by electrons accelerated in kilo-parsec scale jets of NGC 315 and NGC 4261 can explain the observed gamma-ray flux. The maximum value of the Lorentz factor of the order of 10^8 obtained to fit the X-ray and gamma-ray data indicates that the electrons are accelerated to ultra-relativistic energies in the kilo-parsec jets. Such high Lorentz factors also favor the synchrotron origin of X-rays from these jets, as suggested before by Worrall et al. (2007a), Worrall et al. (2010). It is also noted that strong emission of starlight photons from the host galaxy is required for these objects to be seen in GeV γ - rays. Kilo-parsec scale jet is also present in NGC 4486, whose radio-to-X-ray emission has been modeled earlier with synchrotron emission of relativistic electrons (Sun et al. 2018). The inverse Compton mechanism may also emit these relativistic electrons and contribute to the observed gamma-ray flux. The hadronic model has been used earlier to explain the

high energy gamma ray data (Marinelli et al. 2014, Fraija & Marinelli 2016). A detailed modeling of NGC 4486 to explain the high-energy gamma-ray data is beyond the scope of this paper.

Centaurus A is also considered to be a LLAGN as the luminosity of its H α emission is less than 10^{40} ergs/s (Brodatzki et al. 2011). Earlier, the High Energy Stereoscopic System (H.E.S.S.) reported extended TeV gamma-ray emission from this LLAGN (H. E. S. S. Collaboration et al. 2020b). They explained the very high energy gamma-ray emission as inverse Compton scattering of mainly the dust photons by ultra-relativistic electrons in the kilo-parsec scale jet of this source. The extended X-ray emission from the kilo-parsec scale jet of this source is explained as synchrotron emission of ultra-relativistic electrons. The kilo-parsec scale jets may also be the acceleration sites of protons and heavy nuclei, contributing to the observed spectrum of ultrahigh-energy cosmic rays. More observations of high-energy gamma rays from nearby LLAGNs would be useful in understanding their role as cosmic particle accelerators.

Nature uses only the longest threads to weave her patterns so that each small piece of her fabric reveals the organization of the entire tapestry.

Richard Feynman

4

Curious case of M81*

In this chapter, we study the association of radio and X-ray flares with the knot ejection from M81 by modeling its multi-wavelength spectral energy distribution (SED) during these flares to constrain the physical parameters of the jet. Moreover, we construct a long-term light curve in X-rays to identify the flares in the available data and constrain the jet parameters during those periods. The jet activity may vary on short and long timescales, producing flares in different frequency bands. The SEDs from radio to X-ray during the quiescent and flaring states are found to be satisfactorily explained by synchrotron emission of relativistic electrons from a single zone. The variation in the values of the jet parameters during the different states is shown, and similarities are*

drawn with high-synchrotron peaked blazars.

This chapter is based on the paper published in the *Astrophysical Journal* titled “**X-Ray Flares in the Long-term Light Curve of Low-luminosity Active Galactic Nucleus M81***” by Tomar & Gupta (2023).

4.1 M81*

M81* is located at a distance of 3.6 Mpc (Freedman et al. 1994) with an SMBH of estimated mass $7 \times 10^7 M_{\odot}$, at the center of the massive spiral galaxy NGC 3031. The bolometric luminosity of M81* is 9.3×10^{40} ergs/s, implying an Eddington ratio of M81* is 9.3×10^{40} ergs/s implying an Eddington ratio of $1.1 \times 10^{-5} L_{Edd}$, where L_{Edd} is the Eddington luminosity. The low Eddington ratio, the absence of a thin disk at the inner radius (Young et al. 1995), and its proximity makes it a prototype LLAGN to study the emission mechanisms and temporal features of LLAGNs, which remain unexplored.

Jet-dominated spectral models for M81* have previously been used to explain the data from radio to X-ray frequencies (Markoff et al. 2004), with both synchrotron and synchrotron self-Compton (SSC) as the proposed dominant mechanisms of X-ray emission, providing a good fit to the observed data. It is important to understand whether the jet activity of M81* is similar to that of the general population of high-luminosity AGNs, which have been extensively studied recently with multi-wavelength data from various telescopes.

A uniquely large radio flare (Pooley 2011) was seen to be followed by a discrete knot ejection in M81*, suggesting a similar jet-production mechanism to luminous

AGNs (King et al. 2016). An X-ray flare and a radio rebrightening were found to be associated with the ejected knot. Their result significantly impacts the understanding of the jet activity of M81*, as this indicates for the first time the presence of radial motion in the jet of a low-luminosity AGN.

We constrain the physical parameters of the jet during the emission of the discrete knot in radio frequencies by constructing and modeling the multi-wavelength SEDs. Moreover, we identify several X-ray flares in the long-term light curve of M81* (2005 April 21–2014 May 24) constructed using Swift data. The methods followed to analyze the X-ray, UV-optical, and gamma-ray data are given in Section 4.2, and the methods used to identify the flares and quiescent state are discussed in Section 4.3. We discuss the construction of the SEDs during the different states in Section 4.4.1 and, subsequently, the modeling of these SEDs is discussed in Section 4.4.2.

Our results from this work are mentioned in Section 4.5 and discussed in Section 4.6. Interestingly, we find that all the SEDs covering radio to X-ray frequencies can be explained by synchrotron emission from the jet of M81*, similar to high-synchrotron peaked blazars (HSPs) like Mrk 421 (Sinha et al. 2015).

4.2 Multi-wavelength Observations and Data Analysis

4.2.1 X-ray

The Swift telescope has monitored M81* several times between April 21, 2005 and May 24, 2021. The X-ray data were taken from the X-Ray Telescope (XRT) instrument onboard Swift, in both PC and WT modes (for details, see Section 2.2.3). The data reduction was performed using the standard data pipeline package (`xrtpipeline v0.13.5`) to produce cleaned event files. For the observations in WT mode, the

source events were extracted using a circular aperture of radius 118 arcsec, and the background events were extracted from an annular region with an inner and outer radius of 200.6 arcsecs and 271.4 arcsecs, respectively, chosen to be symmetrically placed about 100 pixels. Each observation’s count rate was below the pile-up limit (~ 100 counts s^{-1}). For the observations in PC mode, the source events were extracted from a circular region of radius 118 arcsec centered on the source. The background events were extracted from an annular region of inner radius and outer radius of 141 arcsec and 213 arcsec, respectively (King et al. 2016). The observations with the count rate above the pile-up limit (~ 0.5 counts s^{-1}) were checked for pile-up effect by modeling the XRT-PSF with Kings function following the standard procedure (briefly discussed in Appendix A). The source event files for the observations with pile-up were then extracted by excluding the events within the circle of radius up to which pile-up was significant (varying between 2 arcsec and 10 arcsec). The spectra were obtained from the corresponding event files using the `xselect v2.4g` software; we created the response files using the task `xrtmkarf` and then combined them with the source and background spectra using `grppha`. Due to low count rates, we binned the spectra with a minimum count of 1 per bin using `grppha`. We used `XSPEC` to fit each spectrum using Cash statistics (more details in Section 2.2.2).

We fit each spectrum with a simple absorbed power law (`tbabs*po`) with corresponding Galactic hydrogen column density (N_H) along the direction of M81* fixed to 5×10^{20} cm^{-2} (King et al. 2016). The power law is defined as $A(E) = KE^{-\Gamma_x}$, where the photon index Γ_x and the normalization K were allowed to vary. The flux obtained in the soft X-ray band (0.5-2.0 keV) and hard X-ray band (2.0-10.0 keV) at each epoch is shown in Figures 4.1(a) and 4.1(b), respectively.

Observation taken by another X-ray instrument, NuSTAR, during the period

of the detected flares was also analyzed for completeness. An observation was taken by *NuSTAR* on May 18, 2015, during Flare B. The data were processed using *NUSTARDAS* (v1.8.0) along with *CALDB* v20190627. The cleaned event files with an exposure of ~ 20.9 ks were obtained using *nupipeline*. We extracted the source spectrum from a circular region of radius 100 arcsec centered on the source for both Focal Plane Modules A and B (FPMA and FPMB). The background spectrum was extracted from a region of an equivalent radius away from the source. We carried out the spectral fitting over an energy range of 3.0-60.0 keV for FPMA and FPMB simultaneously using *XSPEC* with the same baseline model along with three Gaussian absorption lines with centroid energies fixed at 6.4, 6.68, and 6.96 keV (Page et al. 2004).

4.2.2 UV-Optical

M81* was monitored by Swift's Ultra-violet Optical Telescope (UVOT) in some or all of six filters, simultaneously with multiple XRT observations. We reduced the data using the standard procedures (detailed in Section 2.2.3) by extracting source counts from a circular region of a 5 arcsec radius centered on the source. In contrast, background counts were extracted from an annulus region centered on the source with inner and outer radii of 27.5 arcsecs and 35 arcsecs, respectively. We used the tool *uvotsource* to derive the magnitudes, which were then corrected for Galactic extinction using the extinction values obtained with python module *extinction* and the reddening law with $R_v = 3.1$ from Fitzpatrick (1999b). The corrected observed magnitudes were converted into fluxes using the zero-point correction flux (Breeveld et al. 2011b). The Swift-UVOT light curve is shown in Figures 4.1(c) and 4.1(d). The host galaxy flux (taken from Pian et al. 2010) was subtracted for U, W1, M2, and W2 filters.

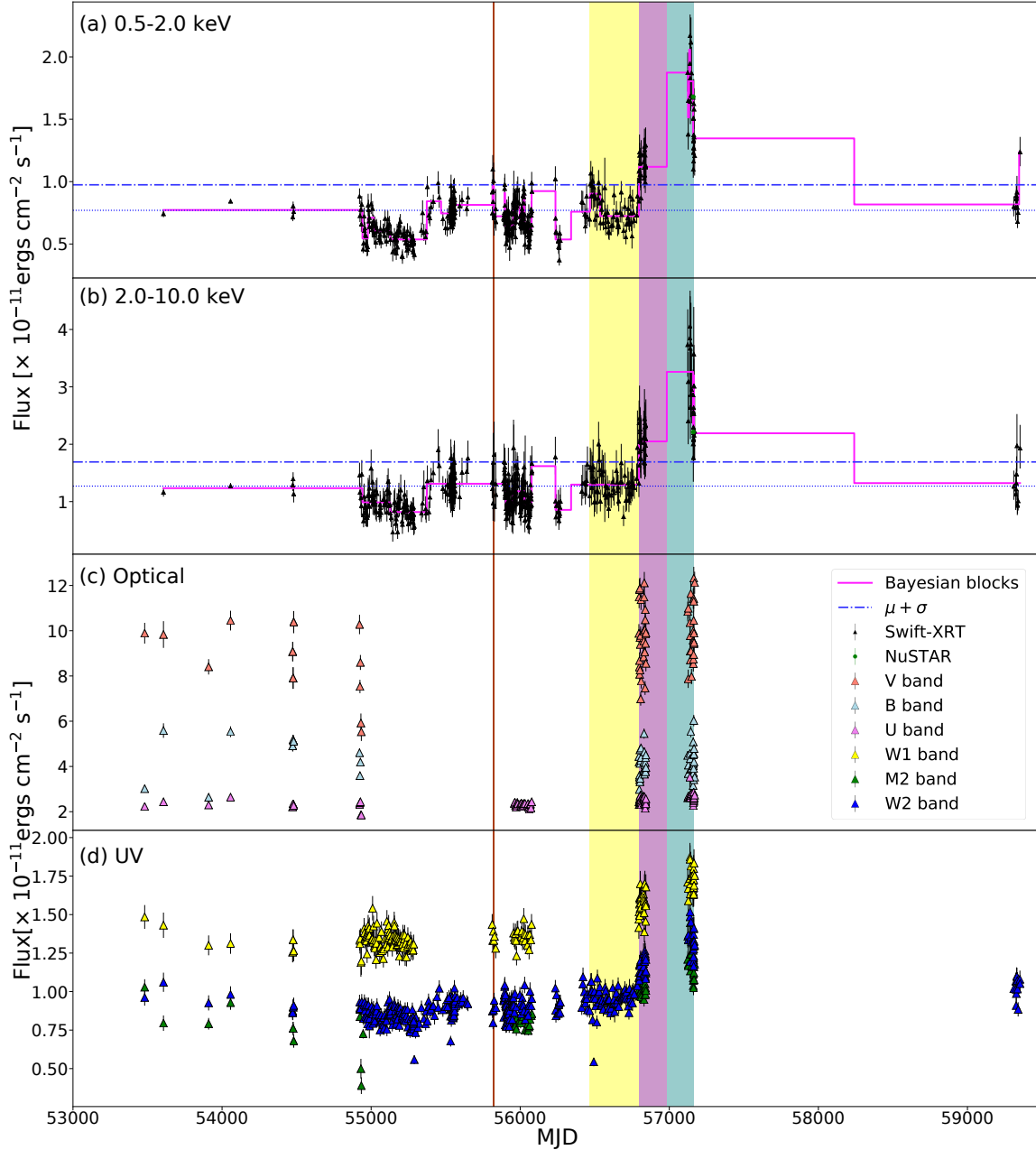


Figure 4.1: The lightcurve in (a) soft X-ray energies (0.5-2.0 keV) and (b) hard X-ray energies (2.0-10.0 keV), and the light curve in the (c) optical and (d) UV. The yellow region represents the quiescent state (MJD 56467.7 - MJD 56796.7). The brown line (MJD 55814.83 - MJD 55823.35), and the purple (MJD 56796.74 - MJD 56983.37) and teal (MJD 56983.37 - MJD 57160.25) shaded regions represent Flare A, Flare B, and Flare C, respectively.

4.2.3 Gamma-Ray

We analyzed the data collected by Fermi's Large Area Telescope (LAT; Section 2.1) over a period of ~ 13.5 yr ranging from 2008 August 8 to 2022 February 28 with

fermitools v2.0.0, fermipy v1.0.0, and Pass 8 event processed data. The extraction of gamma-ray emission from M81* is challenged by its neighbor starburst galaxy M82, a strong gamma-ray emitter, located at 0.62° away from M81*. Since the point spread function (PSF) of Fermi-LAT at lower energies is larger than the separation, contamination from M82 to gamma-ray flux cannot be ruled out (Lenain & Walter 2011). Therefore, we selected the events in the 10-300 GeV energy range, where the PSF is smaller than the separation. The events are selected in a $15^\circ \times 15^\circ$ region of interest (ROI) centered on the position of M81*. The data were spatially binned with a scale of 0.1° per pixel and eight logarithmically spaced bins per energy decade. We then manually added a point source at the center of the ROI, as M81* does not belong to the 4FGL catalog. The source was modeled with a power law spectrum.

We only selected the Source class events (`evclass = 128` and `evtype = 3`) with the recommended filter expression (`DATA_QUAL>0 && LAT_CONFIG == 1`). Also, a maximum zenith angle cut of 90° was applied to reduce the contamination from secondary gamma rays from the Earth limb. We included the standard diffuse templates, `gll_iem_v07` and `iso_P8R3_SOURCE_V2_v1`, available from the Fermi Science Support Center¹, to model the Galactic diffuse emission and the residual background and isotropic extragalactic emission, respectively.

A binned maximum-likelihood analysis was performed by taking into account all the sources included in the updated fourth source catalog (4FGL-DR2) and lying up to 5° outside the ROI to obtain the spectral parameters and the significance of detection of the source. Automatic optimization of the ROI was performed using function `optimize` within the package to ensure that all the parameters were close to their global likelihood maxima. To look for any additional sources in our

¹<https://fermi.gsfc.nasa.gov/ssc/data/access/lat/BackgroundModels.html>

model which were not included in the 4FGL catalog, we used `find_sources()` with a power law model with index 2, `sqrt_ts_threshold = 5.0`, and `min_seperation = 0.5`. When detected with $TS > 25$, additional sources were included during the LAT analysis. The normalization of all the sources within a radius of 5° from the ROI and the isotropic and Galactic diffuse emission templates were left to vary. We derived an upper limit on gamma-ray flux of M81* as 2.58×10^{-13} ergs cm^{-2} s^{-1} over 10-300 GeV energy range.

4.3 Long-term X-ray Light Curve

We construct a long-term light curve by plotting the absorption-corrected soft (0.5 - 2 keV) and hard (2.0-10.0 keV) X-ray flux and optical and UV flux with the date of observations in Figure 4.1.

4.3.1 Identification of Flares

We use the Bayesian Block algorithm to identify statistically significant X-ray flares in the light curve (Scargle et al. 2013). The algorithm finds the optimally spaced time intervals by considering the statistical fluctuations from the flux measurement errors. We use the `astropy` implementation of the Bayesian Block algorithm with a false-positive rate of 0.01 with the option of “measures” in the fitness function. The change in flux states, as obtained by the Bayesian Block algorithm, is represented by a magenta line in Figure 4.1. The height of each block represents the statistical mean of all the flux measurements within that block. We define the statistical mean of all the flux measurements as the base (or quiescent) flux. If the mean flux value in a block exceeds the base value by a factor of $n\sigma$, we consider it as a flare, where n is an integer and σ is the standard deviation. By this definition, we

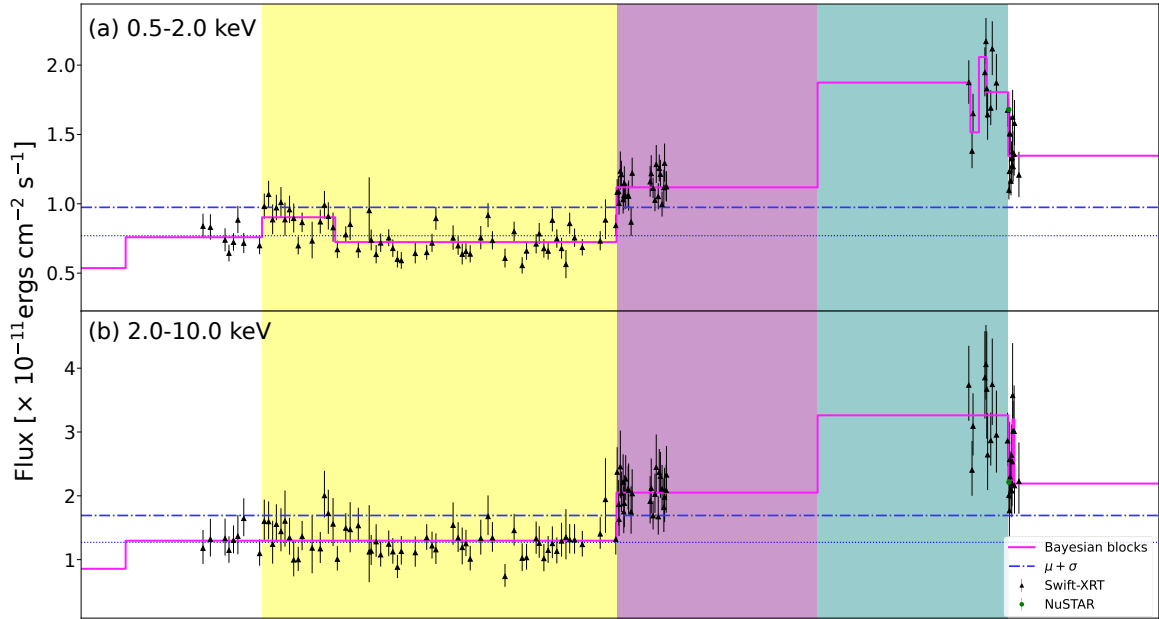


Figure 4.2: Same as Figures 4.1(a) and (b), zoomed in to the region of Flare B and Flare C to show the change in flux.

identify two flares, Flare B and Flare C, seen in both soft and hard X-ray energies, as shown in Figures 4.1 and 4.2. Flare A flux exceeds the base flux value by only 0.8σ (indicated by the red line in Figure 4.1) and thus is not statistically significant. However, for a comparative study, we also consider Flare A since it was identified as an X-ray flare preceding a radio rebrightening that followed the largest radio flare observed for M81* by King et al. (2016). The corresponding flux in the higher energy range is close to the baseline flux, consistent with no flare seen in this band by King et al. (2016), as well.

4.3.2 Identification of Quiescent State Period

We select the period of MJD 56467.7- MJD 56796.7 for the quiescent state (shown in yellow in Figures 4.1 and 4.2). The flux in this period is close to the mean average flux over the entire period of the light curve. Also, the response matrix files of the observations of this period are the same, thus eliminating the need to sum different response files.

4.4 Multi-wavelength Spectral Energy Distributions

4.4.1 Construction of Spectral Energy Distributions for Different States

In Figure 4.3, we zoom in to the period over which rebrightening of M81* was observed in the radio band in 2011 (King et al. 2016). Though an increase in flux in the soft X-ray band is seen, it is not statistically significant, as discussed in Section 4.3.1. However, we consider this period as Flare A to estimate the jet parameters, electron distribution, and evolution with time during knot ejection. The green dashed lines represent the four epochs over which radio observations were recorded by King et al. (2016). Our paper refers to them as Epochs 1, 2, 3, and 4, respectively. Since Epoch 1 lies within the flaring period of Flare A, we include this to construct a quasi-simultaneous SED for Flare A. Similarly, simultaneous and quasi-simultaneous SEDs are constructed for Epochs 2, 3, and 4.

To construct a SED for Epoch 2, we have taken the Swift observation recorded on the same day (2011 September 21). We constructed SED with only radio measurements for Epoch 3 (2011 September 27) due to Swift's lack of observation. For Epoch 4 (2011 October 4), the Swift observation recorded on 2011 October 3 was used to construct the SED.

We constrain the emission in the gamma-ray band with the upper limit on gamma-ray flux from M81* (Section 4.2.3). The compilation of multi-wavelength data for the different epochs and flares is shown in Figure 4.4, which includes both archival data and the data analyzed in the present work (shown in color).

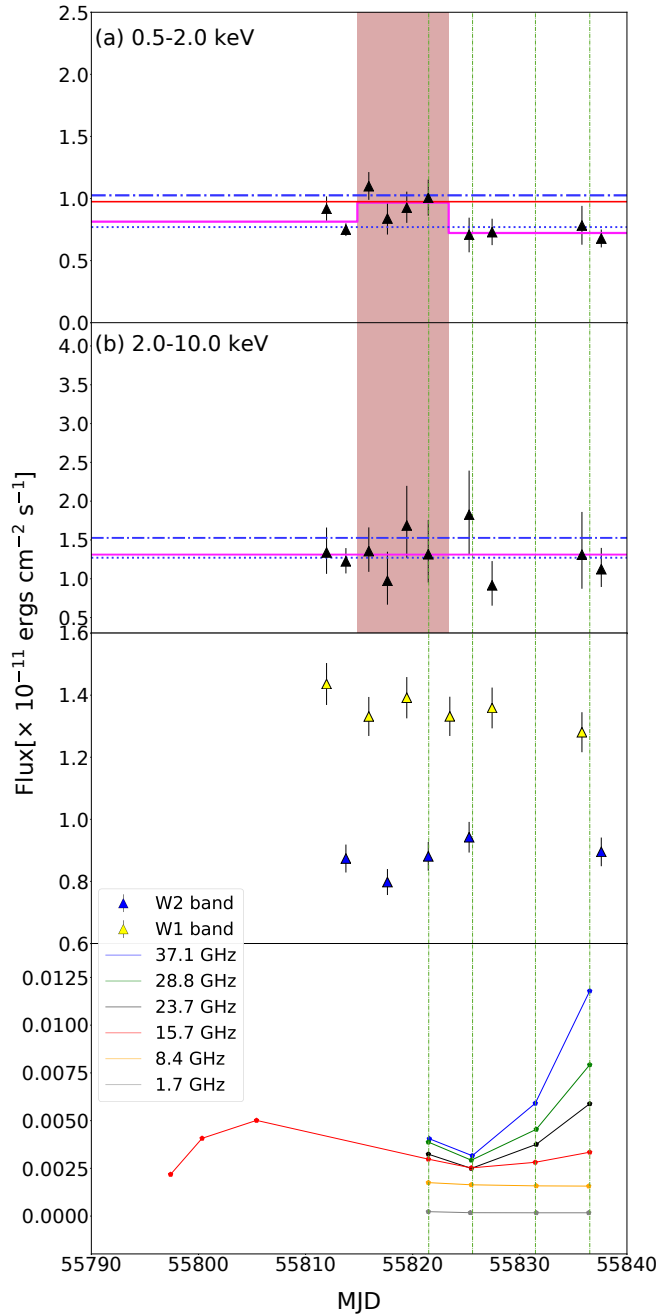


Figure 4.3: The lightcurve during the period considered at the time of knot ejection (King et al. 2016). The measurements in radio are taken from the same work. The black data points are Swift measurements. The magenta line in Panels (a) and (b), represent the Bayesian blocks, as in Figure 4.1. The blue dotted line is the mean flux over the entire period of 16 yr that we have considered in our study. The red line in panel (a) is the mean flux plus 0.8σ , which represents the peak flux of the X-ray flare associated with the knot ejection, while the blue dotted-dashed line represents 1σ over the mean flux. The vertical dotted-dashed lines represent the four epochs: 2011, September 17, September 21, September 27, and October 4, in the same order. For Flare A, we consider the radio data taken at Epoch 1 (2011 September 17) as it lies within the flare period for a simultaneous radio to X-ray SED. We also construct the SEDs for Epochs 2, 3, and 4 when quasi-simultaneous single-epoch X-ray measurements are available.

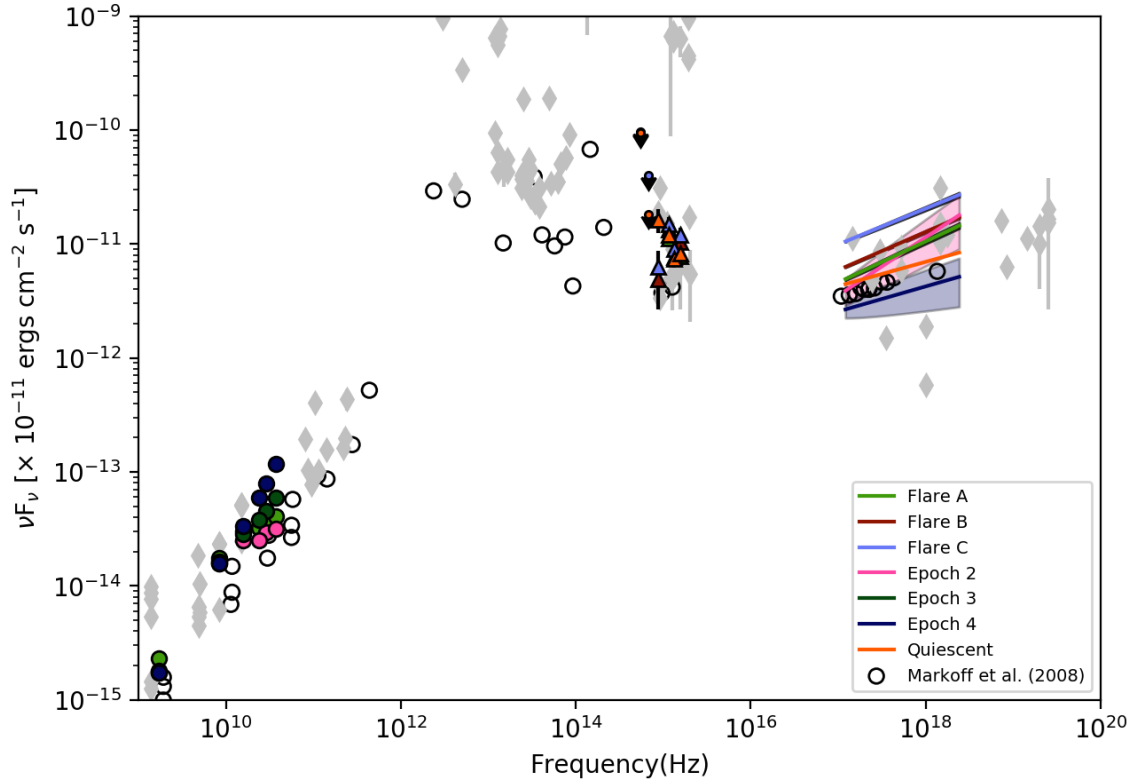


Figure 4.4: The multi-wavelength data of M81* at different epochs and flaring periods are shown in color. In the X-ray band, the power law component of the X-ray spectrum obtained in these different states has been shown, with the shaded region representing the errors at 90% confidence level (2.706σ). The simultaneous multi-wavelength data from Markoff et al. (2004) at a quiescent period are also shown by open circles for reference. The gray diamonds are the archival data obtained from the NASA/IPAC Extragalactic Database (NED), shown here as a secondary constraint for modeling at the frequencies where the simultaneous/quasi-simultaneous data are unavailable.

4.4.2 Modeling of Spectral Energy Distributions

We model the compiled broadband SEDs in different states using the time-dependent code GAMERA to investigate the evolution of the broadband spectrum, in particular, the X-ray spectrum (for modeling details, see Section 2.3). We consider a homogeneous and spherical emission region (blob) of radius R having the magnetic field B and moving along the jet with a bulk Lorentz factor Γ . This region contains relativistic electrons with a power law distribution of particles and emits radiation through synchrotron and SSC processes.

Using this code, we calculate the particle spectrum $N = N(E, t)$ under the con-

tinuous injection of the particles described by $Q(E, t)$ and energy loss rate $b = b(E, t)$. The code solves the transport equation given by Equation 2.18 with Q independent of time; that is, continuous uniform injection is assumed. The code subsequently calculates the synchrotron and SSC emission, which are Doppler boosted by a factor of δ^4 in the observer's frame due to relativistic beaming, where $\delta = [\Gamma(1 - \beta \cos \theta)]^{-1}$ is the Doppler factor, Γ is the bulk Lorentz factor of the emission region or the jet frame, β is the intrinsic speed of the emitting plasma, and θ is the viewing angle of the jet with respect to the line of sight of the observer.

For modeling, we consider a quiescent state as the time the system attains a steady state, i.e., $N(E, t)$ no longer evolves with time. For Epochs 2, 3, and 4, the time over which the electron spectrum evolves is constrained by the number of days between each epoch. For each flare, we allow $N(E, t)$ to evolve over the period of the respective flare obtained with the Bayesian block method. For all the SEDs, the Lorentz bulk factor has been kept at a fixed value of 3.7 (Doi et al. 2013). We vary the parameters that define the injected electron distribution, e.g., the spectral index, the minimum Lorentz factor (Γ_{min}), the maximum Lorentz factor (Γ_{max}), and the normalization factor (A), and also the parameters of the emission region e.g., the radius of the emission region (R) and the magnetic field (B) in that region to fit the data. Here, the primed quantities denote the parameters in the comoving frame of the emission region in the jet, and the unprimed quantities are the values of the parameters measured in the observer's frame. The energy density of the injected electrons is $U'_{e,inj}$ in the comoving frame, and the jet power in the injected electrons, $P_{e,inj}$, is calculated with the following expression:

$$P_{e,inj} = \pi R^2 \Gamma^2 c U'_{e,inj} = \frac{3\Gamma^2 c}{4R} \int_{E_{min}}^{E_{max}} EQ(E) dE \quad (4.1)$$

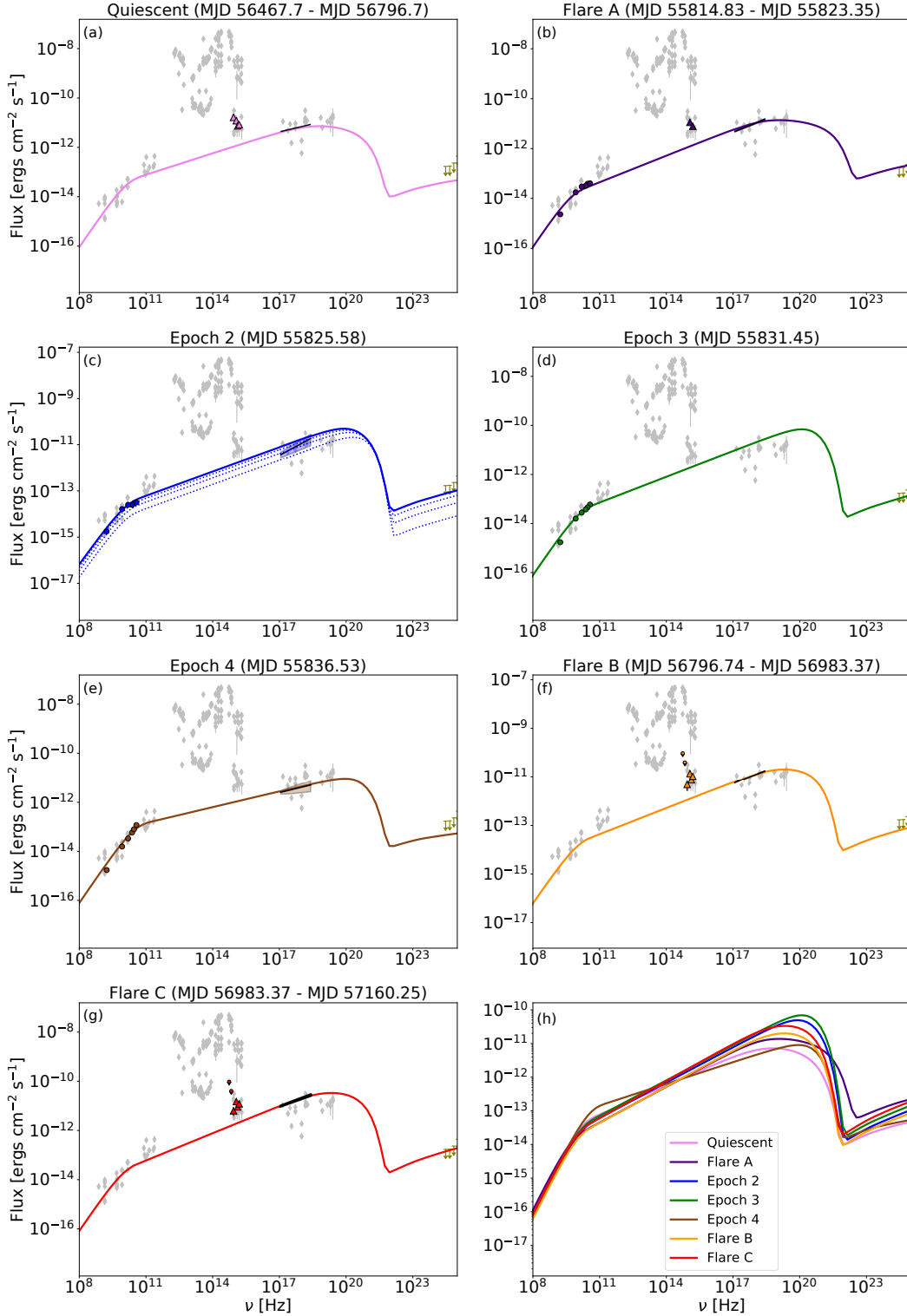


Figure 4.5: One-zone SED modeling of M81* during different states. Panel (c): the dotted curves in the modeling represent the evolution of SED from the initial time of injected electrons to the final age of the system, which explains the emission at this epoch. Panels (a)-(g): X-ray data for different states are black. The upper limits obtained using Fermi-LAT data are shown in olive to constrain the SSC component and, thus, the size of the emission region. Panel (h): Simulated SEDs for all the states and epochs plotted together to show their spectral shape and flux variations.

4.5 Results

We identify three flares (Flare A, B, and C) in the soft X-ray band, as shown in Figure 4.1. A flare is observed in the high X-ray band for both Flare B and Flare C but not for Flare A. In Figures 4.1(c) and (d), we show the flux in optical and UV bands as obtained by Swift-UVOT. The flux in UV and optical bands is also found to be increased during Flare B and Flare C. This flux is corrected for Galactic extinction and host-galaxy contribution. Therefore, the rise in flux in these bands during Flare B and C indicates variability in M81*.

Interestingly, the X-ray flux significantly varies at different time intervals (Figure 4.4). Using time-dependent SED modeling, the evolution of the jet parameters has been studied in each state.

By modeling the SED during the quiescent state (2013 June 24 - 2014 May 19), we find that the radio-to-X-ray emission can be explained by one-zone synchrotron emission, which extends up to 10^{20} Hz, while the SSC emission is well below the upper limits that we have obtained by Fermi-LAT in the gamma-ray energy band from 10 to 300 GeV. The system attains a steady state after 200 days. It is noted that the hard spectrum of X-rays in the quiescent state requires a hard injected electron spectrum with spectral index $p=2.42$ (Figure 4.5(a)). The size of the emitting region is 0.029 pc, and the system is found to be particle dominated with $U'_B/U'_e \approx 0.017$, two orders of magnitude away from the equipartition of energy in the jet. The jet parameter values used for our SED modeling are shown in Table 4.1. The total jet power during the quiescent state is 8.84×10^{41} ergs s^{-1} , while it shows slight variation during the other epochs and flares.

Subsequently, we perform the SED modeling for all the other states, as shown in Figure 4.5(a)-(g). Synchrotron emission can explain the radio to X-ray data for

all the epochs and flares. All the SEDs simulated from our model are presented in Figure 4.5(h) to show the variation in spectral shape and flux during the different states of M81*.

During Flare A, the X-ray spectrum hardens, which is explained by the hardening in the injected electron distribution. After 4 days, at Epoch 2, the radio spectrum has softened (as also seen in Figure 4.3), and the X-ray spectrum with similar flux has hardened. A change in injected electron energy density explains this. Six days later, on 2011 September 27, at Epoch 3, the radio spectrum became harder. Due to the lack of X-ray data at this epoch, we have fitted the radio spectrum with synchrotron emission using a parameter set similar to Epoch 2. It is found that the injected electron density is again increased to accommodate the radio data at this epoch. Eight days later, at Epoch 4, the X-ray spectrum is found to be softer than that at Epoch 2. Interestingly, while the X-ray flux at this epoch is lower than that of the quiescent state, the radio flux becomes the maximum at this epoch (see Figure 4.3). The spectral index of the injected electron distribution required to explain the emission is the maximum at this epoch. Further, the injected electron density at this epoch is maximum. Flare B (2014 May 19-2014 November 22) and Flare C (2014 November 22 - 2015 May 18) show flaring in both soft and hard X-ray bands. The values of the radius of the emission region (R) during Flare B and Flare C are the same as that during the quiescent state, and the magnetic field has been kept fixed at 0.003 Gauss while the injected electron spectrum becomes harder. Epoch 4 requires the highest injected electron density among all the states, as shown in Table 4.1. At all the epochs and states, the power in electrons has the highest contribution to the total jet luminosity.

The Swift UV-Optical data points can be explained as multi-blackbody thermal emission from the disc (Markoff et al. 2004, Lucchini et al. 2019).

| Parameter | Quiescent State | Flare A | Epoch 2 | Epoch 3 | Epoch 4 | Flare B | Flare C |
|--------------------------------------|------------------------|------------------------|------------------------|------------------------|------------------------|------------------------|------------------------|
| Spectral index | 2.42 | 2.3 | 2.3 | 2.3 | 2.57 | 2.26 | 2.26 |
| Γ_{min} | 400 | 400 | 400 | 400 | 580 | 400 | 400 |
| Γ_{max} | 1.5×10^8 | 1.5×10^8 | 1.5×10^8 | 1.5×10^8 | 1.5×10^8 | 1.5×10^8 | 1.5×10^8 |
| R [cm] | $9. \times 10^{16}$ | $9. \times 10^{16}$ | $9. \times 10^{16}$ | 9.0×10^{16} | 9.0×10^{16} | 9.0×10^{16} | 9.0×10^{16} |
| B [Gauss] | 0.004 | 0.004 | 0.004 | 0.004 | 0.004 | 0.003 | 0.003 |
| Doppler factor | 4.1 | 4.1 | 4.1 | 4.1 | 4.1 | 4.1 | 4.1 |
| Bulk Γ | 3.7 | 3.7 | 3.7 | 3.7 | 3.7 | 3.7 | 3.7 |
| $U'_{e,inj}$ [erg cm ⁻³] | 1.19×10^{-11} | 1.57×10^{-11} | 4.20×10^{-11} | 7.70×10^{-11} | 1.17×10^{-10} | 1.21×10^{-11} | 1.98×10^{-11} |
| $P_{e,inj}$ [erg s ⁻¹] | 1.25×10^{35} | 1.64×10^{35} | 4.39×10^{35} | 8.06×10^{35} | 1.64×10^{36} | 1.27×10^{35} | 2.07×10^{35} |
| U'_B/U'_e | 0.017 | 0.027 | 0.020 | 0.017 | 0.014 | 0.008 | 0.007 |

Table 4.1: Parameters obtained from modeling the SEDs of M81* in different states. Note, the $U'_{e,inj}$ and U'_B are the energy densities in electrons and magnetic field in the jet frame, and $P_{e,inj}$ is the jet power in injected electrons. The escape time for each case is taken to be R/c .

The variation of parameter values in the different states obtained from the X-ray data analysis (top two panels) and SED modeling is shown in Figure 4.6.

4.6 Discussion

Our time-dependent modeling of SEDs shows that the radio-to-X-ray emission observed from M81* can be well explained by synchrotron emission from the jet in all the states (quiescent to high X-ray flux states) and the epochs of radio knot emission.

4.6.1 Comparison with High-Synchrotron Peaked Blazars

The synchrotron emission peaks at 8.2×10^{18} Hz in the quiescent state of M81*, which is similar to extreme HSPs where the radio to X-ray data is explained with the synchrotron emission of relativistic electrons, with the peak frequencies higher than 10^{17} Hz (Costamante et al. 2001, Costamante et al. 2018). For HSPs, e.g. 1ES 1959+650 (Chandra et al. 2021), 1ES 1218+304 (Sahakyan 2020), and Mrk 501 (Singh et al. 2019), it has been noted that the synchrotron peak frequencies, ν_{syn} , can reach frequencies higher than 10^{17} Hz, at least in the flaring states, showing extreme high-synchrotron-peaked behavior. We observe a similar behavior during

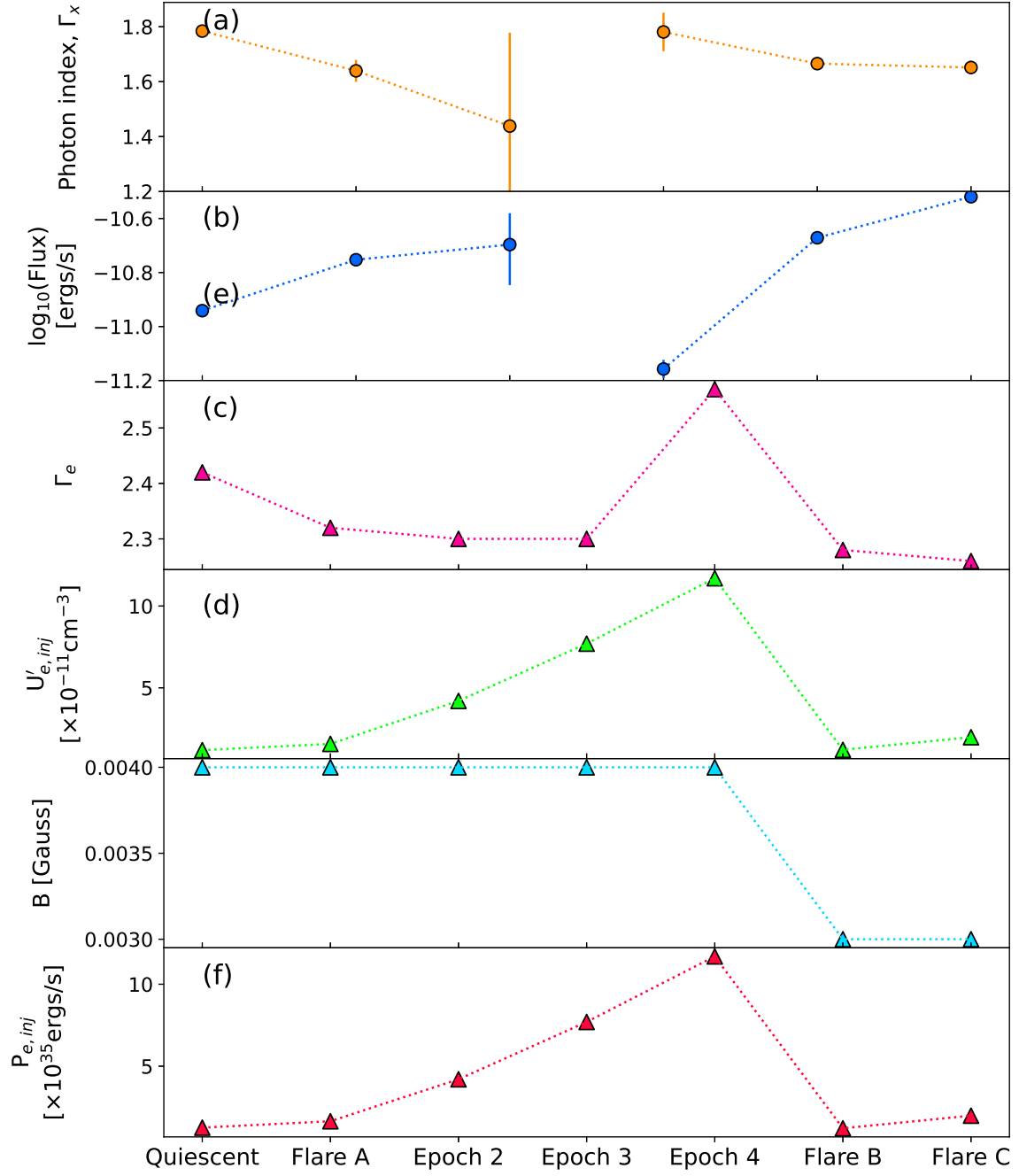


Figure 4.6: Time evolution of observables, (a) X-ray photon index, Γ_x , and (b) soft X-ray flux, and the parameters obtained from modeling, (c) injected electron spectral index, (d) energy density of injected electrons, (e) the magnetic field in the emission region, and (f) the jet power in injected electrons. We do not have any quasi-simultaneous X-ray data for Epoch 3, so there is a break in the connected dot plot in the top two panels

the X-ray flares of M81*. The synchrotron peak shifts to higher frequencies with the increase in the amplitude of the X-ray flux, with the maximum value of ν_{peak} reaching up to 3.32×10^{19} Hz during Flare C.

4.6.2 Photon Index during Flares

A harder-when-brighter behavior is commonly seen during X-ray flares of blazars, which manifests itself as a decrease in photon index with increasing flux (Xue et al. 2006). Figures 4.6(a) and (b) suggest a similar behavior in M81*. Our modeling shows that the spectral index of the injected electron distribution must be decreased with increasing X-ray flux (Figure 4.6(c)).

4.6.3 Magnetic Field during Flares

The magnetic field required to fit the SEDs of M81* during all states is of the order of milliGauss, which is two orders of magnitude lower than the magnetic field required to fit the quiescent states of other LLAGNs detected in gamma rays (see Tomar et al. 2021). However, in those cases, the X-ray data were fitted with SSC emission except for M87, where the synchrotron emission covered the X-ray data. The magnetic field required to explain the synchrotron emission from HSP Mrk 501 during its high activity state in X-rays is of the order of 0.1 Gauss (MAGIC Collaboration et al. 2020d) in the single zone leptonic model, which is similar to the magnetic field used in the modeling of several LLAGNs (Tomar et al. 2021) in the quiescent state. Ten extreme high-frequency peaked BL Lacs (Acciari et al. 2020), which include 1ES 2037+521, TXS 0210+515, BZB 080+3455, TXS 0637-128, and six other sources were modeled with a single-zone conical-jet model. The magnetic field required to explain their X-ray data with synchrotron emission of leptons varies from 0.02 to 0.25 G, comparable to Mrk 501 and higher than M81*.

4.6.4 Role of Doppler Boosting in Flaring

In the present work, the value of the Doppler factor 4.1 has been adapted from Doi et al. (2013), which is much lower than the typical value of the Doppler factor of the orders of tens observed in blazars. In other LLAGNs, the values of the Doppler factor are found to be 1.6 for NGC 315, 1 for NGC 4261, 2.3 for NGC 1275, and 2.3 for M87 (Tomar et al. 2021), which are comparable to that of M81*.

Mrk 501 is at a distance of 140 Mpc, and M81* is only at a distance of 3.4 Mpc from us. If we compare their X-ray fluxes, during the quiescent state, the X-ray flux of Mrk 501 is a few times 10^{-10} erg cm $^{-2}$ sec $^{-1}$ (see Figure 1 of MAGIC Collaboration et al. (2020d) and Figure 1 of Ahnen et al. 2017), whereas the X-ray flux M81* is about 10^{-11} erg cm $^{-2}$ sec $^{-1}$. During the flaring state, the X-ray and gamma-ray flux becomes a factor of 2 or higher than the flux in the quiescent state in the case of Mrk 501. Still, in the case of M81*, a factor of 2 variations in X-ray flux is observed only during Flare C (which is the only X-ray flare with a significance of more than 3σ). During flares, the X-ray and gamma-ray flux of the blazars may become much higher compared to the same during their quiescent state, as happened during the intense TeV flare of 1ES 1959+650 in 2016 (MAGIC Collaboration et al. 2020a). In Figure 4.7, we compare the SED of 1ES 1959+650 with that of M81* during quiescent and flaring states. The unusually high gamma-ray flux has been explained by a small emission region and a high value of Doppler factor in the range of 40 to 60.

It is important to mention here that the value of the Doppler factor plays an important role in producing higher flux and higher variability in flux in blazars. Due to high values of the Doppler factor, a higher flux of photons is expected from blazars in all energy bands compared to LLAGNs as the flux is Doppler boosted by a factor of δ^4 in the observer's frame. Moreover, as a result of high values of the Doppler factor, the increase in flux during flaring states with respect to the

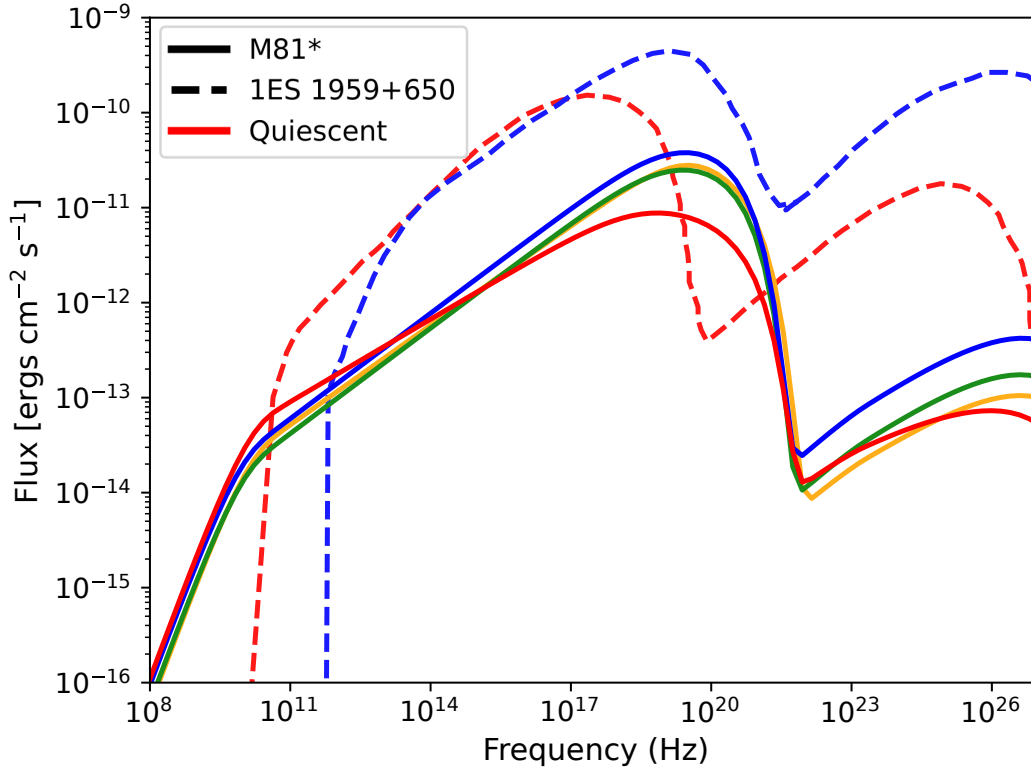


Figure 4.7: SED of blazar 1ES 1959+650 obtained using a one-zone SSC model during quiescent state (red dashed line; reproduced from Tagliaferri et al. 2008) and flaring state (blue dashed line; reproduced from MAGIC Collaboration et al. 2020a) compared with that of M81* during quiescent state (red solid line) and flaring states (blue, green, and yellow solid lines).

quiescent state is higher compared to LLAGNs.

4.6.5 Other Parameters during Flares

In the long-term X-ray light curve of M81*, the variation in the X-ray flux is within a factor of 2 of the quiescent state flux. As a result, we do not report any large variation in the injected power of electrons during Flare A, Flare B, and Flare C when the magnetic field is nearly constant. During Epochs 2, 3, and 4, the rise in the radio flux requires considerably higher power in injected electrons compared to the quiescent state.

Figure 4.6 shows how the values of two of the observables (X-ray photon index,

(Γ_x) and flux) and our model parameters (electron spectral index at injection, (Γ_e), the energy density in injected electrons in the comoving frame ($U'_{e,inj}$), magnetic field (B), and jet power in injected electrons, ($P_{e,inj}$) change in different states of M81* that we have considered in our study.

A hard-injected electron spectrum is required to explain the hardness in the X-ray spectrum, which is observed during Flare B and Flare C. At the other epochs, injected electron spectrum evolution is also found to be in accordance with the evolution of the X-ray spectrum. The jet remains dominated by particles during all the states, and equipartition in energy is not maintained.

The X-ray flux increases during the flares, but the shape of the SED does not change significantly from the quiescent state. The synchrotron peak flux increases and the peak shifts slightly towards higher energy in the flaring states. The injected jet power in electrons increases with increasing X-ray flux during flares. While the X-ray flux is lower at Epoch 4 than the quiescent state, the jet power is the highest at this epoch. This could be attributed to the increase in radio emissions.

LLAGNs are interesting sites for studying cosmic ray acceleration, multi-wavelength flares, the time evolution of particle spectrum, and jet parameters. We conclude from the SED modeling of the different states and epochs of M81* that the synchrotron emission from the one-zone model can explain the radio to X-ray emission from M81*. Detection of gamma rays can help to constrain the model better. Low values of Lorentz bulk factor, magnetic field, and jet power in electrons compared to those of the high luminosity AGNs are common features of LLAGNs. With more observations on the spectral and temporal evolution of LLAGNs, it would be possible to confirm whether the jet activities of LLAGNs and high-luminosity AGNs are similar.

Curiouser and curiouser!

-Alice (Alice in Wonderland)

5

Conclusions

In this thesis, two intertwined studies (Tomar et al. 2021, Tomar & Gupta 2023) were conducted to understand LLAGN jets better. We presented construction and detailed analysis of the SEDs of LLAGNs, focusing on the non-thermal multi-wavelength emission properties of the jet.

In Tomar et al. (2021), the multi-wavelength SEDs of four LLAGNs with gamma-ray detection (NGC 315, NGC 4261, NGC 1275, and NGC 4486) were modeled using a leptonic model. The study demonstrated that synchrotron self-Compton (SSC) emission from subparsec-scale jets could explain the observed broadband SEDs. However, for higher energy gamma-ray emissions (above a few GeV) observed in

NGC 315 and NGC 4261, an additional external inverse-Compton (IC) component from kilo-parsec scale jets was necessary, where the stars of the host galaxy provided the dominant photon field. This work highlighted the role of kiloparsec scale jets in modeling the emission from LLAGNs, similar to those in more luminous AGNs. Thus suggesting more similarities across the scale (Schwartz et al. 2020, Zacharias & Wagner 2016, Breiding et al. 2023).

Tomar & Gupta (2023) expanded on the crucial observation of the ejection of a discrete knot in an LLAGN M81* by examining its jet parameters' SEDs and time evolution. Since jets in LLAGNs are expected to be continuous, the detection of discrete knots motivates us to constrain the properties of the jets, the production and emission mechanism for which is hinted to be more similar to luminous AGNs than previously thought.

This study revealed that the synchrotron emission from a one-zone SSC model could adequately explain the radio to X-ray emissions during the quiescent, flaring states and other epochs during the knot ejection. Additionally, it was found that the LLAGN with no confirmed gamma-ray detection showed harder-when-brighter behavior similar to blazars, which are strong gamma-ray emitters, highlighting the role of Doppler boosting in the latter. The behavior in the case of M81* can be understood as a low Doppler-boosted version of high-synchrotron peaked blazars (as shown in Figure 4.7).

Both studies underline the similarities in jet emission mechanisms in LLAGNs and luminous AGNs. They also show the significance of LLAGNs as high-energy particle acceleration sites and their non-negligible contributions to the high-energy multi-wavelength sky. The detailed modeling of the SEDs provides a comprehensive understanding of the underlying physical processes in the jets of these systems, particularly the role of synchrotron and inverse Compton scattering mech-

anisms.

5.1 Future Outlook

While significant progress has been made in understanding the emission mechanisms and jet dynamics of LLAGNs, the field remains ripe with opportunities for further discoveries and advancements. Integrating new observational techniques, theoretical models, and multi-messenger data will undoubtedly lead to a significantly more comprehensive understanding of these fascinating cosmic objects and their role in the multi-messenger sky, which has begun to light up well.

Cherenkov Telescope Array (CTA; [CTA Consortium & Ong 2019](#)) is a promising future ground-based gamma-ray detector with greatly improved sensitivity to the gamma-ray sky. Our research ([Tomar et al. 2021](#)) has demonstrated the presence of high Lorentz factor electrons within kiloparsec-scale jets of low-luminosity active galactic nuclei (LLAGNs), identifying these jets as pivotal targets for CTA. To further explore this, we plan to examine LLAGNs listed in the XJETS database, which catalogs extragalactic jets emitting in X-rays. By assessing their potential for gamma-ray emission using the framework developed in [Tomar et al. \(2021\)](#), we aim to refine predictions for gamma-ray observatories and enhance our understanding of high-energy processes in these jets.

The recent detection of VHE gamma-ray emissions associated with the low-luminosity AGN NGC 4278 by LHAASO ([Cao et al. 2024a](#)) suggests that even these less dynamic systems can host regions of extreme particle acceleration. Further, the behavior of VHE gamma rays is similar to those observed in blazars ([Cao et al. 2024b](#)). Multi-wavelength studies proposed for NGC 4278 suggest these high-energy emissions originate from regions near the black hole ([Dutta & Gupta 2024](#)).

Moreover, the identification of the blazar TXS 0506+056 as a neutrino source by

IceCube (IceCube Collaboration et al. 2018a) provides direct evidence that blazars can accelerate hadrons to high energies, leading to neutrino production through hadronic processes. This discovery is crucial as it links AGNs, particularly blazars, with high-energy neutrino production. Additionally, our study (Tomar & Gupta 2023) found that the behavior of M81*, a low-luminosity AGN, is similar to that of high-synchrotron peaked blazars, suggesting that even if gamma-rays are not detected or are faint in some LLAGNs, these galaxies might still effectively accelerate particles and potentially produce neutrinos. This observation, coupled with evidence of gamma-ray emissions from various scales of jets in LLAGNs, supports further investigation into whether LLAGNs could also be significant sources of neutrinos and cosmic rays akin to blazars (Zacharias & Wagner 2016, Pratim Basumallick & Gupta 2017, Sahu et al. 2021)

Polarimetric studies using the Imaging X-ray Polarimetry Explorer (IXPE) have already provided key insights into the acceleration mechanisms of these emissions and magnetic field configurations (Marin et al. 2023, MAGIC Collaboration et al. 2024). Further insights are expected from the X-ray Polarimetry Satellite (XPoSat)¹. These investigations can help us remove degeneracies between different leptonic and hadronic emission models, which are critical for deciphering the particle processes in these environments (Zhang & Böttcher 2013, Tavecchio et al. 2018). Moreover, M81* spectra and variability are found to be similar to high-synchrotron peaked blazars in our work (Tomar & Gupta 2023). Correlating polarimetric data with observations across radio, optical, X-ray, and gamma-ray frequencies of M81* can help confirm if the jet properties of M81* mirror those of high-synchrotron-peaked blazars (HBLs), strengthening the idea that these different types of active galactic nuclei (AGNs) may share similar jet behaviors and

¹Details at <https://www.isro.gov.in/XPoSat.html>.

physical conditions but perhaps scaled-down.

Another key to understanding particle acceleration in these jets is the connection between radio knots/components in AGN jets and high-energy emissions. These regions are often sites of shocks or turbulence, where high-energy electrons upscatter photons via the inverse Compton process, emitting gamma rays. Temporal correlations between radio flares and high-energy emissions, supported by multi-wavelength observations, indicate a common origin in these acceleration zones. Detailed SED modeling, such as in LLAGN M81* (Tomar & Gupta 2023), shows that SSC emission from radio knots can explain broadband emissions. Studying this correlation in a larger sample will enhance our understanding of acceleration sites and mechanisms.

Much information about the relativistic jets is still unknown, including their launching, emission mechanisms, and particle composition. The comparative study in this thesis can be expanded to include more LLAGNs, thereby providing a larger sample of jet properties on accretion efficiency scales. The sample of studied LLAGNs could be expanded by identifying and analyzing new candidates to provide a broader statistical basis for understanding these objects. Future surveys and missions, such as the eROSITA X-ray telescope (Predehl et al. 2021), will be instrumental in discovering and characterizing new LLAGNs.

In a nutshell, we aim to unravel the role of LLAGNs in the very-high-energy sky by addressing the following key questions in the future:

- How are radio knots/components connected to high-energy emissions in AGN jets?
- What does the variability in LLAGN central engines tell us about their behavior compared to more luminous AGNs?

- Are LLAGNs among the most efficient sites for particle acceleration near us?
- Is the jet production and emission mechanism in LLAGNs and their luminous counterparts similar?
- Do LLAGNs accelerate high-energy and ultra-high-energy cosmic rays, including heavy nuclei, which dominate at the highest energies?
- Could LLAGNs also be potential sources of neutrinos, similar to blazars?

Exploring these questions will help us piece together the broader role of LLAGNs in cosmic high-energy phenomena.

To Infinity and Beyond.

Buzz Lightyear (Toy Story)



XRT Pile-up Correction

Pile-up correction ¹ in Swift's XRT data involves identifying the pile-up by checking count rates, which should be below 0.5 counts per second. If pile-up is detected, an annular extraction region is used to exclude the central, piled-up area. The central area is determined involves modeling the point spread function (PSF) using a combination of a King function and a Gaussian component. The PSF is given by:

$$\text{PSF}(r) = W \exp\left(-\frac{r^2}{2\sigma^2}\right) + (1 - W) \left[1 + \left(\frac{r}{r_c}\right)^2\right]^{-\beta}$$

For Swift PC mode, $W \approx 0.075$, $\sigma \approx 7.42$ arcseconds, $r_c \approx 3.72$ arcseconds, and

¹More details at <https://www.swift.ac.uk/analysis/xrt/pileup.php>

$\beta \approx 1.31$. The values of σ and r_c are in arcseconds, with 1 pixel equivalent to 2.357 arcseconds.

Pile-up distorts the PSF center, reducing the count relative to the King function, while the wings fit the King+Gaussian model. To correct for pile-up, fit the PSF model to the outer wings and extrapolate inward to determine the divergence point, which should be excluded when extracting spectra or light curves. The pile-up limit is typically a count rate above 0.5 counts per second.

B

Errors in Swift-UVOT Fluxes

The error in the six filters of UVOT is calculated as follows, following the standard propagation of errors.

Count rates, C are obtained from the intrinsic magnitude, m_o using

$$m_o = Z_{pt} - 2.5 \log_{10}(C) \quad (\text{B.1})$$

Here, Z_{pt} is the zero point value. Flux from the count rate is then calculated

using the Conversion factor, Cf as follows

$$F[\text{ergs/s/cm}^2/\text{\AA}] = C \times Cf \quad (\text{B.2})$$

Error on each flux value is calculated using standard error propagation, as follows:

$$f = f(x, y, z)$$

$$\sigma_f^2 = \left(\frac{df}{dx}\right)^2 \sigma_x^2 + \left(\frac{df}{dy}\right)^2 \sigma_y^2 + \left(\frac{df}{dz}\right)^2 \sigma_z^2$$

$$\sigma_{m_o} = \sigma_m$$

$$C = 10^{\frac{Z_{pt}-m_o}{2.5}}$$

$$\ln C = \frac{Z - m_o}{2.5} \ln 10$$

$$\frac{dC}{dZ} = \frac{\ln 10}{2.5} C$$

$$\frac{dC}{dm_o} = -\frac{\ln 10}{2.5} C$$

$$\sigma_C^2 = \left(\frac{dC}{dZ}\right)^2 \sigma_z^2 + \left(\frac{dC}{dm_o}\right)^2 \sigma_{m_o}^2$$

$$\sigma_F^2 = \left(\frac{dF}{dcf}\right)^2 \sigma_{cf}^2 + \left(\frac{dF}{dC}\right)^2 \sigma_C^2$$

$$\sigma_F^2 = C^2 \sigma_{cf}^2 + cf^2 \sigma_C^2$$

$$\sigma_F^2 = C^2 \sigma_{cf}^2 + cf^2 \left(\left(\frac{dC}{dZ}\right)^2 \sigma_z^2 + \left(\frac{dC}{dm_o}\right)^2 \sigma_{m_o}^2 \right)$$

$$\sigma_F^2 = C^2 \left(\sigma_{cf}^2 + \left(\frac{\ln 10 \cdot cf}{2.5}\right)^2 (\sigma_z^2 + \sigma_{m_o}^2) \right)$$

References

- Abbott, B. P., Abbott, R., Abbott, T. D., et al. 2017, Multi-messenger Observations of a Binary Neutron Star Merger, *The Astrophysical Journal Letters*, 848, L12, doi: [10.3847/2041-8213/aa91c9](https://doi.org/10.3847/2041-8213/aa91c9)
- Abdo, A. A., Ackermann, M., Ajello, M., et al. 2009a, Fermi Discovery of Gamma-ray Emission from NGC 1275, *The Astrophysical Journal*, 699, 31, doi: [10.1088/0004-637x/699/1/31](https://doi.org/10.1088/0004-637x/699/1/31)
- Abdo, A. A., Ackermann, M., Ajello, M., et al. 2009b, Fermi Large Area Telescope Gamma-Ray Detection of the Radio Galaxy M87, *The Astrophysical Journal*, 707, 55, doi: [10.1088/0004-637x/707/1/55](https://doi.org/10.1088/0004-637x/707/1/55)
- Abdo, A. A., Ackermann, M., Agudo, I., et al. 2010a, The Spectral Energy Distribution of Fermi Bright Blazars, *The Astrophysical Journal*, 716, 30, doi: [10.1088/0004-637x/716/1/30](https://doi.org/10.1088/0004-637x/716/1/30)
- Abdo, A. A., Ackermann, M., Ajello, M., et al. 2010b, Observations of the Large Magellanic Cloud with Fermi, *Astronomy & Astrophysics*, 512, A7, doi: [10.1051/0004-6361/200913474](https://doi.org/10.1051/0004-6361/200913474)
- Abdo, A. A., Ackermann, M., Ajello, M., et al. 2010c, Fermi Large Area Telescope View of the Core of the Radio Galaxy Centaurus A, *The Astrophysical Journal*, 719, 1433, doi: [10.1088/0004-637x/719/2/1433](https://doi.org/10.1088/0004-637x/719/2/1433)
- Abdollahi, S., Acero, F., Ackermann, M., et al. 2020, Fermi Large Area Telescope Fourth Source Catalog, *The Astrophysical Journal Supplement Series*, 247, 33, doi: [10.3847/1538-4365/ab6bcb](https://doi.org/10.3847/1538-4365/ab6bcb)
- Abramowicz, M. A., Czerny, B., Lasota, J. P., & Szuszkiewicz, E. 1988, Slim Accretion Disks, *The Astrophysical Journal*, 332, 646, doi: [10.1086/166683](https://doi.org/10.1086/166683)
- Acciari, V. A., Beilicke, M., Blaylock, G., et al. 2008, Observation of Gamma-Ray Emission from the Galaxy M87 above 250 GeV with VERITAS, *The Astrophysical Journal*, 679, 397, doi: [10.1086/587458](https://doi.org/10.1086/587458)
- Acciari, V. A., Aliu, E., Arlen, T., et al. 2009, Radio Imaging of the Very-High-Energy γ -Ray Emission Region in the Central Engine of a Radio Galaxy, *Science*, 325, 444, doi: [10.1126/science.1175406](https://doi.org/10.1126/science.1175406)

Acciari, V. A., Ansoldi, S., Antonelli, L. A., et al. 2020, New Hard-TeV Extreme Blazars Detected with the MAGIC Telescopes, *The Astrophysical Journal Supplement Series*, 247, 16, doi: [10.3847/1538-4365/ab5b98](https://doi.org/10.3847/1538-4365/ab5b98)

Acciari, V. A., Ansoldi, S., Antonelli, L. A., et al. 2021, First detection of VHE gamma-ray emission from TXS 1515-273, study of its X-ray variability and spectral energy distribution, *Monthly Notices of the Royal Astronomical Society*, 507, 1528, doi: [10.1093/mnras/stab1994](https://doi.org/10.1093/mnras/stab1994)

Acerro, F., Ackermann, M., Ajello, M., et al. 2015, Fermi Large Area Telescope Third Source Catalog, *The Astrophysical Journal Supplement Series*, 218, 23, doi: [10.1088/0067-0049/218/2/23](https://doi.org/10.1088/0067-0049/218/2/23)

Ackermann, M., Ajello, M., Albert, A., et al. 2012, The Fermi Large Area Telescope on Orbit: Event Classification, Instrument Response Functions, and Calibration, *The Astrophysical Journal Supplement Series*, 203, 4, doi: [10.1088/0067-0049/203/1/4](https://doi.org/10.1088/0067-0049/203/1/4)

Ackermann, M., Ajello, M., Allafort, A., et al. 2013, Detection of the Characteristic Pion-Decay Signature in Supernova Remnants, *Science*, 339, 807, doi: [10.1126/science.1231160](https://doi.org/10.1126/science.1231160)

Ackermann, M., Ajello, M., Albert, A., et al. 2014, Fermi establishes classical novae as a distinct class of gamma-ray sources, *Science*, 345, 554, doi: [10.1126/science.1253947](https://doi.org/10.1126/science.1253947)

Agudo, I., Thum, C., Gómez, J. L., & Wiesemeyer, H. 2014, A simultaneous 3.5 and 1.3 mm polarimetric survey of active galactic nuclei in the northern sky, *Astronomy & Astrophysics*, 566, A59, doi: [10.1051/0004-6361/201423366](https://doi.org/10.1051/0004-6361/201423366)

Aharonian, F., Akhperjanian, A., Beilicke, M., et al. 2003, Is the giant radio galaxy M 87 a TeV gamma-ray emitter?, *Astronomy & Astrophysics*, 403, L1, doi: [10.1051/0004-6361:20030372](https://doi.org/10.1051/0004-6361:20030372)

Aharonian, F., Akhperjanian, A. G., Bazer-Bachi, A. R., et al. 2006, Fast Variability of Tera-Electron Volt γ Rays from the Radio Galaxy M87, *Science*, 314, 1424, doi: [10.1126/science.1134408](https://doi.org/10.1126/science.1134408)

Ahnen, M. L., Ansoldi, S., Antonelli, L. A., et al. 2017, Multiband variability studies and novel broadband SED modeling of Mrk 501 in 2009, *Astronomy & Astrophysics*, 603, A31, doi: [10.1051/0004-6361/201629540](https://doi.org/10.1051/0004-6361/201629540)

Ajello, M., Rebusco, P., Cappelluti, N., et al. 2009, Galaxy Clusters in the Swift/Burst Alert Telescope Era: Hard X-rays in the Intracluster Medium, *The Astrophysical Journal*, 690, 367, doi: [10.1088/0004-637x/690/1/367](https://doi.org/10.1088/0004-637x/690/1/367)

- Ajello, M., Angioni, R., Axelsson, M., et al. 2020, The Fourth Catalog of Active Galactic Nuclei Detected by the Fermi Large Area Telescope, *The Astrophysical Journal*, 892, 105, doi: [10.3847/1538-4357/ab791e](https://doi.org/10.3847/1538-4357/ab791e)
- Albert, J., Aliu, E., Anderhub, H., et al. 2008, Very High Energy Gamma-Ray Observations of Strong Flaring Activity in M87 in 2008 February, *The Astrophysical Journal Letters*, 685, L23, doi: [10.1086/592348](https://doi.org/10.1086/592348)
- Aleksić, J., Alvarez, E. A., Antonelli, L. A., et al. 2012, Detection of very-high energy γ -ray emission from <ASTROBJ>NGC 1275</ASTROBJ> by the MAGIC telescopes, *Astronomy & Astrophysics*, 539, L2, doi: [10.1051/0004-6361/201118668](https://doi.org/10.1051/0004-6361/201118668)
- Alfvén, H., & Herlofson, N. 1950, Cosmic Radiation and Radio Stars, *Physical Review*, 78, 616, doi: [10.1103/PhysRev.78.616](https://doi.org/10.1103/PhysRev.78.616)
- Antonucci, R. 1993, Unified models for active galactic nuclei and quasars., *Annual Review of Astronomy and Astrophysics*, 31, 473, doi: [10.1146/annurev.aa.31.090193.002353](https://doi.org/10.1146/annurev.aa.31.090193.002353)
- Asada, K., Kamenon, S., Shen, Z.-Q., et al. 2006, The Expanding Radio Lobe of 3C 84 Revealed by VSOP Observations, *Publications of the Astronomical Society of Japan*, 58, 261, doi: [10.1093/pasj/58.2.261](https://doi.org/10.1093/pasj/58.2.261)
- Asmus, D., Hönl, S. F., Gandhi, P., Smette, A., & Duschl, W. J. 2014, The subarc-second mid-infrared view of local active galactic nuclei - I. The N- and Q-band imaging atlas, *Monthly Notices of the Royal Astronomical Society*, 439, 1648, doi: [10.1093/mnras/stu041](https://doi.org/10.1093/mnras/stu041)
- Atwood, W., Albert, A., Baldini, L., et al. 2013, Pass 8: Toward the Full Realization of the Fermi-LAT Scientific Potential, arXiv e-prints, arXiv:1303.3514. <https://arxiv.org/abs/1303.3514>
- Atwood, W. B., Abdo, A. A., Ackermann, M., et al. 2009, The Large Area Telescope on the Fermi Gamma-Ray Space Telescope Mission, *The Astrophysical Journal*, 697, 1071, doi: [10.1088/0004-637x/697/2/1071](https://doi.org/10.1088/0004-637x/697/2/1071)
- Baade, W., & Minkowski, R. 1954a, Identification of the Radio Sources in Cassiopeia, Cygnus A, and Puppis A, *The Astrophysical Journal*, 119, 206, doi: [10.1086/145812](https://doi.org/10.1086/145812)
- Baade, W., & Minkowski, R. 1954b, Identification of the Radio Sources in Cassiopeia, Cygnus A, and Puppis A, *The Astrophysical Journal*, 119, 206, doi: [10.1086/145812](https://doi.org/10.1086/145812)
- Balbus, S. A., & Hawley, J. F. 1991, A Powerful Local Shear Instability in Weakly Magnetized Disks. I. Linear Analysis, *The Astrophysical Journal*, 376, 214, doi: [10.1086/170270](https://doi.org/10.1086/170270)

Ballet, J., Burnett, T. H., Digel, S. W., & Lott, B. 2020, Fermi Large Area Telescope Fourth Source Catalog Data Release 2, arXiv e-prints, arXiv:2005.11208. <https://arxiv.org/abs/2005.11208>

Balmaverde, B., & Capetti, A. 2006, The host galaxy/AGN connection in nearby early-type galaxies. Is there a miniature radio-galaxy in every “core” galaxy?, *Astronomy & Astrophysics*, 447, 97, doi: [10.1051/0004-6361:20054031](https://doi.org/10.1051/0004-6361:20054031)

Barthelmy, S. D., Barbier, L. M., Cummings, J. R., et al. 2005, The Burst Alert Telescope (BAT) on the SWIFT Midex Mission, *Space Science Reviews*, 120, 143, doi: [10.1007/s11214-005-5096-3](https://doi.org/10.1007/s11214-005-5096-3)

Begelman, M. C., & Sikora, M. 1987, Inverse Compton Scattering of Ambient Radiation by a Cold Relativistic Jet: A Source of Beamed, Polarized X-Ray and Optical Observations of X-Ray–selected BL Lacertae Objects, *The Astrophysical Journal*, 322, 650, doi: [10.1086/165760](https://doi.org/10.1086/165760)

Bethe, H., & Heitler, W. 1934, On the Stopping of Fast Particles and on the Creation of Positive Electrons, *Proceedings of the Royal Society of London Series A*, 146, 83, doi: [10.1098/rspa.1934.0140](https://doi.org/10.1098/rspa.1934.0140)

Biretta, J. A., Sparks, W. B., & Macchetto, F. 1999, Hubble Space Telescope Observations of Superluminal Motion in the M87 Jet, *The Astrophysical Journal*, 520, 621, doi: [10.1086/307499](https://doi.org/10.1086/307499)

Birkinshaw, M., & Davies, R. L. 1985a, The orientations of the rotation axes of radio galaxies. I. Radio morphologies of bright elliptical galaxies., *The Astrophysical Journal*, 291, 32, doi: [10.1086/163038](https://doi.org/10.1086/163038)

Birkinshaw, M., & Davies, R. L. 1985b, The orientations of the rotation axes of radio galaxies. I. Radio morphologies of bright elliptical galaxies., *The Astrophysical Journal*, 291, 32, doi: [10.1086/163038](https://doi.org/10.1086/163038)

Blaauw, A. 1997, V. A. Ambartsumian (18 September 1908–12 August 1996), *Journal of Astrophysics and Astronomy*, 18, 1, doi: [10.1007/BF02714847](https://doi.org/10.1007/BF02714847)

Blandford, R., & Eichler, D. 1987, Particle acceleration at astrophysical shocks: A theory of cosmic ray origin, *Physics Report*, 154, 1, doi: [10.1016/0370-1573\(87\)90134-7](https://doi.org/10.1016/0370-1573(87)90134-7)

Blandford, R., Meier, D., & Readhead, A. 2019, Relativistic Jets from Active Galactic Nuclei, *Annual Review of Astronomy and Astrophysics*, 57, 467, doi: [10.1146/annurev-astro-081817-051948](https://doi.org/10.1146/annurev-astro-081817-051948)

Blandford, R. D., & Begelman, M. C. 1999a, On the fate of gas accreting at a low rate on to a black hole, *Monthly Notices of the Royal Astronomical Society*, 303, L1, doi: [10.1046/j.1365-8711.1999.02358.x](https://doi.org/10.1046/j.1365-8711.1999.02358.x)

- Blandford, R. D., & Begelman, M. C. 1999b, On the fate of gas accreting at a low rate on to a black hole, *Monthly Notices of the Royal Astronomical Society*, 303, L1, doi: [10.1046/j.1365-8711.1999.02358.x](https://doi.org/10.1046/j.1365-8711.1999.02358.x)
- Blandford, R. D., & Payne, D. G. 1982, Hydromagnetic flows from accretion disks and the production of radio jets., *Monthly Notices of the Royal Astronomical Society*, 199, 883, doi: [10.1093/mnras/199.4.883](https://doi.org/10.1093/mnras/199.4.883)
- Blandford, R. D., & Znajek, R. L. 1977, Electromagnetic extraction of energy from Kerr black holes., *Monthly Notices of the Royal Astronomical Society*, 179, 433, doi: [10.1093/mnras/179.3.433](https://doi.org/10.1093/mnras/179.3.433)
- Blumenthal, G. R., & Gould, R. J. 1970, Bremsstrahlung, Synchrotron Radiation, and Compton Scattering of High-Energy Electrons Traversing Dilute Gases, *Reviews of Modern Physics*, 42, 237, doi: [10.1103/RevModPhys.42.237](https://doi.org/10.1103/RevModPhys.42.237)
- Böhringer, H., Belsole, E., Kennea, J., et al. 2001, XMM-Newton observations of M 87 and its X-ray halo, *Astronomy & Astrophysics*, 365, L181, doi: [10.1051/0004-6361:20000092](https://doi.org/10.1051/0004-6361:20000092)
- Böttcher, M., Reimer, A., Sweeney, K., & Prakash, A. 2013, Leptonic and Hadronic Modeling of Fermi-detected Blazars, *The Astrophysical Journal*, 768, 54, doi: [10.1088/0004-637x/768/1/54](https://doi.org/10.1088/0004-637x/768/1/54)
- Breeveld, A. A., Landsman, W., Holland, S. T., et al. 2011a, in *American Institute of Physics Conference Series*, Vol. 1358, *Gamma Ray Bursts 2010*, ed. J. E. McEnery, J. L. Racusin, & N. Gehrels (AIP), 373–376, doi: [10.1063/1.3621807](https://doi.org/10.1063/1.3621807)
- Breeveld, A. A., Landsman, W., Holland, S. T., et al. 2011b, in *American Institute of Physics Conference Series*, Vol. 1358, 373–376, doi: [10.1063/1.3621807](https://doi.org/10.1063/1.3621807)
- Breiding, P., Meyer, E. T., Georganopoulos, M., et al. 2023, A multiwavelength study of multiple spectral component jets in AGN: testing the IC/CMB model for the large-scale-jet X-ray emission, *Monthly Notices of the Royal Astronomical Society*, 518, 3222, doi: [10.1093/mnras/stac3081](https://doi.org/10.1093/mnras/stac3081)
- Brodatzki, K. A., Pardy, D. J. S., Becker, J. K., & Schlickeiser, R. 2011, Internal $\gamma\gamma$ Opacity in Active Galactic Nuclei and the Consequences for the TeV Observations of M87 and Cen A, *The Astrophysical Journal*, 736, 98, doi: [10.1088/0004-637x/736/2/98](https://doi.org/10.1088/0004-637x/736/2/98)
- Buchner, J., & Boorman, P. 2023, Statistical Aspects of X-ray Spectral Analysis, arXiv e-prints, arXiv:2309.05705, doi: [10.48550/arXiv.2309.05705](https://doi.org/10.48550/arXiv.2309.05705)
- Burbidge, E. M., Burbidge, G. R., & Prendergast, K. H. 1959, Mass Distribution and Physical Conditions in the Inner Region of NGC 1068., *The Astrophysical Journal*, 130, 26, doi: [10.1086/146693](https://doi.org/10.1086/146693)

- Burbidge, G. R. 1956, On Synchrotron Radiation from Messier 87., *The Astrophysical Journal*, 124, 416, doi: [10.1086/146237](https://doi.org/10.1086/146237)
- Burrows, D. N., Hill, J. E., Nousek, J. A., et al. 2005, The Swift X-Ray Telescope, *Space Science Reviews*, 120, 165, doi: [10.1007/s11214-005-5097-2](https://doi.org/10.1007/s11214-005-5097-2)
- Canvin, J. R., Laing, R. A., Bridle, A. H., & Cotton, W. D. 2005, A relativistic model of the radio jets in NGC 315, *Monthly Notices of the Royal Astronomical Society*, 363, 1223, doi: [10.1111/j.1365-2966.2005.09537.x](https://doi.org/10.1111/j.1365-2966.2005.09537.x)
- Cao, Z., Aharonian, F., An, Q., et al. 2024a, The First LHAASO Catalog of Gamma-Ray Sources, *The Astrophysical Journal Supplement Series*, 271, 25, doi: [10.3847/1538-4365/acfd29](https://doi.org/10.3847/1538-4365/acfd29)
- Cao, Z., Aharonian, F., An, Q., et al. 2024b, Discovery of Very-high-energy Gamma-ray Emissions from the Low Luminosity AGN NGC 4278 by LHAASO, arXiv e-prints, arXiv:2405.07691, doi: [10.48550/arXiv.2405.07691](https://doi.org/10.48550/arXiv.2405.07691)
- Capetti, A., Verdoes Kleijn, G., & Chiaberge, M. 2005, The HST view of the nuclear emission line region in low luminosity radio-galaxies, *Astronomy & Astrophysics*, 439, 935, doi: [10.1051/0004-6361:20041609](https://doi.org/10.1051/0004-6361:20041609)
- Cappellari, M., Emsellem, E., Krajnović, D., et al. 2011, The ATLAS^{3D} project - I. A volume-limited sample of 260 nearby early-type galaxies: science goals and selection criteria, *Monthly Notices of the Royal Astronomical Society*, 413, 813, doi: [10.1111/j.1365-2966.2010.18174.x](https://doi.org/10.1111/j.1365-2966.2010.18174.x)
- Cash, W. 1979, Parameter estimation in astronomy through application of the likelihood ratio., *The Astrophysical Journal*, 228, 939, doi: [10.1086/156922](https://doi.org/10.1086/156922)
- Celotti, A., Ghisellini, G., & Chiaberge, M. 2001, Large-scale jets in active galactic nuclei: multiwavelength mapping, *Monthly Notices of the Royal Astronomical Society*, 321, L1, doi: [10.1046/j.1365-8711.2001.04160.x](https://doi.org/10.1046/j.1365-8711.2001.04160.x)
- Chandra, S., Boettcher, M., Goswami, P., et al. 2021, X-Ray Observations of 1ES 1959+650 in Its High-activity State in 2016-2017 with AstroSat and Swift, *The Astrophysical Journal*, 918, 67, doi: [10.3847/1538-4357/ac01d1](https://doi.org/10.3847/1538-4357/ac01d1)
- Chatterjee, K., Liska, M., Tchekhovskoy, A., & Markoff, S. B. 2019, Accelerating AGN jets to parsec scales using general relativistic MHD simulations, *Monthly Notices of the Royal Astronomical Society*, 490, 2200, doi: [10.1093/mnras/stz2626](https://doi.org/10.1093/mnras/stz2626)
- Chiaberge, M., Capetti, A., & Celotti, A. 1999, The HST view of FR I radio galaxies: evidence for non-thermal nuclear sources, *Astronomy & Astrophysics*, 349, 77, doi: [10.48550/arXiv.astro-ph/9907064](https://doi.org/10.48550/arXiv.astro-ph/9907064)

- Costamante, L., Bonnoli, G., Tavecchio, F., et al. 2018, The NuSTAR view on hard-TeV BL Lacs, *Monthly Notices of the Royal Astronomical Society*, 477, 4257, doi: [10.1093/mnras/sty857](https://doi.org/10.1093/mnras/sty857)
- Costamante, L., Ghisellini, G., Giommi, P., et al. 2001, Extreme synchrotron BL Lac objects. Stretching the blazar sequence, *Astronomy & Astrophysics*, 371, 512, doi: [10.1051/0004-6361:20010412](https://doi.org/10.1051/0004-6361:20010412)
- Cotton, W. D., Feretti, L., Giovannini, G., Lara, L., & Venturi, T. 1999, A Parsec-Scale Accelerating Radio Jet in the Giant Radio Galaxy NGC 315, *The Astrophysical Journal*, 519, 108, doi: [10.1086/307358](https://doi.org/10.1086/307358)
- CTA Consortium, & Ong, R. A. 2019, in *European Physical Journal Web of Conferences*, Vol. 209, *European Physical Journal Web of Conferences*, 01038, doi: [10.1051/epjconf/201920901038](https://doi.org/10.1051/epjconf/201920901038)
- Curtis, H. D. 1918, *Descriptions of 762 Nebulae and Clusters Photographed with the Crossley Reflector*, *Publications of Lick Observatory*, 13, 9
- Das, S., Gupta, N., & Razzaque, S. 2020, Ultrahigh-energy Cosmic-Ray Interactions as the Origin of Very High-energy γ -Rays from BL Lacertae Objects, *The Astrophysical Journal*, 889, 149, doi: [10.3847/1538-4357/ab6131](https://doi.org/10.3847/1538-4357/ab6131)
- de Jong, S., Beckmann, V., Soldi, S., Tramacere, A., & Gros, A. 2015, High-energy emission processes in M87, *Monthly Notices of the Royal Astronomical Society*, 450, 4333, doi: [10.1093/mnras/stv927](https://doi.org/10.1093/mnras/stv927)
- de Menezes, R., Nemmen, R., Finke, J. D., Almeida, I., & Rani, B. 2020, Gamma-ray observations of low-luminosity active galactic nuclei, *Monthly Notices of the Royal Astronomical Society*, 492, 4120, doi: [10.1093/mnras/staa083](https://doi.org/10.1093/mnras/staa083)
- Doi, A., Kohno, K., Nakanishi, K., et al. 2013, Nuclear Radio Jet from a Low-luminosity Active Galactic Nucleus in NGC 4258, *The Astrophysical Journal*, 765, 63, doi: [10.1088/0004-637x/765/1/63](https://doi.org/10.1088/0004-637x/765/1/63)
- Donato, D., Sambruna, R. M., & Gliozzi, M. 2004, Obscuration and Origin of Nuclear X-Ray Emission in FR I Radio Galaxies, *The Astrophysical Journal*, 617, 915, doi: [10.1086/425575](https://doi.org/10.1086/425575)
- Done, C., Gierliński, M., & Kubota, A. 2007, Modelling the behaviour of accretion flows in X-ray binaries. Everything you always wanted to know about accretion but were afraid to ask, *The Astronomy and Astrophysics Review*, 15, 1, doi: [10.1007/s00159-007-0006-1](https://doi.org/10.1007/s00159-007-0006-1)
- Dreyer, J. L. E. 1888, *A New General Catalogue of Nebulae and Clusters of Stars, being the Catalogue of the late Sir John F. W. Herschel, Bart, revised, corrected, and enlarged*, *Memoirs of the Royal Astronomical Society*, 49, 1

Dutta, S., & Gupta, N. 2024, Multiple Emission Regions in Jets of Low Luminosity Active Galactic Nucleus in NGC 4278, arXiv e-prints, arXiv:2405.15657, doi: [10.48550/arXiv.2405.15657](https://doi.org/10.48550/arXiv.2405.15657)

Eracleous, M., Hwang, J. A., & Flohic, H. M. L. G. 2010, Spectral Energy Distributions of Weak Active Galactic Nuclei Associated with Low-Ionization Nuclear Emission Regions, *The Astrophysical Journal Supplement Series*, 187, 135, doi: [10.1088/0067-0049/187/1/135](https://doi.org/10.1088/0067-0049/187/1/135)

Evans, P. A., Nixon, C. J., Campana, S., et al. 2023, Monthly quasi-periodic eruptions from repeated stellar disruption by a massive black hole, *Nature Astronomy*, 7, 1368, doi: [10.1038/s41550-023-02073-y](https://doi.org/10.1038/s41550-023-02073-y)

Event Horizon Telescope Collaboration, Akiyama, K., Alberdi, A., et al. 2019, First M87 Event Horizon Telescope Results. VI. The Shadow and Mass of the Central Black Hole, *The Astrophysical Journal Letters*, 875, L6, doi: [10.3847/2041-8213/ab1141](https://doi.org/10.3847/2041-8213/ab1141)

Fabian, A. C. 2012, Observational Evidence of Active Galactic Nuclei Feedback, *Annual Review of Astronomy and Astrophysics*, 50, 455, doi: [10.1146/annurev-astro-081811-125521](https://doi.org/10.1146/annurev-astro-081811-125521)

Fath, E. A. 1909, The spectra of some spiral nebulae and globular star clusters, *Lick Observatory Bulletin*, 149, 71, doi: [10.5479/ADS/bib/1909LicOB.5.71F](https://doi.org/10.5479/ADS/bib/1909LicOB.5.71F)

Ferrarese, L., Ford, H. C., & Jaffe, W. 1996, Evidence for a Massive Black Hole in the Active Galaxy NGC 4261 from Hubble Space Telescope Images and Spectra, *The Astrophysical Journal*, 470, 444, doi: [10.1086/177876](https://doi.org/10.1086/177876)

Fitzpatrick, E. L. 1999a, Correcting for the Effects of Interstellar Extinction, *Publications of the Astronomical Society of the Pacific*, 111, 63, doi: [10.1086/316293](https://doi.org/10.1086/316293)

Fitzpatrick, E. L. 1999b, Correcting for the Effects of Interstellar Extinction, *Publications of the Astronomical Society of the Pacific*, 111, 63, doi: [10.1086/316293](https://doi.org/10.1086/316293)

Fraija, N., & Marinelli, A. 2016, Neutrino, γ -Ray, and Cosmic-Ray Fluxes from the Core of the Closest Radio Galaxies, *The Astrophysical Journal*, 830, 81, doi: [10.3847/0004-637x/830/2/81](https://doi.org/10.3847/0004-637x/830/2/81)

Frank, J., King, A., & Raine, D. J. 2002, *Accretion Power in Astrophysics: Third Edition*

Freedman, W. L., Hughes, S. M., Madore, B. F., et al. 1994, The Hubble Space Telescope Extragalactic Distance Scale Key Project. I. The Discovery of Cepheids and a New Distance to M81, *The Astrophysical Journal*, 427, 628, doi: [10.1086/174172](https://doi.org/10.1086/174172)

Fujita, Y., & Nagai, H. 2017, Discovery of a new subparsec counterjet in NGC 1275: the inclination angle and the environment, *Monthly Notices of the Royal Astronomical Society*, 465, L94, doi: [10.1093/mnrasl/slw217](https://doi.org/10.1093/mnrasl/slw217)

Fukazawa, Y., Finke, J., Stawarz, Ł., et al. 2015, Suzaku Observations of γ -Ray Bright Radio Galaxies: Origin of the X-Ray Emission and Broadband Modeling, *The Astrophysical Journal*, 798, 74, doi: [10.1088/0004-637x/798/2/74](https://doi.org/10.1088/0004-637x/798/2/74)

Gao, S., Pohl, M., & Winter, W. 2017, On the Direct Correlation between Gamma-Rays and PeV Neutrinos from Blazars, *The Astrophysical Journal*, 843, 109, doi: [10.3847/1538-4357/aa7754](https://doi.org/10.3847/1538-4357/aa7754)

García-Burillo, S., Combes, F., Ramos Almeida, C., et al. 2019, ALMA images the many faces of the <ASTROBJ>NGC 1068</ASTROBJ> torus and its surroundings, *Astronomy & Astrophysics*, 632, A61, doi: [10.1051/0004-6361/201936606](https://doi.org/10.1051/0004-6361/201936606)

Gehrels, N., Chincarini, G., Giommi, P., et al. 2004, The Swift Gamma-Ray Burst Mission, *The Astrophysical Journal*, 611, 1005, doi: [10.1086/422091](https://doi.org/10.1086/422091)

Ghisellini, G. 2013, *Radiative Processes in High Energy Astrophysics*, Vol. 873, doi: [10.1007/978-3-319-00612-3](https://doi.org/10.1007/978-3-319-00612-3)

Ghisellini, G., Celotti, A., Tavecchio, F., Haardt, F., & Sbarrato, T. 2014, Radio-loud active galactic nuclei at high redshifts and the cosmic microwave background, *Monthly Notices of the Royal Astronomical Society*, 438, 2694, doi: [10.1093/mnras/stt2394](https://doi.org/10.1093/mnras/stt2394)

Ghosal, B., Tolamatti, A., Singh, K. K., et al. 2020, Multiwavelength study of the radio galaxy NGC 1275 with TACTIC, Fermi and Swift during December, 2016 - February, 2017, *Nature Astronomy*, 80, 101402, doi: [10.1016/j.newast.2020.101402](https://doi.org/10.1016/j.newast.2020.101402)

Ginzburg, V. L., & Syrovatskii, S. I. 1964, *The Origin of Cosmic Rays*

Giozzi, M., Sambruna, R. M., & Brandt, W. N. 2003, On the origin of the X-rays and the nature of accretion in <ASTROBJ>NGC 4261</ASTROBJ>, *Astronomy & Astrophysics*, 408, 949, doi: [10.1051/0004-6361:20031050](https://doi.org/10.1051/0004-6361:20031050)

Globus, N., & Levinson, A. 2016, The collimation of magnetic jets by disc winds, *Monthly Notices of the Royal Astronomical Society*, 461, 2605, doi: [10.1093/mnras/stw1474](https://doi.org/10.1093/mnras/stw1474)

González-Martín, O., Masegosa, J., Márquez, I., Guerrero, M. A., & Dultzin-Hacyan, D. 2006, X-ray nature of the LINER nuclear sources, *Astronomy & Astrophysics*, 460, 45, doi: [10.1051/0004-6361:20054756](https://doi.org/10.1051/0004-6361:20054756)

- González-Martín, O., Masegosa, J., García-Bernete, I., et al. 2019a, Exploring the Mid-infrared SEDs of Six AGN Dusty Torus Models. I. Synthetic Spectra, *The Astrophysical Journal*, 884, 10, doi: [10.3847/1538-4357/ab3e6b](https://doi.org/10.3847/1538-4357/ab3e6b)
- González-Martín, O., Masegosa, J., García-Bernete, I., et al. 2019b, Exploring the Mid-infrared SEDs of Six AGN Dusty Torus Models. II. The Data, *The Astrophysical Journal*, 884, 11, doi: [10.3847/1538-4357/ab3e4f](https://doi.org/10.3847/1538-4357/ab3e4f)
- Gorenstein, P., Gursky, H., & Garmire, G. 1968, The Analysis of X-Ray Spectra, *The Astrophysical Journal*, 153, 885, doi: [10.1086/149713](https://doi.org/10.1086/149713)
- Gu, Q. S., Huang, J. S., Wilson, G., & Fazio, G. G. 2007, Direct Evidence from Spitzer for a Low-Luminosity AGN at the Center of the Elliptical Galaxy NGC 315, *The Astrophysical Journal Letters*, 671, L105, doi: [10.1086/525018](https://doi.org/10.1086/525018)
- Gulati, S., Bhattacharya, D., Ramadevi, M. C., Stalin, C. S., & Sreekumar, P. 2023, Multiwavelength study of radio galaxy Pictor A: detection of western hotspot in far-UV and possible origin of high energy emissions, *Monthly Notices of the Royal Astronomical Society*, 521, 2704, doi: [10.1093/mnras/stad716](https://doi.org/10.1093/mnras/stad716)
- Gupta, A. C., Krichbaum, T. P., Wiita, P. J., et al. 2012, Multiwavelength intraday variability of the BL Lacertae S5 0716+714, *Monthly Notices of the Royal Astronomical Society*, 425, 1357, doi: [10.1111/j.1365-2966.2012.21550.x](https://doi.org/10.1111/j.1365-2966.2012.21550.x)
- H. E. S. S. Collaboration, Abdalla, H., Adam, R., et al. 2020a, Resolving acceleration to very high energies along the jet of Centaurus A, *Nature*, 582, 356, doi: [10.1038/s41586-020-2354-1](https://doi.org/10.1038/s41586-020-2354-1)
- H. E. S. S. Collaboration, Abdalla, H., Adam, R., et al. 2020b, Resolving acceleration to very high energies along the jet of Centaurus A, *Nature*, 582, 356, doi: [10.1038/s41586-020-2354-1](https://doi.org/10.1038/s41586-020-2354-1)
- Hahn, J. 2015, in *International Cosmic Ray Conference*, Vol. 34, 34th International Cosmic Ray Conference (ICRC2015), 917
- Harris, D. E., & Krawczynski, H. 2006, X-Ray Emission from Extragalactic Jets, *Annual Review of Astronomy and Astrophysics*, 44, 463, doi: [10.1146/annurev.astro.44.051905.092446](https://doi.org/10.1146/annurev.astro.44.051905.092446)
- Harrison, C. M., Costa, T., Tadhunter, C. N., et al. 2018, AGN outflows and feedback twenty years on, *Nature Astronomy*, 2, 198, doi: [10.1038/s41550-018-0403-6](https://doi.org/10.1038/s41550-018-0403-6)
- Hazard, C., Mackey, M. B., & Shimmins, A. J. 1963a, Investigation of the Radio Source 3C 273 By The Method of Lunar Occultations, *Nature*, 197, 1037, doi: [10.1038/1971037a0](https://doi.org/10.1038/1971037a0)

- Hazard, C., Mackey, M. B., & Shimmins, A. J. 1963b, Investigation of the Radio Source 3C 273 By The Method of Lunar Occultations, *Nature*, 197, 1037, doi: [10.1038/1971037a0](https://doi.org/10.1038/1971037a0)
- Heckman, T. M., Lebofsky, M. J., Rieke, G. H., & van Breugel, W. 1983, An infrared and optical investigation of galactic nuclei with compact Radio Source., *The Astrophysical Journal*, 272, 400, doi: [10.1086/161308](https://doi.org/10.1086/161308)
- Ho, L. C. 2008, Nuclear activity in nearby galaxies., *Annual Review of Astronomy and Astrophysics*, 46, 475, doi: [10.1146/annurev.astro.45.051806.110546](https://doi.org/10.1146/annurev.astro.45.051806.110546)
- Ho, L. C., Filippenko, A. V., & Sargent, W. L. 1995, A Search for “Dwarf” Seyfert Nuclei. II. an Optical Spectral Atlas of the Nuclei of Nearby Galaxies, *The Astrophysical Journal Supplement Series*, 98, 477, doi: [10.1086/192170](https://doi.org/10.1086/192170)
- Ho, L. C., Filippenko, A. V., & Sargent, W. L. W. 1997a, A Search for “Dwarf” Seyfert Nuclei. III. Spectroscopic Parameters and Properties of the Host Galaxies, *The Astrophysical Journal Supplement Series*, 112, 315, doi: [10.1086/313041](https://doi.org/10.1086/313041)
- Ho, L. C., Filippenko, A. V., Sargent, W. L. W., & Peng, C. Y. 1997b, A Search for “Dwarf” Seyfert Nuclei. IV. Nuclei with Broad H α Emission, *The Astrophysical Journal Supplement Series*, 112, 391, doi: [10.1086/313042](https://doi.org/10.1086/313042)
- Hönig, S. F., & Beckert, T. 2007, Active galactic nuclei dust tori at low and high luminosities, *Monthly Notices of the Royal Astronomical Society*, 380, 1172, doi: [10.1111/j.1365-2966.2007.12157.x](https://doi.org/10.1111/j.1365-2966.2007.12157.x)
- Hoof, S., Geringer-Sameth, A., & Trotta, R. 2020, A global analysis of dark matter signals from 27 dwarf spheroidal galaxies using 11 years of Fermi-LAT observations, *Journal of Cosmology and Astroparticle Physics*, 2020, 012, doi: [10.1088/1475-7516/2020/02/012](https://doi.org/10.1088/1475-7516/2020/02/012)
- Hoyle, F., & Fowler, W. A. 1963, On the nature of strong radio sources, *Monthly Notices of the Royal Astronomical Society*, 125, 169, doi: [10.1093/mnras/125.2.169](https://doi.org/10.1093/mnras/125.2.169)
- IceCube Collaboration, Aartsen, M. G., Ackermann, M., et al. 2018a, Multimessenger observations of a flaring blazar coincident with high-energy neutrino IceCube-170922A, *Science*, 361, eaat1378, doi: [10.1126/science.aat1378](https://doi.org/10.1126/science.aat1378)
- IceCube Collaboration, Aartsen, M. G., Ackermann, M., et al. 2018b, Multimessenger observations of a flaring blazar coincident with high-energy neutrino IceCube-170922A, *Science*, 361, eaat1378, doi: [10.1126/science.aat1378](https://doi.org/10.1126/science.aat1378)
- IceCube Collaboration, Abbasi, R., Ackermann, M., et al. 2022, Evidence for neutrino emission from the nearby active galaxy NGC 1068, *Science*, 378, 538, doi: [10.1126/science.abg3395](https://doi.org/10.1126/science.abg3395)

- Imanishi, M., Nakanishi, K., Izumi, T., & Wada, K. 2018, ALMA Reveals an Inhomogeneous Compact Rotating Dense Molecular Torus at the NGC 1068 Nucleus, *The Astrophysical Journal Letters*, 853, L25, doi: [10.3847/2041-8213/aaa8df](https://doi.org/10.3847/2041-8213/aaa8df)
- Jaffe, W., Ford, H. C., Ferrarese, L., van den Bosch, F., & O'Connell, R. W. 1993, A large nuclear accretion disk in the active galaxy NGC4261, *Nature*, 364, 213, doi: [10.1038/364213a0](https://doi.org/10.1038/364213a0)
- Jansen, F., Lumb, D., Altieri, B., et al. 2001, XMM-Newton observatory. I. The spacecraft and operations, *Astronomy & Astrophysics*, 365, L1, doi: [10.1051/0004-6361:20000036](https://doi.org/10.1051/0004-6361:20000036)
- Jansky, K. G. 1933, Radio Waves from Outside the Solar System, *Nature*, 132, 66, doi: [10.1038/132066a0](https://doi.org/10.1038/132066a0)
- Jennison, R. C. 1959, in *URSI Symp. 1: Paris Symposium on Radio Astronomy*, ed. R. N. Bracewell, Vol. 9, 309
- Jones, D. L., & Wehrle, A. E. 1997, VLBA Imaging of NGC 4261: Symmetric Parsec-scale Jets and the Inner Accretion Region, *The Astrophysical Journal*, 484, 186, doi: [10.1086/304320](https://doi.org/10.1086/304320)
- Jones, F. C., & Ellison, D. C. 1991, The plasma physics of shock acceleration, *Space Science Reviews*, 58, 259, doi: [10.1007/BF01206003](https://doi.org/10.1007/BF01206003)
- Kalberla, P. M. W., Burton, W. B., Hartmann, D., et al. 2005, The Leiden/Argentine/Bonn (LAB) Survey of Galactic HI. Final data release of the combined LDS and IAR surveys with improved stray-radiation corrections, *Astronomy & Astrophysics*, 440, 775, doi: [10.1051/0004-6361:20041864](https://doi.org/10.1051/0004-6361:20041864)
- Kewley, L. J., Groves, B., Kauffmann, G., & Heckman, T. 2006, The host galaxies and classification of active galactic nuclei, *Monthly Notices of the Royal Astronomical Society*, 372, 961, doi: [10.1111/j.1365-2966.2006.10859.x](https://doi.org/10.1111/j.1365-2966.2006.10859.x)
- King, A. L., Miller, J. M., Bietenholz, M., et al. 2016, Discrete knot ejection from the jet in a nearby low-luminosity active galactic nucleus, M81*, *Nature Physics*, 12, 772, doi: [10.1038/nphys3724](https://doi.org/10.1038/nphys3724)
- Kirk, J. G., Rieger, F. M., & Mastichiadis, A. 1998, Particle acceleration and synchrotron emission in blazar jets, *Astronomy & Astrophysics*, 333, 452, doi: [10.48550/arXiv.astro-ph/9801265](https://doi.org/10.48550/arXiv.astro-ph/9801265)
- Konigl, A. 1981, Relativistic jets as X-ray and gamma-ray sources., *The Astrophysical Journal*, 243, 700, doi: [10.1086/158638](https://doi.org/10.1086/158638)
- Kormendy, J. 2004, in *Coevolution of Black Holes and Galaxies*, ed. L. C. Ho, arXiv. <https://arxiv.org/abs/astro-ph/0306353>

- Kormendy, J., & Ho, L. C. 2013, Coevolution (Or Not) of Supermassive Black Holes and Host Galaxies, *Annual Review of Astronomy and Astrophysics*, 51, 511, doi: [10.1146/annurev-astro-082708-101811](https://doi.org/10.1146/annurev-astro-082708-101811)
- Kovalev, Y. Y., Kellermann, K. I., Lister, M. L., et al. 2005, Sub-Milliarcsecond Imaging of Quasars and Active Galactic Nuclei. IV. Fine-Scale Structure, *The Astronomical Journal*, 130, 2473, doi: [10.1086/497430](https://doi.org/10.1086/497430)
- Laor, A. 2003, On the Nature of Low-Luminosity Narrow-Line Active Galactic Nuclei, *The Astrophysical Journal*, 590, 86, doi: [10.1086/375008](https://doi.org/10.1086/375008)
- Lazio, T. J. W., Waltman, E. B., Ghigo, F. D., et al. 2001, A Dual-Frequency, Multiyear Monitoring Program of Compact Radio Sources, *The Astrophysical Journal Supplement Series*, 136, 265, doi: [10.1086/322531](https://doi.org/10.1086/322531)
- Lenain, J. P., & Walter, R. 2011, Search for high-energy γ -ray emission from galaxies of the Local Group with Fermi/LAT, *Astronomy & Astrophysics*, 535, A19, doi: [10.1051/0004-6361/201117523](https://doi.org/10.1051/0004-6361/201117523)
- Livio, M., Ogilvie, G. I., & Pringle, J. E. 1999, Extracting Energy from Black Holes: The Relative Importance of the Blandford-Znajek Mechanism, *The Astrophysical Journal*, 512, 100, doi: [10.1086/306777](https://doi.org/10.1086/306777)
- Lott, B., Gasparri, D., & Ciprini, S. 2020, The Fourth Catalog of Active Galactic Nuclei Detected by the Fermi Large Area Telescope – Data Release 2, arXiv e-prints, arXiv:2010.08406. <https://arxiv.org/abs/2010.08406>
- Lucchini, M., Krauß, F., & Markoff, S. 2019, The unique case of the active galactic nucleus core of M87: a misaligned low-power blazar?, *Monthly Notices of the Royal Astronomical Society*, 489, 1633, doi: [10.1093/mnras/stz2125](https://doi.org/10.1093/mnras/stz2125)
- Lynden-Bell, D. 1969, Galactic Nuclei as Collapsed Old Quasars, *Nature*, 223, 690, doi: [10.1038/223690a0](https://doi.org/10.1038/223690a0)
- MAGIC Collaboration, Acciari, V. A., Ansoldi, S., et al. 2020a, Broadband characterisation of the very intense TeV flares of the blazar 1ES 1959+650 in 2016, *Astronomy & Astrophysics*, 638, A14, doi: [10.1051/0004-6361/201935450](https://doi.org/10.1051/0004-6361/201935450)
- MAGIC Collaboration, Acciari, V. A., Ansoldi, S., et al. 2020b, Study of the variable broadband emission of Markarian 501 during the most extreme Swift X-ray activity, *Astronomy & Astrophysics*, 637, A86, doi: [10.1051/0004-6361/201834603](https://doi.org/10.1051/0004-6361/201834603)
- MAGIC Collaboration, Acciari, V. A., Ansoldi, S., et al. 2020c, Monitoring of the radio galaxy M 87 during a low-emission state from 2012 to 2015 with MAGIC, *Monthly Notices of the Royal Astronomical Society*, 492, 5354, doi: [10.1093/mnras/staa014](https://doi.org/10.1093/mnras/staa014)

MAGIC Collaboration, Acciari, V. A., Ansoldi, S., et al. 2020d, Study of the variable broadband emission of Markarian 501 during the most extreme Swift X-ray activity, *Astronomy & Astrophysics*, 637, A86, doi: [10.1051/0004-6361/201834603](https://doi.org/10.1051/0004-6361/201834603)

MAGIC Collaboration, Abe, S., Abhir, J., et al. 2024, Insights into the broadband emission of the TeV blazar Mrk 501 during the first X-ray polarization measurements, *Astronomy & Astrophysics*, 685, A117, doi: [10.1051/0004-6361/202348709](https://doi.org/10.1051/0004-6361/202348709)

Marin, F. 2016, Are there reliable methods to estimate the nuclear orientation of Seyfert galaxies?, *Monthly Notices of the Royal Astronomical Society*, 460, 3679, doi: [10.1093/mnras/stw1131](https://doi.org/10.1093/mnras/stw1131)

Marin, F., Barnouin, T., Ehlert, S. R., et al. 2023, An X-rays-to-radio investigation of the nuclear polarization from the radio-galaxy Centaurus A, *Monthly Notices of the Royal Astronomical Society*, 526, 6321, doi: [10.1093/mnras/stad3059](https://doi.org/10.1093/mnras/stad3059)

Marinelli, A., Fraija, N., & Patricelli, B. 2014, The Hadronic Picture of the Radio-galaxy M87, arXiv e-prints, arXiv:1410.8549. <https://arxiv.org/abs/1410.8549>

Markoff, S., Nowak, M., Falcke, H., Maccarone, T., & Fender, R. 2004, Exploring the role of jets in X-ray binaries and low-luminosity AGN, *Nuclear Physics B Proceedings Supplements*, 132, 129, doi: [10.1016/j.nuclphysbps.2004.04.016](https://doi.org/10.1016/j.nuclphysbps.2004.04.016)

Marshall, H. L., Miller, B. P., Davis, D. S., et al. 2002, A High-Resolution X-Ray Image of the Jet in M87, *The Astrophysical Journal*, 564, 683, doi: [10.1086/324396](https://doi.org/10.1086/324396)

Mason, K. O., Breeveld, A., Much, R., et al. 2001, The XMM-Newton optical/UV monitor telescope, *Astronomy & Astrophysics*, 365, L36, doi: [10.1051/0004-6361:20000044](https://doi.org/10.1051/0004-6361:20000044)

Massaro, E., Perri, M., Giommi, P., & Nesci, R. 2004, Log-parabolic spectra and particle acceleration in the BL Lac object Mkn 421: Spectral analysis of the complete BeppoSAX wide band X-ray data set, *Astronomy & Astrophysics*, 413, 489, doi: [10.1051/0004-6361:20031558](https://doi.org/10.1051/0004-6361:20031558)

Mattox, J. R., Bertsch, D. L., Chiang, J., et al. 1996, The Likelihood Analysis of EGRET Data, *The Astrophysical Journal*, 461, 396, doi: [10.1086/177068](https://doi.org/10.1086/177068)

McHardy, I. M., Koerding, E., Knigge, C., Uttley, P., & Fender, R. P. 2006, Active galactic nuclei as scaled-up Galactic black holes, *Nature*, 444, 730, doi: [10.1038/nature05389](https://doi.org/10.1038/nature05389)

McKinney, J. C. 2006, General relativistic magnetohydrodynamic simulations of the jet formation and large-scale propagation from black hole accretion systems, *Monthly Notices of the Royal Astronomical Society*, 368, 1561, doi: [10.1111/j.1365-2966.2006.10256.x](https://doi.org/10.1111/j.1365-2966.2006.10256.x)

Messier, C. 1781, Catalogue des Nébuleuses et des Amas d'Étoiles (Catalog of Nebulae and Star Clusters), *Connaissance des Temps ou des Mouvements Célestes*, for 1784, p. 227-267

Mukherjee, R., & VERITAS Collaboration. 2017, VERITAS detection of the radio galaxy NGC 1275 with elevated very-high-energy gamma-ray emission, *The Astronomer's Telegram*, 9931, 1

Nagai, H., Suzuki, K., Asada, K., et al. 2010, VLBI Monitoring of 3C 84 (NGC 1275) in Early Phase of the 2005 Outburst, *Publications of the Astronomical Society of Japan*, 62, L11, doi: [10.1093/pasj/62.2.L11](https://doi.org/10.1093/pasj/62.2.L11)

Nagar, N. M., Falcke, H., & Wilson, A. S. 2005, Radio sources in low-luminosity active galactic nuclei. IV. Radio luminosity function, importance of jet power, and radio properties of the complete Palomar sample, *Astronomy & Astrophysics*, 435, 521, doi: [10.1051/0004-6361:20042277](https://doi.org/10.1051/0004-6361:20042277)

Nagar, N. M., Wilson, A. S., & Falcke, H. 2001, Evidence for Jet Domination of the Nuclear Radio Emission in Low-Luminosity Active Galactic Nuclei, *The Astrophysical Journal Letters*, 559, L87, doi: [10.1086/323938](https://doi.org/10.1086/323938)

Narayan, R., Igumenshchev, I. V., & Abramowicz, M. A. 2000, Self-similar Accretion Flows with Convection, *The Astrophysical Journal*, 539, 798, doi: [10.1086/309268](https://doi.org/10.1086/309268)

Narayan, R., & Yi, I. 1994, Advection-dominated Accretion: A Self-similar Solution, *The Astrophysical Journal Letters*, 428, L13, doi: [10.1086/187381](https://doi.org/10.1086/187381)

Nemmen, R. S., Storchi-Bergmann, T., & Eracleous, M. 2014a, Spectral models for low-luminosity active galactic nuclei in LINERs: the role of advection-dominated accretion and jets, *Monthly Notices of the Royal Astronomical Society*, 438, 2804, doi: [10.1093/mnras/stt2388](https://doi.org/10.1093/mnras/stt2388)

Nemmen, R. S., Storchi-Bergmann, T., & Eracleous, M. 2014b, Spectral models for low-luminosity active galactic nuclei in LINERs: the role of advection-dominated accretion and jets, *Monthly Notices of the Royal Astronomical Society*, 438, 2804, doi: [10.1093/mnras/stt2388](https://doi.org/10.1093/mnras/stt2388)

Netzer, H. 2013, *The Physics and Evolution of Active Galactic Nuclei*

Netzer, H. 2015, Revisiting the Unified Model of Active Galactic Nuclei, *Annual Review of Astronomy and Astrophysics*, 53, 365, doi: [10.1146/annurev-astro-082214-122302](https://doi.org/10.1146/annurev-astro-082214-122302)

Oke, J. B. 1963, Absolute Energy Distribution in the Optical Spectrum of 3C 273, *Nature*, 197, 1040, doi: [10.1038/1971040b0](https://doi.org/10.1038/1971040b0)

- Padovani, P., Miller, N., Kellermann, K. I., et al. 2011, The VLA Survey of Chandra Deep Field South. V. Evolution and Luminosity Functions of Sub-millijansky Radio Sources and the Issue of Radio Emission in Radio-quiet Active Galactic Nuclei, *The Astrophysical Journal*, 740, 20, doi: [10.1088/0004-637x/740/1/20](https://doi.org/10.1088/0004-637x/740/1/20)
- Padovani, P., Alexander, D. M., Assef, R. J., et al. 2017, Active galactic nuclei: what's in a name?, *The Astronomy and Astrophysics Review*, 25, 2, doi: [10.1007/s00159-017-0102-9](https://doi.org/10.1007/s00159-017-0102-9)
- Page, M. J., Soria, R., Zane, S., Wu, K., & Starling, R. L. C. 2004, Highly ionized Fe K α emission lines from the LINER galaxy M 81, *Astronomy & Astrophysics*, 422, 77, doi: [10.1051/0004-6361:20034451](https://doi.org/10.1051/0004-6361:20034451)
- Paliya, V. S., Marcotulli, L., Ajello, M., et al. 2017, General Physical Properties of CGRaBS Blazars, *The Astrophysical Journal*, 851, 33, doi: [10.3847/1538-4357/aa98e1](https://doi.org/10.3847/1538-4357/aa98e1)
- Perlman, E. S., Sparks, W. B., Radomski, J., et al. 2001, Deep 10 Micron Imaging of M87, *The Astrophysical Journal Letters*, 561, L51, doi: [10.1086/324515](https://doi.org/10.1086/324515)
- Pian, E., Romano, P., Maoz, D., et al. 2010, Variability and spectral energy distributions of low-luminosity active galactic nuclei: a simultaneous X-ray/UV look with Swift, *Monthly Notices of the Royal Astronomical Society*, 401, 677, doi: [10.1111/j.1365-2966.2009.15689.x](https://doi.org/10.1111/j.1365-2966.2009.15689.x)
- Piner, B. G., Jones, D. L., & Wehrle, A. E. 2001, Orientation and Speed of the Parsec-Scale Jet in NGC 4261 (3C 270), *The Astronomical Journal*, 122, 2954, doi: [10.1086/323927](https://doi.org/10.1086/323927)
- Piran, T. 1978, The role of viscosity and cooling mechanisms in the stability of accretion disks., *The Astrophysical Journal*, 221, 652, doi: [10.1086/156069](https://doi.org/10.1086/156069)
- Poole, T. S., Breeveld, A. A., Page, M. J., et al. 2008, Photometric calibration of the Swift ultraviolet/optical telescope, *Monthly Notices of the Royal Astronomical Society*, 383, 627, doi: [10.1111/j.1365-2966.2007.12563.x](https://doi.org/10.1111/j.1365-2966.2007.12563.x)
- Pooley, G. 2011, Radio flare in M81, *The Astronomer's Telegram*, 3621, 1
- Potter, W. J., & Cotter, G. 2013, Synchrotron and inverse-Compton emission from blazar jets - II. An accelerating jet model with a geometry set by observations of M87, *Monthly Notices of the Royal Astronomical Society*, 429, 1189, doi: [10.1093/mnras/sts407](https://doi.org/10.1093/mnras/sts407)
- Pratim Basumallick, P., & Gupta, N. 2017, Constraints on a Proton Synchrotron Origin of VHE Gamma Rays from the Extended Jet of AP Librae, *The Astrophysical Journal*, 844, 58, doi: [10.3847/1538-4357/aa7a12](https://doi.org/10.3847/1538-4357/aa7a12)

- Predehl, P., Andritschke, R., Arefiev, V., et al. 2021, The eROSITA X-ray telescope on SRG, *Astronomy & Astrophysics*, 647, A1, doi: [10.1051/0004-6361/202039313](https://doi.org/10.1051/0004-6361/202039313)
- Prieto, M. A., Fernández-Ontiveros, J. A., Markoff, S., Espada, D., & González-Martín, O. 2016, The central parsecs of M87: jet emission and an elusive accretion disc, *Monthly Notices of the Royal Astronomical Society*, 457, 3801, doi: [10.1093/mnras/stw166](https://doi.org/10.1093/mnras/stw166)
- Pu, H.-Y., Asada, K., & Nakamura, M. 2022, Modeling Nearby Low-Luminosity Active-Galactic-Nucleus Jet Images at All VLBI Scales, *Galaxies*, 10, 104, doi: [10.3390/galaxies10060104](https://doi.org/10.3390/galaxies10060104)
- Rani, B., Krichbaum, T. P., Lee, S. S., et al. 2017, Probing the gamma-ray variability in 3C 279 using broad-band observations, *Monthly Notices of the Royal Astronomical Society*, 464, 418, doi: [10.1093/mnras/stw2342](https://doi.org/10.1093/mnras/stw2342)
- Rani, B., Mundo, S. A., Mushotzky, R., et al. 2022, Hard X-Ray Emission in Centaurus A, *The Astrophysical Journal*, 932, 104, doi: [10.3847/1538-4357/ac6fd4](https://doi.org/10.3847/1538-4357/ac6fd4)
- Rani, B., Krichbaum, T. P., Fuhrmann, L., et al. 2013, Radio to gamma-ray variability study of blazar S5 0716+714, *Astronomy & Astrophysics*, 552, A11, doi: [10.1051/0004-6361/201321058](https://doi.org/10.1051/0004-6361/201321058)
- Reber, G. 1944, Cosmic Static., *The Astrophysical Journal*, 100, 279, doi: [10.1086/144668](https://doi.org/10.1086/144668)
- Rees, M. J. 1971, New Interpretation of Extragalactic Radio Sources, *Nature*, 229, 312, doi: [10.1038/229312a0](https://doi.org/10.1038/229312a0)
- Reynolds, C. S., Di Matteo, T., Fabian, A. C., Hwang, U., & Canizares, C. R. 1996, The ‘quiescent’ black hole in M87, *Monthly Notices of the Royal Astronomical Society*, 283, L111, doi: [10.1093/mnras/283.4.L111](https://doi.org/10.1093/mnras/283.4.L111)
- Rieger, F. M. 2017, in *American Institute of Physics Conference Series*, Vol. 1792, 6th International Symposium on High Energy Gamma-Ray Astronomy (AIP), 020008, doi: [10.1063/1.4968893](https://doi.org/10.1063/1.4968893)
- Rodrigues, X., Heinze, J., Palladino, A., van Vliet, A., & Winter, W. 2021, Active Galactic Nuclei Jets as the Origin of Ultrahigh-Energy Cosmic Rays and Perspectives for the Detection of Astrophysical Source Neutrinos at EeV Energies, *Physical Review Letters*, 126, 191101, doi: [10.1103/PhysRevLett.126.191101](https://doi.org/10.1103/PhysRevLett.126.191101)
- Roychowdhury, A., Meyer, E. T., Georganopoulos, M., Breiding, P., & Petropoulou, M. 2022, Circumnuclear Dust in AP Librae and the Source of Its VHE Emission, *The Astrophysical Journal*, 924, 57, doi: [10.3847/1538-4357/ac34f1](https://doi.org/10.3847/1538-4357/ac34f1)
- Rybicki, G. B., & Lightman, A. P. 1986, *Radiative Processes in Astrophysics*

- Sahakyan, N. 2020, Broad-band study of high-synchrotron-peaked BL Lac object 1ES 1218+304, *Monthly Notices of the Royal Astronomical Society*, 496, 5518, doi: [10.1093/mnras/staa1893](https://doi.org/10.1093/mnras/staa1893)
- Sahu, S., López Fortín, C. E., Castañeda Hernández, L. H., & Rajpoot, S. 2021, A Two-zone Photohadronic Interpretation of the EHBL-like Behavior of the 2016 Multi-TeV Flares of 1ES 1959+650, *The Astrophysical Journal*, 906, 91, doi: [10.3847/1538-4357/abc9c6](https://doi.org/10.3847/1538-4357/abc9c6)
- Salpeter, E. E. 1964, Accretion of Interstellar Matter by Massive Objects., *The Astrophysical Journal*, 140, 796, doi: [10.1086/147973](https://doi.org/10.1086/147973)
- Scargle, J. D., Norris, J. P., Jackson, B., & Chiang, J. 2013, The Bayesian Block Algorithm, arXiv e-prints, arXiv:1304.2818. <https://arxiv.org/abs/1304.2818>
- Schimoia, J. S., Storchi-Bergmann, T., Grupe, D., et al. 2015, Short-timescale Monitoring of the X-Ray, UV, and Broad Double-peak Emission Line of the Nucleus of NGC 1097, *The Astrophysical Journal*, 800, 63, doi: [10.1088/0004-637x/800/1/63](https://doi.org/10.1088/0004-637x/800/1/63)
- Schmidt, M. 1963, 3C 273 : A Star-Like Object with Large Red-Shift, *Nature*, 197, 1040, doi: [10.1038/1971040a0](https://doi.org/10.1038/1971040a0)
- Schwartz, D. A., Marshall, H. L., Lovell, J. E. J., et al. 2000, Chandra Discovery of a 100 kiloparsec X-Ray Jet in PKS 0637-752, *The Astrophysical Journal Letters*, 540, 69, doi: [10.1086/312875](https://doi.org/10.1086/312875)
- Schwartz, D. A., Siemiginowska, A., Snios, B., et al. 2020, Two Candidate High-redshift X-Ray Jets without Coincident Radio Jets, *The Astrophysical Journal*, 904, 57, doi: [10.3847/1538-4357/abbd99](https://doi.org/10.3847/1538-4357/abbd99)
- Seyfert, C. K. 1943, Nuclear Emission in Spiral Nebulae., *The Astrophysical Journal*, 97, 28, doi: [10.1086/144488](https://doi.org/10.1086/144488)
- Shakura, N. I., & Sunyaev, R. A. 1973, Black holes in binary systems. Observational appearance., *Astronomy & Astrophysics*, 24, 337
- Shapiro, S. L., Lightman, A. P., & Eardley, D. M. 1976, A two-temperature accretion disk model for Cygnus X-1: structure and spectrum., *The Astrophysical Journal*, 204, 187, doi: [10.1086/154162](https://doi.org/10.1086/154162)
- Shklovskii, I. S. 1955, O Prirode Izlučeniâ Radiogalaktiki NGC 4486 On the Nature of the Emission of Radiogalaxy NGC 4486., *Astronomicheskii Zhurnal*, 32, 215
- Sikora, M., Stawarz, Ł., & Lasota, J.-P. 2007, Radio Loudness of Active Galactic Nuclei: Observational Facts and Theoretical Implications, *The Astrophysical Journal*, 658, 815, doi: [10.1086/511972](https://doi.org/10.1086/511972)

- Singh, K., Meintjes, P., Ramamonjisoa, F., & Tolamatti, A. 2019, Extremely High energy peaked BL Lac nature of the TeV blazar Mrk 501, *Nature Astronomy*, 73, 101278, doi: [10.1016/j.newast.2019.101278](https://doi.org/10.1016/j.newast.2019.101278)
- Sinha, A., Shukla, A., Misra, R., et al. 2015, Underlying particle spectrum of Mkn 421 during the huge X-ray flare in April 2013, *Astronomy & Astrophysics*, 580, A100, doi: [10.1051/0004-6361/201526264](https://doi.org/10.1051/0004-6361/201526264)
- Snios, B., Nulsen, P. E. J., Kraft, R. P., et al. 2019, Detection of Superluminal Motion in the X-Ray Jet of M87, *The Astrophysical Journal*, 879, 8, doi: [10.3847/1538-4357/ab2119](https://doi.org/10.3847/1538-4357/ab2119)
- Stawarz, Ł., Kneiske, T. M., & Kataoka, J. 2006, Kiloparsec-Scale Jets in FR I Radio Galaxies and the γ -Ray Background, *The Astrophysical Journal*, 637, 693, doi: [10.1086/498084](https://doi.org/10.1086/498084)
- Stawarz, Ł., Sikora, M., & Ostrowski, M. 2003, High-Energy Gamma Rays from FR I Jets, *The Astrophysical Journal*, 597, 186, doi: [10.1086/378290](https://doi.org/10.1086/378290)
- Strüder, L., Briel, U., Dennerl, K., et al. 2001, The European Photon Imaging Camera on XMM-Newton: The pn-CCD camera, *Astronomy & Astrophysics*, 365, L18, doi: [10.1051/0004-6361:20000066](https://doi.org/10.1051/0004-6361:20000066)
- Su, M., Slatyer, T. R., & Finkbeiner, D. P. 2010, Giant Gamma-ray Bubbles from Fermi-LAT: Active Galactic Nucleus Activity or Bipolar Galactic Wind?, *The Astrophysical Journal*, 724, 1044, doi: [10.1088/0004-637x/724/2/1044](https://doi.org/10.1088/0004-637x/724/2/1044)
- Sun, X.-N., Yang, R.-Z., Rieger, F. M., Liu, R.-Y., & Aharonian, F. 2018, Energy distribution of relativistic electrons in the kiloparsec scale jet of M 87 with Chandra, *Astronomy & Astrophysics*, 612, A106, doi: [10.1051/0004-6361/201731716](https://doi.org/10.1051/0004-6361/201731716)
- Tagliaferri, G., Foschini, L., Ghisellini, G., et al. 2008, Simultaneous Multiwavelength Observations of the Blazar 1ES 1959+650 at a Low TeV Flux, *The Astrophysical Journal*, 679, 1029, doi: [10.1086/586731](https://doi.org/10.1086/586731)
- Tanada, K., Kataoka, J., Arimoto, M., et al. 2018a, The Origins of the Gamma-Ray Flux Variations of NGC 1275 Based on Eight Years of Fermi-LAT Observations, *The Astrophysical Journal*, 860, 74, doi: [10.3847/1538-4357/aac26b](https://doi.org/10.3847/1538-4357/aac26b)
- Tanada, K., Kataoka, J., Arimoto, M., et al. 2018b, The Origins of the Gamma-Ray Flux Variations of NGC 1275 Based on Eight Years of Fermi-LAT Observations, *The Astrophysical Journal*, 860, 74, doi: [10.3847/1538-4357/aac26b](https://doi.org/10.3847/1538-4357/aac26b)
- Tanada, K., Kataoka, J., & Inoue, Y. 2019, Inverse Compton Scattering of Starlight in the Kiloparsec-scale Jet in Centaurus A: The Origin of Excess TeV γ -Ray Emission, *The Astrophysical Journal*, 878, 139, doi: [10.3847/1538-4357/ab2233](https://doi.org/10.3847/1538-4357/ab2233)

Tavecchio, F., Maraschi, L., Sambruna, R. M., & Urry, C. M. 2000, The X-Ray Jet of PKS 0637-752: Inverse Compton Radiation from the Cosmic Microwave Background?, *The Astrophysical Journal Letters*, 544, L23, doi: [10.1086/317292](https://doi.org/10.1086/317292)

Tavecchio, F., Righi, C., Capetti, A., Grandi, P., & Ghisellini, G. 2018, High-energy neutrinos from FR0 radio galaxies?, *Monthly Notices of the Royal Astronomical Society*, 475, 5529, doi: [10.1093/mnras/sty251](https://doi.org/10.1093/mnras/sty251)

Tchekhovskoy, A., Narayan, R., & McKinney, J. C. 2011, Efficient generation of jets from magnetically arrested accretion on a rapidly spinning black hole, *Monthly Notices of the Royal Astronomical Society*, 418, L79, doi: [10.1111/j.1745-3933.2011.01147.x](https://doi.org/10.1111/j.1745-3933.2011.01147.x)

The Event Horizon Collaboration. 2021, First M87 Event Horizon Telescope Results. VIII. Magnetic Field Structure near The Event Horizon, arXiv e-prints, arXiv:2105.01173. <https://arxiv.org/abs/2105.01173>

The Event Horizon Telescope Collaboration. 2023, First Sagittarius A* Event Horizon Telescope Results. I. The Shadow of the Supermassive Black Hole in the Center of the Milky Way, arXiv e-prints, arXiv:2311.08680, doi: [10.48550/arXiv.2311.08680](https://doi.org/10.48550/arXiv.2311.08680)

The Event Horizon Telescope-Multi-wavelength science working group, The Event Horizon Telescope Collaboration, The Fermi Large Area Telescope Collaboration, et al. 2024, Broadband Multi-wavelength Properties of M87 during the 2018 EHT Campaign including a Very High Energy Flaring Episode, arXiv e-prints, arXiv:2404.17623, doi: [10.48550/arXiv.2404.17623](https://doi.org/10.48550/arXiv.2404.17623)

Thompson, D. J. 2015, Space detectors for gamma rays (100 MeV-100 GeV): From EGRET to Fermi LAT, *Comptes Rendus Physique*, 16, 600, doi: [10.1016/j.crhy.2015.07.002](https://doi.org/10.1016/j.crhy.2015.07.002)

Thompson, D. J., & Wilson-Hodge, C. A. 2022, in *Handbook of X-ray and Gamma-ray Astrophysics*, 29, doi: [10.1007/978-981-16-4544-0_58-1](https://doi.org/10.1007/978-981-16-4544-0_58-1)

Tomar, G., & Gupta, N. 2023, X-Ray Flares in the Long-term Light Curve of Low-luminosity Active Galactic Nucleus M81*, *The Astrophysical Journal*, 950, 113, doi: [10.3847/1538-4357/acd16d](https://doi.org/10.3847/1538-4357/acd16d)

Tomar, G., Gupta, N., & Prince, R. 2021, Broadband Modeling of Low-luminosity Active Galactic Nuclei Detected in Gamma Rays, *The Astrophysical Journal*, 919, 137, doi: [10.3847/1538-4357/ac1588](https://doi.org/10.3847/1538-4357/ac1588)

Trager, S. C., Faber, S. M., Worthey, G., & González, J. J. 2000, The Stellar Population Histories of Local Early-Type Galaxies. I. Population Parameters, *The Astronomical Journal*, 119, 1645, doi: [10.1086/301299](https://doi.org/10.1086/301299)

- Turner, M. J. L., Abbey, A., Arnaud, M., et al. 2001, The European Photon Imaging Camera on XMM-Newton: The MOS cameras, *Astronomy & Astrophysics*, 365, L27, doi: [10.1051/0004-6361:20000087](https://doi.org/10.1051/0004-6361:20000087)
- Urry, C. M., & Padovani, P. 1995, Unified Schemes for Radio-Loud Active Galactic Nuclei, *Publications of the Astronomical Society of the Pacific*, 107, 803, doi: [10.1086/133630](https://doi.org/10.1086/133630)
- Venturi, T., Giovannini, G., Feretti, L., Comoretto, G., & Wehrle, A. E. 1993, VLBI Observations of a Complete Sample of Radio Galaxies. II. The Parsec-Scale Structure of NGC 315, *The Astrophysical Journal*, 408, 81, doi: [10.1086/172571](https://doi.org/10.1086/172571)
- Verdoes Kleijn, G. A., Baum, S. A., de Zeeuw, P. T., & O’Dea, C. P. 1999, Hubble Space Telescope Observations of Nearby Radio-Loud Early-Type Galaxies, *The Astronomical Journal*, 118, 2592, doi: [10.1086/301135](https://doi.org/10.1086/301135)
- Verdoes Kleijn, G. A., Baum, S. A., de Zeeuw, P. T., & O’Dea, C. P. 2002, Core Radio and Optical Emission in the Nuclei of nearby FR I Radio Galaxies, *The Astronomical Journal*, 123, 1334, doi: [10.1086/339177](https://doi.org/10.1086/339177)
- Vermeulen, R. C., Readhead, A. C. S., & Backer, D. C. 1994, Discovery of a Nuclear Counterjet in NGC 1275: A New Way to Probe the Parsec-Scale Environment, *The Astrophysical Journal Letters*, 430, L41, doi: [10.1086/187433](https://doi.org/10.1086/187433)
- Volonteri, M. 2010, Formation of supermassive black holes, *The Astronomy and Astrophysics Review*, 18, 279, doi: [10.1007/s00159-010-0029-x](https://doi.org/10.1007/s00159-010-0029-x)
- Walker, R. C., Dhawan, V., Romney, J. D., Kellermann, K. I., & Vermeulen, R. C. 2000, VLBA Absorption Imaging of Ionized Gas Associated with the Accretion Disk in NGC 1275, *The Astrophysical Journal*, 530, 233, doi: [10.1086/308372](https://doi.org/10.1086/308372)
- Walker, R. C., Hardee, P. E., Davies, F. B., Ly, C., & Junor, W. 2018, The Structure and Dynamics of the Subparsec Jet in M87 Based on 50 VLBA Observations over 17 Years at 43 GHz, *The Astrophysical Journal*, 855, 128, doi: [10.3847/1538-4357/aaafcc](https://doi.org/10.3847/1538-4357/aaafcc)
- Walker, R. C., Romney, J. D., & Benson, J. M. 1994, Detection of a VLBI Counterjet in NGC 1275: A Possible Probe of the Parsec-Scale Accretion Region, *The Astrophysical Journal Letters*, 430, L45, doi: [10.1086/187434](https://doi.org/10.1086/187434)
- Wang, F., Yang, J., Fan, X., et al. 2021, A Luminous Quasar at Redshift 7.642, *The Astrophysical Journal Letters*, 907, L1, doi: [10.3847/2041-8213/abd8c6](https://doi.org/10.3847/2041-8213/abd8c6)
- Whysong, D., & Antonucci, R. 2004, Thermal Emission as a Test for Hidden Nuclei in Nearby Radio Galaxies, *The Astrophysical Journal*, 602, 116, doi: [10.1086/380828](https://doi.org/10.1086/380828)

- Wilks, S. S. 1938, The Large-Sample Distribution of the Likelihood Ratio for Testing Composite Hypotheses, *Annals Math. Statist.*, 9, 60, doi: [10.1214/aoms/1177732360](https://doi.org/10.1214/aoms/1177732360)
- Wilms, J., Allen, A., & McCray, R. 2000, On the Absorption of X-Rays in the Interstellar Medium, *The Astrophysical Journal*, 542, 914, doi: [10.1086/317016](https://doi.org/10.1086/317016)
- Woltjer, L. 1959, Emission Nuclei in Galaxies., *The Astrophysical Journal*, 130, 38, doi: [10.1086/146694](https://doi.org/10.1086/146694)
- Wood, M., Caputo, R., Charles, E., et al. 2017, in International Cosmic Ray Conference, Vol. 301, 35th International Cosmic Ray Conference (ICRC2017), 824. <https://arxiv.org/abs/1707.09551>
- Worrall, D. M. 2009, The X-ray jets of active galaxies, *The Astronomy and Astrophysics Review*, 17, 1, doi: [10.1007/s00159-008-0016-7](https://doi.org/10.1007/s00159-008-0016-7)
- Worrall, D. M., Birkinshaw, M., & Hardcastle, M. J. 2003, The X-ray jet and central structure of the active galaxy NGC 315, *Monthly Notices of the Royal Astronomical Society*, 343, L73, doi: [10.1046/j.1365-8711.2003.06945.x](https://doi.org/10.1046/j.1365-8711.2003.06945.x)
- Worrall, D. M., Birkinshaw, M., Laing, R. A., Cotton, W. D., & Bridle, A. H. 2007a, The inner jet of radio galaxy NGC 315 as observed with Chandra and the Very Large Array, *Monthly Notices of the Royal Astronomical Society*, 380, 2, doi: [10.1111/j.1365-2966.2007.11998.x](https://doi.org/10.1111/j.1365-2966.2007.11998.x)
- Worrall, D. M., Birkinshaw, M., Laing, R. A., Cotton, W. D., & Bridle, A. H. 2007b, The inner jet of radio galaxy NGC 315 as observed with Chandra and the Very Large Array, *Monthly Notices of the Royal Astronomical Society*, 380, 2, doi: [10.1111/j.1365-2966.2007.11998.x](https://doi.org/10.1111/j.1365-2966.2007.11998.x)
- Worrall, D. M., Birkinshaw, M., O'Sullivan, E., et al. 2010, The jet and counterjet of 3C270 (NGC4261) viewed in the X-ray with Chandra, *Monthly Notices of the Royal Astronomical Society*, 408, 701, doi: [10.1111/j.1365-2966.2010.17162.x](https://doi.org/10.1111/j.1365-2966.2010.17162.x)
- Xue, Y., Yuan, F., & Cui, W. 2006, X-Ray Spectral Variability of TeV Blazars during Rapid Flares, *The Astrophysical Journal*, 647, 194, doi: [10.1086/505381](https://doi.org/10.1086/505381)
- Younes, G., Porquet, D., Sabra, B., Reeves, J. N., & Grosso, N. 2012, Study of LINER sources with broad H α emission. Spectral energy distribution and multiwavelength correlations, *Astronomy & Astrophysics*, 539, A104, doi: [10.1051/0004-6361/201118299](https://doi.org/10.1051/0004-6361/201118299)
- Young, J. S., Xie, S., Tacconi, L., et al. 1995, The FCRAO Extragalactic CO Survey. I. The Data, *The Astrophysical Journal Supplement Series*, 98, 219, doi: [10.1086/192159](https://doi.org/10.1086/192159)

Zacharias, M., & Wagner, S. 2016, AP Librae: The Extended Jet as the Source of VHE Emission?, *Galaxies*, 4, 63, doi: [10.3390/galaxies4040063](https://doi.org/10.3390/galaxies4040063)

Zel'dovich, Y. B., & Novikov, I. D. 1964, The Radiation of Gravity Waves by Bodies Moving in the Field of a Collapsing Star, *Soviet Physics Doklady*, 9, 246

Zezas, A., Birkinshaw, M., Worrall, D. M., Peters, A., & Fabbiano, G. 2005, Chandra Observations of NGC 4261 (3C 270): Revealing the Jet and Hidden Active Galactic Nucleus in a Type 2 LINER, *The Astrophysical Journal*, 627, 711, doi: [10.1086/430044](https://doi.org/10.1086/430044)

Zhang, H., & Böttcher, M. 2013, X-Ray and Gamma-Ray Polarization in Leptonic and Hadronic Jet Models of Blazars, *The Astrophysical Journal*, 774, 18, doi: [10.1088/0004-637x/774/1/18](https://doi.org/10.1088/0004-637x/774/1/18)